A study of $B^0 \longrightarrow \pi^+\pi^-$ decays using the BABAR detector

E. Tetteh-Lartey

Royal Holloway, University of London

This thesis is submitted in part fulfilment
of the requirement for the degree of PhD
from the University of London.

November 24 1997

Abstract

This thesis reports on the sensitivity of the BABAR detector to the study of CP violation in the B system. Due to the presence of π^0's in most channels of interest to CP violation studies, an electromagnetic calorimeter with high efficiency and good energy resolution for low energy photons is needed for good π^0 and thus B mass resolution. A beam test of a prototype CsI electromagnetic calorimeter and its response to low energy electrons and pions is presented. Measurement of the CKM angle α requires the study of the decay $B \longrightarrow \pi^+\pi^-$, but this is complicated by the presence of penguin diagrams. A clean measurement of α and isolation of these penguin diagrams requires the use of isospin symmetry through the study of B decays to $\pi^+\pi^-$, $\pi^+\pi^0$ and $\pi^0\pi^0$. The branching ratio of $B \longrightarrow \pi^0\pi^0$ is expected to be $\sim 10^{-7}$ implying large statistical errors. In addition a heavy contamination from continuum background is expected which will introduce further systematic errors. These errors will feed into the errors on the penguin correction. A maximum likelihood fitting procedure has been developed to fit the data in preference to event counting to minimise these errors.

Contents

Acknowledgements

I would like to express my sincere gratitude to the following people who have been of immense help to me.

Firstly I would like to thank my supervisor Mike Green for the good supervisory role he played and also reading through this thesis. My special thanks also goes to Damian Johnson and Iain Scott who have help me with the understanding of the programming tools and the theory behind my work. My thanks also goes to Terry Medcalf and Derek Brown for their guidance and advice in the course of my work.

I would also like to thank all the staff and students of the Royal Holloway and Bedford New College HEP group for their ever friendly and helpful attitude.

Preface

The BABAR experiment involves a collaboration of physicists and engineers from research institutions and universities all over the world, with a common aim of building a detector for CP violation studies in the B system. During the three years of my studies for the PhD, I have been closely involved with members of the collaboration in building the detector. In September 1995, I was involved in the testing of a prototype electromagnetic calorimeter at PSI (Zurich). In particular my work was focused on the analysis of the data for pions and electron interactions, the results of which were included in a BABAR note. In addition I have presented work on a simulated response of the detector to CP violation studies at BABAR workshops and conferences. The results of my work as presented in this thesis gives the collaboration an insight of what the real detector will be capable of measuring and to what degree of accuracy. It also provides strategies that could be adopted for better precision measurements.

Chapter 1

The Standard Model and CP violation

1.1 Introduction

Towards the end of the nineteenth century it had become possible to give a satisfactory account of almost all physical phenomena by applying the laws of classical physics. However an overwhelming amount of experimental evidence around the turn of the century showed some limitations on the classical theory. The development of quantum mechanics and relativity in the twentieth century explained many of these difficulties and demonstrated that classical theory could be obtained as an approximation of these new theories. The development of quantum field theory was necessitated by the desire to develop a consistent theoretical framework for describing quantum mechanics of relativistic particles, i.e. particles with velocities approaching the speed of light. Modern particle physics was built solidly on these two theories.

The Standard Model (based on locally gauge-invariant quantum field theory) appears to give a successful description of all the phenomenology of particle physics. The gauge particles are the quanta of the fields. The model provides a list of the physical fields and describes the non-linear interactions that occur between these fields. There are three forces – the strong, the electromagnetic and the weak. There are three symmetries of strong interactions that are not conserved in weak processes. These are the symmetries C (charge conjugation which relates particle to antiparticle), P (parity which relates a

left-handed particle to a similar right-handed one) and T (time-reversal invariance which relates a process or state to the time-reversed process or state). In the Standard Model all weak decays violate C and P but conserve CP with the exception of a very small part that violates CP. This is explained by the CKM (Cabibbo-Kobayashi-Maskawa) matrix which describes the mixing of the quarks. This violation occurs because there is a single phase that remains in the CKM matrix after all possible redefinitions that can remove such phases have been made. An important prediction of the model's explanation of CP violation is the existence of large, calculable asymmetries in the decays of B mesons to CP eigenstates. Excess of matter over antimatter in our universe is one of the key puzzles in cosmology. The Standard Model provides an explanation to this by CP violation. This is however an inadequate explanation since the size of the effect is too small to fully account for the photon to baryonic ratio in our universe. Up to this present time, CP violation has only been observed in the Kaon system. Experiments such as BABAR are currently being designed and built in order to measure CP violation in the B system. BABAR will begin operation in 1999. In this thesis, a study of CP violation in B decays to $\pi\pi$ with the BABAR detector is presented.

1.2 The Standard Model

The term Standard Model was originally used to mean the Glashow–Weinberg–Salam model of electroweak interactions. There are three classes of fields in the model—spin 0 (scalar), spin 1 (vector) and spin 1/2 fermionic fields. The fermionic fields make up all matter in the universe. The quarks and leptons are the quanta of these fields. The four known forces between particles are the strong, the weak, the electromagnetic and the gravitational forces. Only the first three of these forces have been incorporated successfully into the Standard Model. In the model, it is required that all fermionic fields be invariant under local SU(3) $\otimes$ SU(2) $\otimes$ U(1) transformations. The theory is a gauge theory with two principal sectors: QCD (the strong interaction sector) and the electroweak sector. The force between two matter fields arises from the exchange of a quantum of a vector or gauge field and thus it has an associated gauge group. For a matter field to experience a force, it must couple to the associated gauge field and have a non-

zero value of the gauge charge. U(1) is the gauge group for electromagnetic interactions which has a local phase or gauge invariance. The gauge boson required by invariance of the theory under U(1) transformation is labelled B^{μ}. The gauge boson that mediates this force is the photon. The group charge is the electric charge. The gauge group for weak interactions is the SU(2) group. The associated gauge bosons necessary to maintain the invariance of the theory are called W_i^{μ}, i = 1, 2, 3, with μ indicating a spin one boson. There is one boson for each of the three generators of the SU(2) transformation. Their electromagnetic charge states are related by:

$$W^{+} = (-W^{1} + iW^{2})/\sqrt{2}$$

$$W^{-} = (-W^{1} - iW^{2})/\sqrt{2}$$

$$W^{0} = W^{3}.$$

SU(3) is the gauge group for strong interactions. The associated gauge bosons that mediate the force are labelled G_a^{μ}, where a = 1, 2,...8, since there is one spin-one boson for each of the eight generators of SU(3). These bosons are called gluons. The charge of the gauge group is called colour, and can take one of the three values red, green or blue. The theory that describes the interactions of these gauge bosons is called quantum chromodynamics (QCD).

The fermionic fields are divided into two classes: quarks and leptons. There are six quarks and six leptons. These classes are further divided into 3 generations of particles each of which contains a weak isospin doublet of quarks and leptons (see table 1.1). These are all left-handed fermions. The right-handed states exist as singlets with the exception of the neutrino whose right-handed state has not been observed. The same structure exists for the anti-fermions and there is no left-handed anti-neutrino.

In the Standard Model all fermions and bosons are massless, holding the lagrangian invariant under $SU(3)_C \otimes SU(2)_L \otimes U(1)_Y$ transformations. The scalar fields are a by-product of the mechanism by which particles acquire mass, with the lagrangian still maintaining its gauge invariance, a process called spontaneous symmetry breaking. The quantum of the scalar field is the spin zero Higgs particle.

	QUARKS		LEPTONS	
Generation	Flavour	Electric charge	Flavour	Electric charge
1	u	+2/3	ν_e	0
	d	-1/3	e	−1
2	c	+2/3	ν_μ	0
	s	-1/3	μ	−1
3	t	+2/3	ν_τ	0
	b	-1/3	τ	−1

Table 1.1: The physical properties of fermionic matter.

1.2.1 Electroweak unification

Unification of electromagnetic and weak interaction into one single theory invariant under the combined transformation of $SU(2)_L \otimes U(1)_Y$ was achieved in the 1960s by Weinberg and Salam after being first proposed by Glashow. It predicted the existence of a weak neutral current and massive vector bosons ($W^{\pm}$, Z^0). The weak neutral currents were discovered in 1973 by GARGAMELLE at CERN [1] and the massive vector bosons were later discovered in 1983 by the UA1 and UA2 collaborations at CERN [1]. The fermions are arranged into three left-handed doublets

$$\begin{pmatrix} u \\ d \end{pmatrix}, \begin{pmatrix} c \\ s \end{pmatrix}, \begin{pmatrix} t \\ b \end{pmatrix}; \quad \begin{pmatrix} \nu_e \\ e^- \end{pmatrix}, \begin{pmatrix} \nu_\mu \\ \mu^- \end{pmatrix}, \begin{pmatrix} \nu_\tau \\ \tau^- \end{pmatrix}$$

and right-handed singlets: u, c, t, d, s, b, e^-, μ^- and τ^-. The Standard Model lagrangian for fermionic fields is

$$L_f = \sum_f \overline{f} i\gamma^\mu D_\mu f, \tag{1.1}$$

where f is the fermionic field and

$$D_\mu = \partial_\mu - ig_1 \frac{Y}{2} B_\mu - ig_2 \frac{\tau^i}{2} W_\mu^i - ig_3 \frac{\lambda^a}{2} G_\mu^a. \tag{1.2}$$

Y is the generator of U(1) transformations, τ^i (where i=1,2,3) are the Pauli spin matrices, the generators of SU(2) transformations, λ^a (where a=1,...,8) are 3×3 matrices, the

generators of SU(3) transformations, g_1, g_2, g_3 are the coupling constants for the U(1), SU(2), SU(3) groups respectively.

The effective (interaction) lagrangian for U(1) interactions for the first generation of leptons in SU(2) space is

$$L_f(U(1)) = \frac{g_1}{2}[Y_L(\overline{\nu}_L\gamma^\mu\nu_L + \overline{e}_L\gamma^\mu e_L) + Y_R\overline{e}_R\gamma^\mu e_R]B_\mu. \tag{1.3}$$

For SU(2) interactions the effective lagrangian for the first leptonic generation in SU(2) space is given by

$$L_f(SU(2)) = \frac{g_2}{2}[\overline{\nu}_L\gamma^\mu\nu_L W_\mu^0 - \sqrt{2}\overline{\nu}_L\gamma^\mu e_L W_\mu^+ - \sqrt{2}\overline{e}_L\gamma^\mu\nu_L W_\mu^- - \overline{e}_L\gamma^\mu e_L W_\mu^0]. \tag{1.4}$$

The first term of eqn. 1.3 predicts that the neutrino interacts electromagnetically which is a contradiction to experiment. A way of solving this problem is by combining equations eqn. 1.3 and 1.4 into one single equation, i.e. U(1) $\otimes$ SU(2) which we call electroweak unification. This is achieved by introducing two fields, A_μ and Z_μ, and assuming that the electromagnetic field A_μ, is a combination of B_μ and W_μ^0 defined as follows:

$$B_\mu = \frac{g_2A_\mu + g_1Y_LZ_\mu}{\sqrt{g_2^2 + g_1^2Y_L^2}},\ W_\mu^0 = \frac{-g_1Y_LA_\mu + g_2Z_\mu}{\sqrt{g_2^2 + g_1^2Y_L^2}}$$

$$W_\mu^0 = \cos\theta_W Z_\mu + \sin\theta_W A_\mu,\ B_\mu = -\sin\theta_W Z_\mu + \cos\theta_W A_\mu,$$

where

$$\sin\theta_W = \frac{g_1}{\sqrt{g_2^2 + g_1^2}},\ \cos\theta_W = \frac{g_2}{\sqrt{g_2^2 + g_1^2}}.$$

The effective lagrangian for $SU(2)_L \otimes$ U $(1)_Y$ can be split into two parts, L_{NC}, a neutral current contribution where the incoming and outgoing fermions have the same electric charge, and a charge current contribution, L_{CC}, where the incoming and outgoing fermions have a charge difference of one unit. For all three generations of fermions the neutral current lagrangian of SU(2) $\otimes$U(1) has the general form

$$L_{NC} = \left[\sum_i \overline{\chi}_L^i\gamma^\mu(-g_2\sin\theta_W\tfrac{\tau_3}{2})\chi_L^i - \sum_j \overline{\phi}_R^j\gamma^\mu g_1\cos\theta_W\tfrac{Y}{2}\phi_R^j\right]A_\mu$$

$$+\left[\sum_i \overline{\chi}_L^i\gamma^\mu(-g_2\cos\theta_W\tfrac{\tau_3}{2} + g_1\sin\theta_W\tfrac{Y}{2})\chi_L^i + \sum_j \overline{\phi}_R^j\gamma^\mu g_1\sin\theta_W\tfrac{Y}{2}\phi_R^j\right]Z_\mu \tag{1.5}$$

and the charge current has the form

$$L_{CC} = -\frac{g_2}{2\sqrt{2}}\sum_i \overline{\chi}_L^i\gamma^\mu\tau_+\chi_L^iW_\mu^+ + \overline{\chi}_L^i\gamma^\mu\tau_-\chi_L^iW_\mu^- \tag{1.6}$$

Fermion	I	I_3	Y	Q
u_L, c_L, t_L	1/2	1/2	1/3	+2/3
u_R, c_R, t_R	0	0	4/3	+2/3
d_L, s_L, b_L	1/2	-1/2	1/3	-1/3
d_R, s_R, b_R	0	0	-2/3	-1/3
e_L, μ_L, τ_L	1/2	-1/2	-1	-1
e_R, μ_R, τ_R	0	0	-2	-1
$\nu_{eL}, \nu_{\mu L}, \nu_{\tau L}$	1/2	1/2	-1	0

Table 1.2: Charge and Isospin values for SU(2) $\otimes$ U(1)$_Y$ fermionic fields.

$$\tau_{\pm} = \tau_1 \pm i\tau_2,$$

where the electric charge is given by e $= g_2 \sin\theta_W = g_1 \cos\theta_W$. Y is the weak hypercharge and is given by $Y = 2(Q - I_3)$, where I_3 is the the third component of weak isospin and Q is the electric charge. The doublets have total weak isospin I= 1/2. Table 1.2 shows the values for I, I_3, Q and Y for the fermionic fields.

Equation 1.1 shows no mass terms in the lagrangian. Experimental observation of massive W and Z bosons implies there must be mass terms in the lagrangian. However introducing mass terms directly into the lagrangian will break SU(2) $\otimes$ U(1) gauge invariant symmetry which is necessary for the theory to be renormalisable, and therefore predictive. Mass terms are introduced by the coupling of a scalar field called the Higgs to the particle fields while still maintaining the symmetry. The process is called the Higgs mechanism. Searches for the Higgs boson are one motivation for multi-TeV hadron colliders such as LHC (expected to begin operation in 2005). Searches for the Higgs boson in e^+e^- collisions at LEP have set a lower limit of 69.4 GeV/c^2 on the mass (M_H) [2].

1.3 CP violation in the Standard Model

Although parity violation was discovered in 1956 it was thought at that time that the combined operator CP would be conserved in all weak processes. This was later discovered not to be true when CP violation was first observed in the Kaon system (see section 1.3.7). Other evidence of CP violation is the existence of non-zero baryon number in the universe.

CP violation is also expected to show up in the B system. In the Standard Model, the only source of CP violation is the CKM matrix, (discussed further in section 1.3.1).

For the past two decades experiments have been designed to investigate CP violation and provide a stringent test of the Standard Model explanation. Experiments at Fermilab and CERN have measured CP violation parameters in the neutral Kaon system. Searches at LEP for CP violation in the B system [3] have been made, however the sensitivity is not enough for expected effects as predicted by the Standard Model. In the next few years experiments such as CLEO III at CESR, BELLE at KEK, BABAR at SLAC, LHC-B at CERN, CDF, $D0$ and BTEV at Fermilab and HERA-B at DESY will join in these searches. BTEV and LHC-B will operate with pp collider machines at centre of mass energies >1 TeV. The BTEV experiment has a long term goal of carrying out precision studies of CP violation, mixing and rare decays of b and c quarks in the forward direction at the Fermilab Tevatron collider which produces 10^{11} b hadrons and 10^{12} c hadrons in $10^7 s$ at a luminosity of 10^{32} cm$^2 s^{-1}$. The LHC-B experiment will have five times this cross section for $b\overline{b}$ production at the same luminosity. CLEO, BELLE and BABAR use e^+e^- collider machines at a much lower centre of mass energy. HERA-B will study CP violation in the B system using an internal target at the HERA proton ring. At a centre of mass energy of 40 GeV, HERA will produce up to 10^9 B hadrons per year, sufficient for a CP discovery experiment and for the study of many other topics in B-physics. CDF is a general purpose experiment for the study of pp collisions at centre of mass energy of 1.8 TeV. It is optimised towards the physics of large mass scales, but has been upgraded with a silicon vertex detector for B physics. The $D0$ experiment aims to undertake CP violation studies with the Fermilab Tevatron collider. Although the $D0$ detector has been optimised for high p_T physics, its extensive muon detection system combined with triggering capabilities on relatively low-energy muons makes it feasible to study b-physics as well. Despite the huge cross section for $b\overline{b}$ pair production at pp colliders, the total inelastic cross section is enormous. The ratio $\sigma_{bb}/\sigma_{tot} \sim 1/200$ at LHC-B [4] compared to 1.2/3.5 for BABAR at centre of mass energy of 10.58 GeV. Extracting bottom physics with this large background will be a tremendous challenge. However because of the very much higher cross section a better precision is expected to be achieved at the hadron colliders.

Full exploration of B physics will require a combination of both hadron machines and e^+e^- B factories, with hadron machines providing the ultimate measurements of CP asymmetries and rare decays, whereas e^+e^- storage rings are likely to prove superior in the study of general B decay dynamics, because of the larger numbers of accessible channels and possibly smaller backgrounds. Section 4.8 discusses the current experimental limits of these experiments and the CP reach estimates.

1.3.1 CKM matrix

The CKM (Cabibbo-Kobayashi-Maskawa) matrix describes the mixing of the d, s and b quarks. In weak interactions the weak eigenstates of the quarks are not the same as the mass eigenstates since mixing occurs between the d, s and b quarks. The relation between the mass eigenstates and weak eigenstates is given by

$$\begin{pmatrix} d' \\ s' \\ b' \end{pmatrix} = V \begin{pmatrix} d \\ s \\ b \end{pmatrix}, \tag{1.7}$$

where

$$V = \begin{pmatrix} V_{ud} & V_{us} & V_{ub} \\ V_{cd} & V_{cs} & V_{cb} \\ V_{td} & V_{ts} & V_{tb} \end{pmatrix}.$$

Unitarity of the matrix V requires it has three real parameters and one unknown phase. From which we have

$$V_{td}V_{tb}^* + V_{cd}V_{cb}^* + V_{ud}V_{ub}^* = 0. \tag{1.8}$$

This relation can be represented as a triangle in the complex plane (fig. 1.1(a)), where

$$\alpha = \arg\left(-\frac{V_{td}V_{tb}^*}{V_{ud}V_{ub}^*}\right),\ \beta = \arg\left(-\frac{V_{cd}V_{cb}^*}{V_{td}V_{tb}^*}\right),\ \gamma = \arg\left(-\frac{V_{ud}V_{ub}^*}{V_{cd}V_{cb}^*}\right). \tag{1.9}$$

There exist many parametrisations of the CKM matrix. One example is that of Wolfenstein [5]

$$V_{CKM} = \begin{pmatrix} 1-\frac{\lambda^2}{2} & \lambda & |V_{ub}|exp(-i\gamma) \\ -\lambda & 1-\frac{\lambda^2}{2} & A\lambda^2 \\ |V_{td}|exp(-i\beta) & -A\lambda^2 & 1 \end{pmatrix},$$

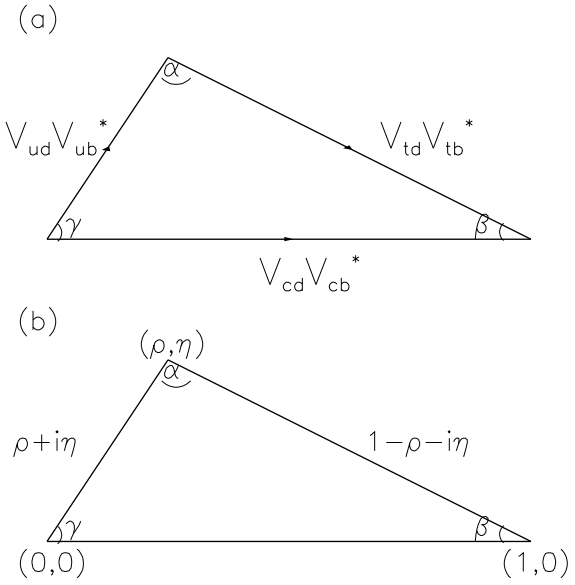

Figure 1.1: (a) The unitarity triangle, showing the CKM angles α, β and γ and the lengths of the sides of the triangle in the complex plane. (b) each of the sides of the triangle has been divided by the magnitude of $V_{cd}V_{cb}^*$.

where $\lambda = V_{us} = \sin\theta_c$ and θ_c is the Cabibbo angle. Dividing the magnitudes of all three sides of the triangle by $|V_{cd}V_{cb}^*|$, the unitarity triangle can be rescaled as shown in fig. 1.1(b) where $\rho + i\eta = V_{ub}/\lambda V_{cb}$ and $1 - \rho - i\eta = V_{td}/\lambda V_{cb}$. We then have, $|V_{td}|\exp(-i\beta) = A\lambda^3(1 - \rho - i\eta)$ and $|V_{ub}|\exp(-i\gamma) = A\lambda^3(\rho - i\eta)$. Figure 1.2 shows examples of three weak decay processes. The matrix element of the decays is given by:

$$\begin{aligned} M(n \longrightarrow pe^-\overline{\nu}_e) &= \frac{G}{\sqrt{2}}[\overline{u}_p\gamma^\mu(1-\gamma^5)u_n][\overline{u}_{\overline{\nu}_e}\gamma_\mu(1-\gamma^5)u_e] \\ M(\mu^- \longrightarrow e^-\overline{\nu}_e\overline{\nu}_\mu) &= \frac{G}{\sqrt{2}}[\overline{u}_{\nu_\mu}\gamma^\sigma(1-\gamma^5)u_\mu][\overline{u}_e\gamma_\sigma(1-\gamma^5)u_{\nu_e}] \\ M(\pi \longrightarrow \mu^+\nu_\mu) &= \frac{G}{\sqrt{2}}[\overline{u}_{\overline{d}}\gamma^a(1-\gamma^5)u_u][\overline{u}_{\mu^+}\gamma_a(1-\gamma^5)u_{\nu_\mu}], \end{aligned}$$

where G is the weak coupling constant.

In the Standard Model:

$$\Gamma(\pi^+ \longrightarrow \mu^+\nu_L) \neq \Gamma(\pi^+ \longrightarrow \mu^+\nu_R) \qquad \text{(P violation)}$$

$$\Gamma(\pi^+ \longrightarrow \mu^+\nu_L) \neq \Gamma(\pi^- \longrightarrow \mu^-\overline{\nu}_L) \qquad \text{(C violation)}$$

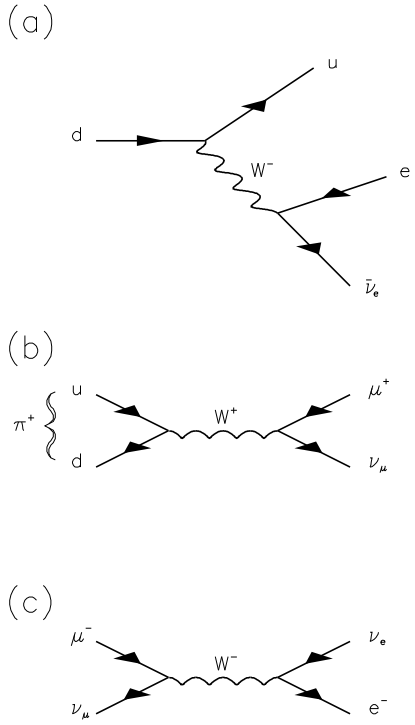

Figure 1.2: Examples of weak decay processes (a) the β decay $n \longrightarrow pe^-\overline{\nu}_e$, i.e. $d \longrightarrow ue^-\overline{\nu}_e$, (b) π decay: $\pi^+ \longrightarrow \mu^+\nu_\mu$ and (c) μ decay: $\mu^- \longrightarrow e^-\overline{\nu}_e\nu_\mu$.

but

$$\Gamma(\pi^+ \longrightarrow \mu^+\nu_L) = \Gamma(\pi^- \longrightarrow \mu^-\overline{\nu}_R) \qquad \text{(CP invariance)}.$$

A phase in the CKM matrix generates CP violation as follows. The charged current matrix element for $q_iq_j \to q_kq_l$ is

$$\begin{aligned} M &= (\overline{u}_k\gamma^\mu(1-\gamma^5)V_{ki}u_i)(\overline{u}_j\gamma_\mu(1-\gamma^5)V_{jl}u_j)^\dagger \\ &= V_{ki}V_{jl}^*(\overline{u}_k\gamma^\mu(1-\gamma^5)u_i)(\overline{u}_l\gamma_\mu(1-\gamma^5)u_j), \end{aligned}$$

where u are the appropriate Dirac spinors. If we can show that the CP transformed matrix element satisfies $M_{CP} = M^\dagger$, then the theory conserves CP. Otherwise, CP is violated.

Under C

$$\begin{aligned} u \longrightarrow u_C &= C\overline{u}^T \\ \overline{u} \longrightarrow \overline{u}_C &= -u^TC^{-1}, \end{aligned}$$

where $C^{-1}\gamma_\mu C = -\gamma_\mu^T$ and $C^{-1}\gamma_\mu\gamma^5 C = (\gamma_\mu\gamma^5)^T$.

Under P

$$P^{-1}\gamma_\mu(1+\gamma^5)P = \gamma_\mu^\dagger(1-\gamma^5),$$

where $\gamma_0^\dagger = \gamma_0, \gamma_i^\dagger = -\gamma_i$.

Then under the combined operator CP we have

$$\overline{u}_k\gamma^\mu(1-\gamma^5)V_{ki}u_i \longrightarrow -V_{ki}\overline{u}_i\gamma_\mu^\dagger(1-\gamma^5)u_k,$$

where

$$M_{CP} = V_{ki}V_{jl}^*(\overline{u}_i\gamma^\mu(1-\gamma^5)u_k)(\overline{u}_j\gamma_\mu(1-\gamma^5)u_l).$$

Now

$$M^\dagger = V_{ki}^*V_{jl}(\overline{u}_i\gamma^\mu(1-\gamma^5)u_k)(\overline{u}_j\gamma_\mu(1-\gamma^5)u_l).$$

$M_{CP} = M^\dagger$ provided V_{ij} are real. It follows that in the three generation model where V_{CKM} has a complex parameter, CP is violated. This shows up in $K^0 - \overline{K}^0$ and $B^0 - \overline{B}^0$ mixing.

There are two types of CP violation, direct CP violation which comes via interference of two decay amplitudes, and indirect CP violation (mixing-induced) due to interference between two paths to a given final state. These are discussed separately in the following sections.

1.3.2 Direct CP violation

Direct CP violation is a difference in the direct decay rate between $B \longrightarrow f$ and $\overline{B} \longrightarrow \overline{f}$ without any contribution from the mixing of B and $\overline{B}$ amplitudes. This occurs both in charged decay channels and in neutral decay channels. Consider a general decay $B^+ \longrightarrow f$ and its charge conjugate process $B^- \longrightarrow \overline{f}$. In order that these two processes have different rates, two amplitudes, A_T from the tree diagram and A_P from the penguin diagram (see fig. 1.3) must contribute with different CKM phases ($\phi_T \neq \phi_P$) and different final state interactions ($\delta_T \neq \delta_P$). The weak phases, ϕ, come from the CKM matrix, and reverse sign in going from the decay to the CP-conjugate decay. However the strong phases δ are the same for both the decay and the CP-conjugate decay since such phases are due to strong-interaction rescattering and hadronisation and since QCD is sensitive

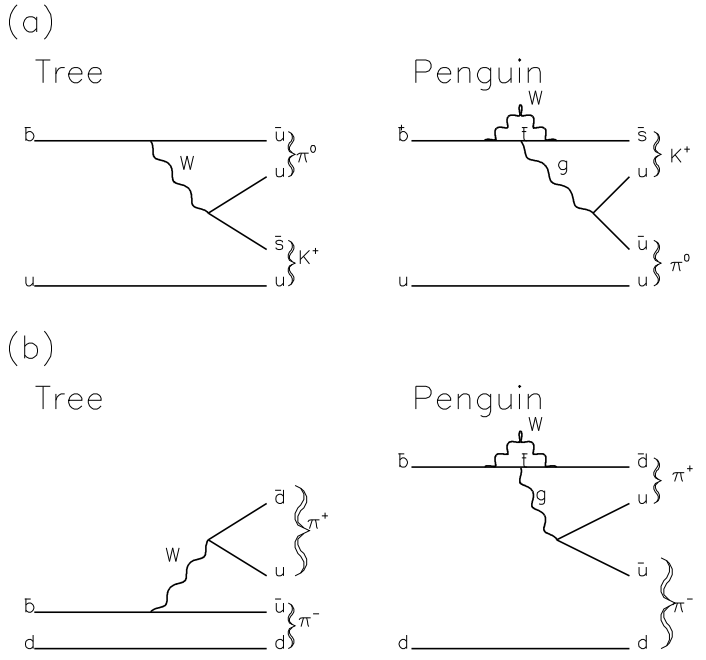

Figure 1.3: Diagrams contributing to the processes (a) $B_u^+ \longrightarrow \pi^0 K^+$ and (b) $B_d^0 \longrightarrow \pi^+\pi^-$.

to colour only, it is irrelevant whether a quark or anti-quark is involved. The amplitudes can be written as:

$$\begin{aligned} A(B^+ \longrightarrow f) &= |A_T| \exp(i\phi_T) \exp(i\delta_T) + |A_P| \exp(i\phi_P) \exp(i\delta_P) \\ \overline{A}(B^- \longrightarrow \overline{f}) &= |A_T| \exp(-i\phi_T) \exp(i\delta_T) + |A_P| \exp(-i\phi_P) \exp(i\delta_P). \end{aligned}$$

The rate asymmetry is given by [6]

$$|A|^2 - |\overline{A}|^2 = 2|A_T A_P| \sin(\phi_T - \phi_P) \sin(\delta_T - \delta_P). \tag{1.10}$$

The penguin diagrams are a loop diagram with the emission of a hard gluon (or photon) from the loop to account for the mass difference between the b quark and s or d quark produced when the W is re-absorbed. This effect suppresses the kinematic factor of the penguin relative to the tree diagram by a factor of order $\alpha(m_b)/4\pi$. This makes it difficult to make firm predictions of CP-violating effect in exclusive charged B-decays since the relationship between the free-quark decay diagrams and the exclusive meson decay amplitudes is model dependent [6]. Also the strong phases that contribute to the

asymmetry cannot be reliably predicted. There are a few calculations of the asymmetry in these processes based on model-dependent estimates of the tree-to-penguin ratio of the amplitude. All such model-dependent calculations involve large theoretical uncertainties [6].

1.3.3 Indirect CP violation ($B^0 - \overline{B}^0$ mixing)

An initial B^0 may decay to a final state f, via two chains $B^0 \longrightarrow B^0 \longrightarrow f$, $B^0 \longrightarrow \overline{B}^0 \longrightarrow f$. Indirect CP violation is due to $B^0 - \overline{B}^0$ mixing, i.e. interference between the amplitudes of the two decay paths. The two mass eigenstates of the B meson can be

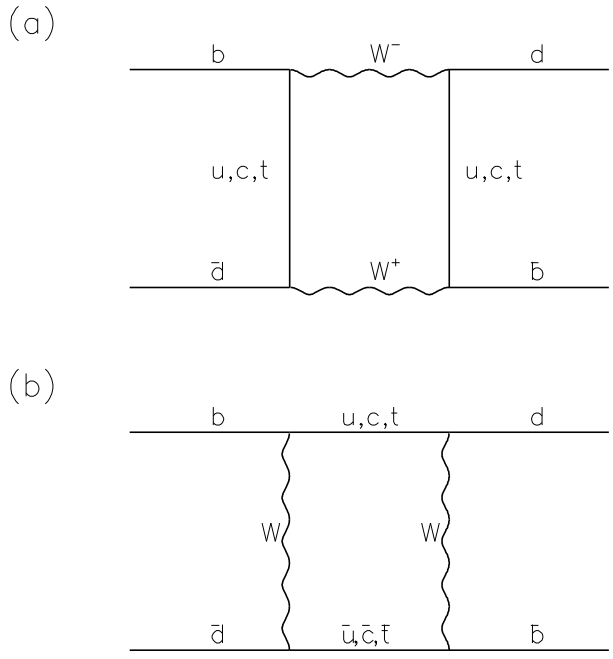

Figure 1.4: $B^0 - \overline{B}^0$ Mixing Diagrams.

written as:

$$\begin{aligned} B_L &= p|B^0> + q|\overline{B}^0> \\ B_H &= p|B^0> - q|\overline{B}^0>, \end{aligned}$$

where L and H indicate the light and heavy mass eigenstates. The widths of the two mass eigenstates are nearly equal and thus also the lifetimes.

$$\Gamma = (\Gamma_H + \Gamma_L)/2, \ \Delta\Gamma = \Gamma_H - \Gamma_L.$$

The mass difference is given by $\Delta M = M_H - M_L$. The proper time evolution of an initially (t=0) pure B^0 or $\overline{B}^0$ is given by:

$$\begin{aligned} |B^0(t)> &= \exp(-\Gamma t/2)\exp(-iM_1 t) \\ &\quad \times \left\{\cos(\Delta M t/2)|B^0> + i(q/p)\sin(\Delta M t/2)|\overline{B}^0>\right\} \qquad (1.11) \\ |\overline{B}^0(t)> &= \exp(-\Gamma t/2)\exp(-iM_2 t) \\ &\quad \times \left\{\cos(\Delta M t/2)|\overline{B}^0> + i(p/q)\sin(\Delta M t/2)|B^0>\right\}, \qquad (1.12) \end{aligned}$$

where M_1 is the mass of B^0 and M_2 is the mass of $\overline{B^0}$ ($M_1 = M_2$ by CPT invariance). If $|p/q|$ =1 and neglecting the effects of $\Delta\Gamma$, the probability that an initial $B^0(\overline{B}^0)$ decays as a $\overline{B}^0(B^0)$ is then

$$P(t) = \frac{1}{2}e^{-\Gamma t}(1 - \cos\Delta M t). \qquad (1.13)$$

Defining the amplitudes of B^0 and $\overline{B}^0$ to a CP eigenstate f by:

$$\begin{aligned} A \equiv A(B^0 \longrightarrow f) &= A_1 e^{i\phi_T}e^{i\delta_T} + A_2 e^{i\phi_P}e^{i\delta_P} \\ \overline{A} \equiv A(\overline{B}^0 \longrightarrow f) &= A_1 e^{-i\phi_T}e^{i\delta_T} + A_2 e^{-i\phi_P}e^{i\delta_P} \end{aligned}$$

and

$$\zeta = \frac{q}{p}\frac{\overline{A}}{A},$$

the time-dependent rates for initially pure B^0 or $\overline{B^0}$ states to decay into a final CP eigenstate at time t is given by:

$$\begin{aligned} \Gamma(B^0(t) \longrightarrow f) &= \frac{1}{2}|A|^2 e^{-\Gamma t} \times \\ &\quad \left[(1+|\zeta|^2) + (1-|\zeta|^2)\cos(\Delta M t) - 2Im\zeta\sin(\Delta M t)\right] \qquad (1.14) \\ \Gamma(\overline{B}^0(t) \longrightarrow f) &= \frac{1}{2}|A|^2 e^{-\Gamma t} \times \\ &\quad \left[(1+|\zeta|^2) - (1-|\zeta|^2)\cos(\Delta M t) + 2Im\zeta\sin(\Delta M t)\right]. \qquad (1.15) \end{aligned}$$

The time dependent CP asymmetry is then defined by:

$$\begin{aligned} a_f(t) &= \frac{\Gamma(B^0(t) \longrightarrow f) - \Gamma(\overline{B}^0(t) \longrightarrow f)}{\Gamma(B^0(t) \longrightarrow f) + \Gamma(\overline{B}^0(t) \longrightarrow f)} \\ &= \frac{(1-|\zeta|^2)\cos(\Delta M t) - 2Im\zeta\sin(\Delta M t)}{1+|\zeta|^2}. \qquad (1.16) \end{aligned}$$

There are two contributions to the asymmetry. The cos term is the asymmetry due to CP violation in the decays of the B^0 and $\overline{B}^0$ to the CP eigenstate f. It follows from the

equation that $|\zeta|$ must not be equal to one for direct CP violation to occur. This requires having two amplitudes A_1 and A_2 with different CKM phases $\phi_T \neq \phi_P$ and different final states hadronic interactions, $\delta_T \neq \delta_P$. The second term, which is the sin term, is the asymmetry induced by the interference of amplitudes of the B^0 and $\overline{B}^0$ via mixing. Eqn. 1.16 can be written as $a(t) = a_-(t) + a_+(t)$, where

$$a_-(t) = \frac{-2Im\zeta}{1+|\zeta|^2}\sin(\delta Mt). \tag{1.17}$$

This asymmetry requires measuring the time order of the B^0 and $\overline{B}^0$ decays to the final state f. The second asymmetry

$$a_+(t) = \frac{1-|\zeta|^2}{1+|\zeta|^2}\cos(\delta Mt), \tag{1.18}$$

can be measured without determining the time order of the two B decays. For $|A_2/A_1| \ll 1$, to first order in $|A_2/A_1|$,

$$\frac{2Im\zeta}{1+|\zeta|^2} \simeq -\sin(2\phi) + 2\frac{|A_2|}{|A_1|}\cos(2\phi)\sin(\phi_T-\phi_P)\cos(\delta_T-\delta_P) \tag{1.19}$$

$$\frac{1-|\zeta|^2}{1+|\zeta|^2} \simeq -2\frac{|A_2|}{|A_1|}\sin(\phi_T-\phi_P)\sin(\delta_T-\delta_P), \tag{1.20}$$

where $\phi = \phi_M + \phi_D$. The unknown final state interaction phases makes it impossible to determine $\sin 2\phi$ from measurements of the two constant coefficients describing the asymmetries $a_-(t)$ and $a_+(t)$. With the exception of situations where $|A_2/A_1|$ is very small, large values of $\sin(\phi_T - \phi_P)$ significantly modify small values of $\sin 2\phi$. The effect of the penguin amplitude is expected to be small for Cabibbo-allowed decays (corresponding to $b \longrightarrow c\overline{c}s$), significant for "once-Cabibbo-suppressed" decays ($b \longrightarrow c\overline{c}d$, $b \longrightarrow u\overline{u}d$) and very large for "twice-Cabibbo-suppressed decays" ($b \longrightarrow u\overline{u}s$) as shown in Table 1.3 [7]. In the approximation of neglecting penguin contribution, i.e. assuming only one decay amplitude occurs, then $|A| = |\overline{A}|$ and that no CP violation occurs in the mixing, so $|p/q| = 1$, then $|\zeta| = 1$. The rate equations in eqns. 1.14 and 1.15 then become:

$$\Gamma(B^0(t) \longrightarrow f) = |A|^2 e^{-\Gamma t}\left[1 + \sin(2\phi)\sin(\Delta Mt)\right] \tag{1.21}$$

$$\Gamma(\overline{B}^0(t) \longrightarrow f) = |A|^2 e^{-\Gamma t}\left[1 - \sin(2\phi)\sin(\Delta Mt)\right]. \tag{1.22}$$

The cos term in eqn. 1.16 vanishes and the time dependent rate asymmetry is

$$a(t) = \sin(2\phi)\sin(\Delta Mt), \tag{1.23}$$

Quark process	Final state	Spectator coupling	Penguin coupling	$\lvert A_2/A_1\rvert$
$b \longrightarrow c\bar{c}s$	$K_s\Psi$	λ^2	$(\lambda^5$ to $\lambda^4)\frac{\alpha_s}{12\pi}\ln\frac{m_t^2}{m_c^2}$	λ^6 to λ^3
$b \longrightarrow c\bar{c}d$	D^+D^-	λ^3	$(\lambda^4$ to $\lambda^3)\frac{\alpha_s}{12\pi}\ln\frac{m_t^2}{m_c^2}$	λ^4 to λ
$b \longrightarrow u\overline{u}d$	$\pi^+\pi^-$	$(\lambda^4$ to $\lambda^3)$	$(\lambda^3$ to $2\lambda^3)\frac{\alpha_s}{12\pi}\ln\frac{m_t^2}{m_c^2}$	$2\lambda^3$ to 1
$b \longrightarrow u\overline{u}s$	$K_s\pi^0$	λ^5 to λ^4	$\alpha^2\frac{\alpha_s}{12\pi}\ln\frac{m_t^2}{m_c^2}$	λ to λ^{-2}

Table 1.3: Spectator and penguin couplings in $\overline{B}^0_d$ decays to CP eigenstates.

where $e^{-2i\phi_M} = q/p$ and $e^{-2i\phi_D} = \overline{A}/A$. The time integrated asymmetry is then given by

$$a = \frac{\sin(2\phi)(\Delta M/\Gamma)}{1+(\Delta M/\Gamma)^2}. \tag{1.24}$$

1.3.4 Isospin and SU(3) symmetry

As we have seen in section 1.3.3, the time-dependent CP rate asymmetry $a(t) \propto \sin 2\alpha$, neglecting penguin contributions. If we take penguin contributions into account, then we have $a(t) \propto \sin(2\alpha + \theta_{+-})$, where θ_{+-} depends on the strong and weak phase contributions due to direct CP violation [8] (see eqns. 1.19 and 1.20) and the situation becomes more complicated. In order to get clean information on the CKM phase α, θ_{+-} has to be measured. The strong phases are incalculable thus rendering θ_{+-} incalculable as well. However there are two techniques that can be used to separate the weak and strong phases: isospin analysis and SU(3) symmetry. The formalism of isospin analysis is discussed in the next section and an example of its application is described in chapter 4.

1.3.5 Isospin analysis

This analysis described in chapter 4 is based on isospin symmetry. The idea is to use isospin to relate the three amplitudes $A^{+-}(B^0_d \longrightarrow \pi^+\pi^-)$, $A^{00}(B^0_d \longrightarrow \pi^0\pi^0)$ and $A^{+0}(B^+ \longrightarrow \pi^+\pi^0)$, and similarly for the CP-conjugate processes. Figs. 1.3 and 1.5 show the tree and penguin diagrams for the three decays. The tree diagrams generally represents the QCD-corrected left-handed four-fermion terms of the low-energy effective

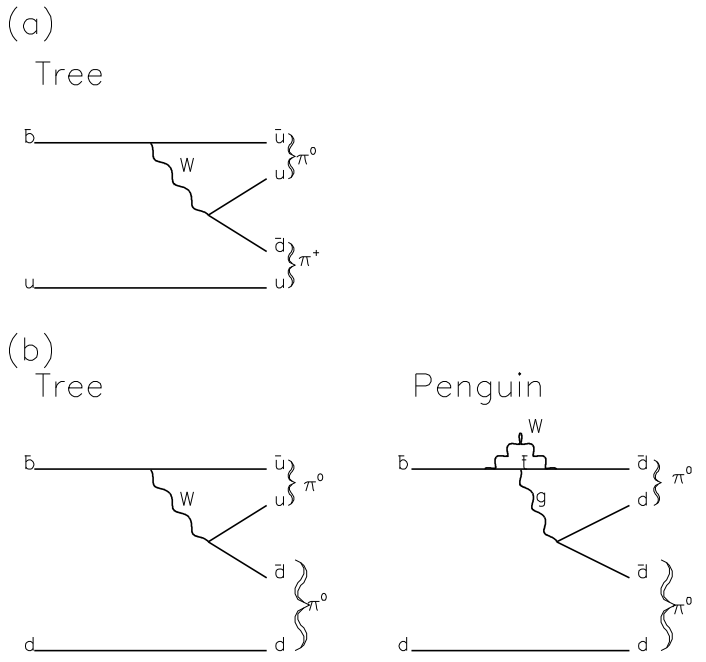

Figure 1.5: Diagrams contributing to the processes (a) $B_u^+ \longrightarrow \pi^0\pi^+$ and (b) $B_d^0 \longrightarrow \pi^0\pi^0$.

Hamiltonian. The penguin diagrams describe the W-loop QCD-induced terms due to pure gluon exchange. In the next-to-leading order approximation, the effective Hamiltonian for charmless B meson decays can be parametrised as [9]

$$H = \frac{G_F}{\sqrt{2}}\left[V_{ub}V_{uq}^*(c_1O_1^u + c_2O_2^u) - V_{tb}V_{tq}^*\sum_{i=3}^{10} c_iO_i\right] + h.c. \tag{1.25}$$

where h.c is the hermitian conjugate, and c_i are the so-called Wilson coefficients. O_i are defined as:

$$O_1^u = \overline{q}_\alpha\gamma^\mu(1-\gamma^5)u_\beta\overline{u}_\beta\gamma^\mu(1-\gamma^5)b_\alpha \tag{1.26}$$

$$O_2^u = \overline{q}\gamma_\mu(1-\gamma^5)u\overline{u}\gamma^\mu(1-\gamma^5)b \tag{1.27}$$

$$O_3 = \overline{q}\gamma_\mu(1-\gamma^5)b\sum_{q'}\overline{q}'\gamma_\mu(1-\gamma^5)q' \tag{1.28}$$

$$Q_4 = \overline{q}_\alpha\gamma_\mu(1-\gamma^5)b_\beta\sum_{q'}\overline{q}_{\beta'}\gamma_\mu(1-\gamma^5)q'_\alpha \tag{1.29}$$

$$O_5 = \overline{q}\gamma_\mu(1-\gamma^5)b\sum_{q'}\overline{q}'\gamma^\mu(1+\gamma^5)q' \tag{1.30}$$

$$Q_6 = \overline{q}_\alpha\gamma_\mu(1-\gamma^5)b_\beta\sum_{q'}\overline{q}_{\beta'}\gamma_\mu(1+\gamma^5)q'_\alpha \tag{1.31}$$

$$O_7 = \frac{3}{2}\overline{q}\gamma_\mu(1-\gamma^5)b\sum_{q'} e_{q'}\overline{q}'\gamma^\mu(1+\gamma^5)q' \quad (1.32)$$

$$O_8 = \frac{3}{2}\overline{q}_\alpha\gamma_\mu(1-\gamma^5)b_\beta\sum_{q'} e_{q'}\overline{q}_{\beta'}\gamma_\mu(1+\gamma^5)q'_\alpha \quad (1.33)$$

$$O_9 = \frac{3}{2}\overline{q}\gamma_\mu(1-\gamma^5)b\sum_{q'} e_{q'}\overline{q}'\gamma^\mu(1-\gamma^5)q' \quad (1.34)$$

$$O_{10} = \frac{3}{2}\overline{q}_\alpha\gamma_\mu(1-\gamma^5)b_\beta\sum_{q'} e_{q'}\overline{q}_\beta\gamma_\mu(1-\gamma^5)q'_\alpha. \quad (1.35)$$

O_1, O_2 are the tree level and QCD corrected operators and q is either a d or s quark. O_{3-6} are the strong gluon-induced operators. O_{7-10} are electroweak operators and are due to γ and Z exchange and "box" diagrams at loop level. This leaves $O_{1,2}$ with two isospin components, two isospin components for the electroweak penguins and only one isospin component for the strong penguin. The electroweak penguin contribution compared with the strong penguin contribution is suppressed by a factor α_{em}/α_s and therefore neglected. However some model calculations suggests that this may not be a valid approximation [9]. The $\Delta I = 3/2$ operator occurs purely as a tree diagram, but $\Delta I = 1/2$ operator has both tree and penguin contributions. For B_d^0 decays to $\pi^+\pi^-$, $\pi^0\pi^0$ and $B_u^+ \longrightarrow \pi^+\pi^0$ final states, $q = d$. The final state pions have isospin $I = 0$, 1, or 2. By Bose symmetry total isospin I for the two final state pions is 0 or 2. The effective Hamiltonian contains $\Delta I = 1/2$ and ΔI=3/2 amplitudes. The $\Delta I = 1/2$ component will contribute to decay amplitudes with $I = 0$ and 1 in the final states and the $\Delta I = 3/2$ component will contribute to amplitudes with I=1 and I=2 in the final states. The ratio of penguin to tree amplitudes for $B^+ \longrightarrow \pi^+\pi^0$ is:

$$A_{tree}(B^+ \longrightarrow \pi^+\pi^0) = -\frac{G_F}{\sqrt{2}}V_{ub}^*V_{ud}(c_1' + c_2')(1+\xi)T \quad (1.36)$$

$$\begin{aligned} A_{penguin}(B^+ \longrightarrow \pi^+\pi^0) = \frac{G_F}{\sqrt{2}}V_{tb}^*V_{td}\frac{3}{2}(c_7' + \xi c_8' + \\ c_9' + \xi c_{10}' + \xi c_9' + c_{10}' + \\ \frac{2}{3}(\xi c_7' + c_8')(2W + X))T, \end{aligned} \quad (1.37)$$

where ξ =1/N, N being the number of colours, W=$m_\pi^2/(m_d+m_u)(m_b-m_d)$, X=$m_\pi^2/2m_d(m_b-m_d)$ and T=$if_{\pi^0}[f_{B\pi^-}^+(m_B^2-m_\pi^2) + f_{B\pi^-}^- m_\pi^2]$. f_{π^0} (= 93 MeV) is the pion decay constant. The ratio of penguin and tree amplitudes in the factorisation

approximation i.e. independent of form factors, is then given by

$$\frac{|A_{penguin}(B^+ \longrightarrow \pi^+\pi^0)|}{|A_{tree}(B^+ \longrightarrow \pi^+\pi^0)|} \approx 0.016(|V_{td}|/|V_{ub}|), \tag{1.38}$$

neglecting a small contribution of about 0.005 due to strong isospin. The ratio of penguin to tree amplitudes for $B^0 \longrightarrow \pi^+\pi^-$ is $0.07(|V_{td}|/|V_{ub}|)$. For $B^0 \longrightarrow \pi^0\pi^0$, the ratio is $0.23(|V_{td}|/|V_{ub}|)$. The larger penguin effect in $B^0 \longrightarrow \pi^0\pi^0$ is attributed to colour suppression of the tree contributions. From eqn. 1.38 we can assume that the process $B^+ \longrightarrow \pi^+\pi^0$ arises solely from the tree diagram (ΔI=3/2) i.e. there is no penguin contribution. Making this assumption, we then expand the amplitudes for $B^0_d \longrightarrow \pi^+\pi^-$, $B^0_d \longrightarrow \pi^0\pi^0$ and $B^+_u \longrightarrow \pi^+\pi^0$ (A^{+-}, A^{00} and A^{+0} respectively) in terms of I=0 and I=2 pieces. Writing $\pi^+\pi^- = (\pi^+_1\pi^-_2 + \pi^-_1\pi^+_2)/\sqrt{2}$ and similarly for $\pi^+\pi^0$ and evaluating the Clebsch-Gordan coefficients, we obtain:

$$(1/\sqrt{2})A^{+-} = A_{i2} - A_{i0}$$

$$A^{00} = 2A_{i2} + A_{i0}, \quad A^{+0} = 3A_{i2} \tag{1.39}$$

where A_{i0} and A_{i2} are the amplitudes for a B to decay to a $\pi\pi$ with $I = 0$ and 2 respectively. There is a similar relation for the CP-conjugate processes. These give the triangle relations:

$$\frac{1}{\sqrt{2}}A^{+-} + A^{00} = A^{+0} \tag{1.40}$$

$$\frac{1}{\sqrt{2}}\overline{A}^{+-} + \overline{A}^{00} = \overline{A}^{-0}, \tag{1.41}$$

where $\overline{A}^{+-}$, $\overline{A}^{00}$ and $\overline{A}^{-0}$ are the amplitudes for the charge-conjugated processes $\overline{B}^0_d \longrightarrow \pi^+\pi^-$, $\overline{B}^0_d \longrightarrow \pi^0\pi^0$ and $B^- \longrightarrow \pi^-\pi^0$ respectively.

Since only a tree-level diagram is involved in charged B decays,

$$A_{i2} = |A_{i2}|e^{i\phi_T}e^{i\delta_{i2}}, \quad \overline{A_{i2}} = |A_{i2}|e^{-i\phi_T}e^{i\delta_{i2}}, \tag{1.42}$$

where δ_{i2} is the $I = 2$ final-state-interaction phase and ϕ_T is the tree-level CKM phase. Thus $|A_{i2}| = |\overline{A}_{i2}|$ and $|A^{+0}| = |\overline{A}^{-0}|$. For neutral B decays there are both tree and penguin contributions to A_{i0} . Also mixing has to be taken into account to measure $|A^{+-}|$, $|\overline{A}^{+-}|$, $|\overline{A}^{00}|$ and $|A^{00}|$. The time dependence of $B^0_d \longrightarrow f$ and $\overline{B}^0_d \longrightarrow \overline{f}$ decays is given in eqn. 1.12. The existence of a $\cos(\Delta Mt)$ term in eqn. 1.16 is due to direct

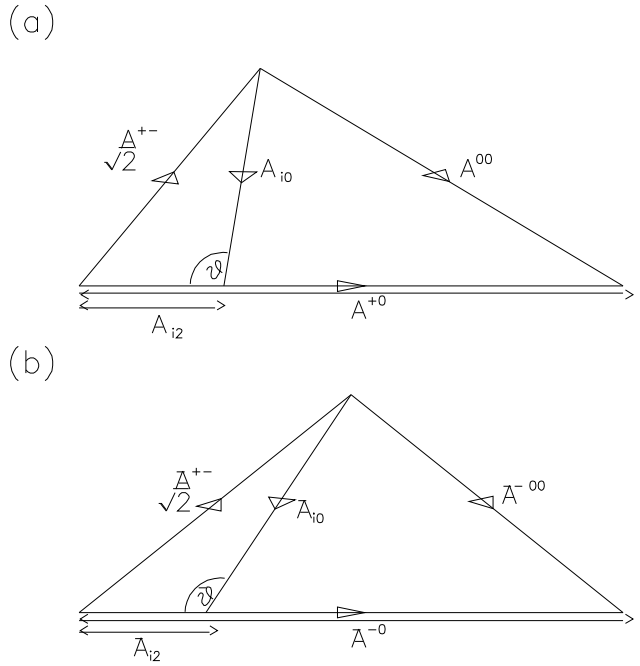

Figure 1.6: Isospin triangles in $B \longrightarrow \pi\pi$.

CP violation. In the approximation of neglecting penguin contributions, $|A| = |\overline{A}|$ and $|\zeta| = 1$ and the $\cos(\Delta M t)$ term disappears. The $\sin(\Delta M t)$ term is CP violating due to interference of the amplitudes of A and $\overline{A}$. Its coefficient for the $\pi^+\pi^-$ final state is given by

$$Im\zeta_{+-} = Im\left[e^{2i\alpha}\left[\frac{1-\overline{z}}{1-z}\right]\right] = Im\left[e^{2i\alpha}\left[\frac{1-|\overline{z}|e^{\pm i\overline{\theta}}}{1-|z|e^{\pm i\theta}}\right]\right], \tag{1.43}$$

where from eqns. 1.39 and 1.42

$$z \equiv A_{i0}/A_{i2},\ \overline{z} \equiv \overline{A}_{i0}/\overline{A}_{i2}. \tag{1.44}$$

θ and $\overline{\theta}$ are as shown in fig. 1.6. If penguin contributions are neglected, then $z = \overline{z}$ and $Im\zeta_{+-} = \sin 2\alpha$. On the other hand if we take penguins into account, then $z \neq \overline{z}$ and we then need to determine their magnitude and phases to measure α. Hence we need to evaluate the equation

$$Im\zeta_{+-} = Im\left[e^{2i\alpha}\left[\frac{1-|\overline{z}|e^{\pm i\overline{\theta}}}{1-|z|e^{\pm i\theta}}\right]\right]. \tag{1.45}$$

A_{i2} in fig. 1.6 can be obtained from $|A^{+-}|$ in eqn. 1.39. Using simple trigonometry from

the triangles of fig. 1.6, z, $|\overline{z}|$, θ and $\overline{\theta}$ can all be evaluated. Eqn. 1.45 can be written as

$$Im\zeta_{+-} = Im\left[e^{2i\alpha}M_{+-}\right], \tag{1.46}$$

where M_{+-} is the term in square brackets and can have four different phases: $\pm\varepsilon_{+-}$ and $\pm\varrho$ which are functions of $|z|$, $|\overline{z}|$, θ and $\overline{\theta}$. Thus we have

$$Im\zeta_{+-} = |M_{+-}|\sin(2\alpha \pm \varepsilon_{+-}), \tag{1.47}$$

$$Im\zeta_{+-} = |M_{+-}|\sin(2\alpha \pm \varrho_{+-}) \tag{1.48}$$

which leaves a fourfold ambiguity in the determination of $\sin 2\alpha$. Eqn. 1.46 can be expanded fully as

$$\begin{aligned} Im\zeta_{+-} &= 2[\sin 2\alpha(|A_{i2}|^2 - |A_{i2}|(|\overline{A_{i0}}|\cos\overline{\theta} + |A_{i0}|\cos\theta) + |A_{i0}||\overline{A_{i0}}|\sin(\theta-\overline{\theta})) \\ &\quad + \cos 2\alpha(|A_{i2}|(|\overline{A_{i0}}|\sin\overline{\theta} - |A_{i0}|\sin\theta) + |A_{i0}||\overline{A_{i0}}|\sin(\theta-\overline{\theta}))]. \end{aligned} \tag{1.49}$$

We have thus shown that the value α can be separated from penguin contribution using isospin symmetry.

1.3.6 Current experimental limits of CP violation studies in the B system

The BABAR, CLEO III, BELLE, CDF, $D0$ and HERA-B experiments are likely to detect CP violation in B meson decays but are unlikely to answer all the important questions. For instance measurement of the CKM Matrix element γ requires a very high luminosity and will probably not be attained at B-factories, HERA-B, CDF or $D0$. Another problem is that recent experimental work suggests that the branching fraction of $B^0 \longrightarrow \pi\pi$ may be smaller than was expected [10]. Table 1.4 shows early predictions of the CP sensitivity expected to be achieved on $\sin 2\beta$ and $\sin 2\alpha$ by BELLE, BABAR, BTEV and LHC-B. The B_s mixing parameter is large, which means that excellent time resolution and large statistics are needed to measure it. The above problems suggests that the future of these investigations lies with hadron collider experiments which provide a much higher rate of B hadrons to work with.

Experiment	Data sample	$\delta[\sin 2\alpha]$	$\delta[\sin 2\beta]$
BELLE	100 fb^{-1}	0.092	0.062
BABAR	30 fb^{-1}	0.085	0.059
BTEV	500 pb^{-1}	0.100	0.042
LHC-B	500 pb^{-1}	0.039	0.023

Table 1.4: CP reach estimates for BELLE, BABAR, BTEV and LHC-B accumulated on the $\Upsilon(4S)$ resonance. The results are based on a GEANT Monte Carlo simulation of the detectors done for the Technical Design Reports [12][13][14].

The Standard Model predicts very low rates and small effects in mixing and CP violation in charm. Thus charm physics provides an excellent place for any discovery of new physics beyond the Standard Model. On a time scale and performance, BTEV and LHC-B would represent a next generation of hadron collider experiment beyond HERA-B, CDF and $D0$. BTEV is a better charm experiment than any current or planned because of its huge event rate, powerful trigger and vertexing capability. Hence any signal from new physics is likely to be observed in the charm sector at BTEV [14].

1.3.7 CP violation in the neutral Kaon sector

The strangeness hypothesis requires there to be two distinct neutral Kaons– a K^0 and $\overline{K}^0$. These are the strong interaction eigenstates of definite flavour. The weak interactions split linear combinations of these states into ones with definite mass and lifetime. The weak eigenstates of the $K^0 - \overline{K}^0$ system can be written as:

$$|K_S> \;=\; p|K^0> + q|\overline{K}^0> \tag{1.50}$$

$$|K_L> \;=\; p|K^0> - q|\overline{K}^0> . \tag{1.51}$$

Under CP invariance, $q = p$ so that K_S would be CP even and can couple to the CP even 2π state, which is short-lived. The K_L is CP odd and long-lived since it cannot decay to 2π but only to three-body final states. The discovery in 1964 [15] that the long-lived neutral Kaon also decays to 2π showed that CP is not a valid symmetry of the weak interactions. CP violation in the Kaon system is similar to the B system. There are two

contributions: $K^0 - \overline{K}^0$ mixing and direct CP violation. For K_L and K_S decays to two final state pions, if there is CP violation, eqns. 1.50 and 1.51 can be written as:

$$|K_S> = \frac{1}{\sqrt{2(1+|\epsilon|^2)}}\left((1+\epsilon)|K^0> +(1-\epsilon)|\overline{K}^0>\right) \tag{1.52}$$

$$|K_L> = \frac{1}{\sqrt{2(1+|\epsilon|^2)}}\left((1+\epsilon)|K^0> -(1-\epsilon)|\overline{K}^0\right), \tag{1.53}$$

where

$$\epsilon = \frac{ImM_{12} - \frac{1}{2}iIm\Gamma_{12}}{i\Delta m - \frac{1}{2}(\Gamma_S - \Gamma_L)}. \tag{1.54}$$

$M_{12} =< K^0|M|\overline{K}^0 >$, $\Gamma_{12} =< K^0|\Gamma|\overline{K}^0 >$ and $\Delta m = m_L - m_S$.

If we define:

$$|K_1> \approx |K^0> +|\overline{K}^0> \qquad (\text{CP} = +1) \tag{1.55}$$

$$|K_2> \approx |K^0> -|\overline{K}^0> \qquad (\text{CP} = \text{-1}), \tag{1.56}$$

then the weak interaction eigenstates K_S and K_L may be written as:

$$|K_S> = \frac{1}{\sqrt{1+\epsilon^2}}(|K_1> +\epsilon|K_2>) \tag{1.57}$$

$$|K_L> = \frac{1}{\sqrt{1+\epsilon^2}}(|K_2> +\epsilon|K_1>). \tag{1.58}$$

The parameter ϵ describes the amount of the "wrong" CP eigenstate in the weak eigenstates. We may define

$$\eta_{+-} \equiv \frac{A(K_L \longrightarrow \pi^+\pi^-)}{A(K_S \longrightarrow \pi^+\pi^-)} = |\eta_{+-}|e^{i\phi_{+-}}, \tag{1.59}$$

and similarly

$$\eta_{00} \equiv \frac{A(K_L \longrightarrow \pi^0\pi^0)}{A(K_S \longrightarrow \pi^0\pi^0)} = |\eta_{00}|e^{i\phi_{00}}. \tag{1.60}$$

If $K_L \longrightarrow \pi\pi$ is purely due to mixing then, $\eta_{+-} = \eta_{00} = \epsilon$. This implies

$$|\eta_{+-}| = |\eta_{00}| \tag{1.61}$$

and

$$\phi_{+-} = \phi_{00} = \arctan\left(\frac{\Delta m}{\Gamma_S - \Gamma_L}\right), \tag{1.62}$$

where ϕ_{+-} and ϕ_{00} are the phases of η_{+-} and η_{00} respectively. If there is direct CP violation in addition to the mixing, we have K decay amplitudes given by

$$A(K \longrightarrow \pi\pi) = A_I e^{i\delta_I}, \tag{1.63}$$

CP Parameter	E731 Results	NA31 Results
$\mathrm{Re}(\epsilon'/\epsilon) \times 10^{-4}$	7.4 ± 5.9	23 ± 6.5
$\tau_s[\times 10^{-10} s]$	0.8929 ± 0.0016	0.902 ± 0.005
$\Delta m[\times 10^{10} \hbar s^{-1}]$	0.5286 ± 0.0028	0.5351 ± 0.0024
$\Delta\phi$	-1.6 ± 1.2	0.2 ± 2.6
ϕ_{+-}	42.2 ± 1.5	46.9 ± 1.4

Table 1.5: Recent published measurements of CP parameters in the neutral Kaon system from the FNAL E731 detector at Fermilab and NA31 experiment at CERN.

where I = 0, 2 is the isospin of the final state and δ_I is the $\pi\pi$ scattering phase-shift at the K mass.

We then have:

$$\eta_{+-} = \epsilon + \epsilon' \tag{1.64}$$

$$\eta_{00} = \epsilon - 2\epsilon', \tag{1.65}$$

where

$$\epsilon' = \frac{i}{\sqrt{2}} Im\left(\frac{A_2}{A_0}\right) e^{i(\delta_2 - \delta_0)}. \tag{1.66}$$

It then follows that:

$$Re\left(\frac{\epsilon'}{\epsilon}\right) \approx \frac{1}{6}\left(1 - \left|\frac{\eta_{00}}{\eta_{+-}}\right|^2\right) \tag{1.67}$$

$$\frac{|\eta_{+-}|^2}{|\eta_{00}|^2} \approx 1 + 6Re(\epsilon'/\epsilon). \tag{1.68}$$

The deviation of the ratio $|\eta_{+-}|^2/|\eta_{00}|^2$ from unity is a signal for direct CP violation. However the deviation ($Re(\epsilon'/\epsilon)$) is expected to be small. Recent results from experiments at Fermilab in the neutral Kaon system have given values of the CP violation parameters $\mathrm{Re}(\epsilon'/\epsilon)$, τ_s, Δm, $\Delta\phi$ and ϕ_{+-}. The results are given in Table 1.5 [16]. The value of $\mathrm{Re}(\epsilon'/\epsilon)$ from the NA31 experiment at CERN does not well agree with the value from Fermilab. The Standard Model prediction of $\mathrm{Re}(\epsilon'/\epsilon)$ is $(3 \pm 4) \times 10^{-4}$ [16] which agrees better with the Fermilab value than with the NA31 value. However both experiments are on the way to improve the level of precision. Two new experiments, FNAL E832 at Fermilab and NA48 at CERN hope to determine ϵ'/ϵ with a precision in the range of

$1 - 2 \times 10^{-4}$. Using new beams and detectors they will increase the statistics (the results quoted are statistically limited) and reduce systematic uncertainties. The CPLEAR (low-energy antiproton ring for the study of CP violation) experiment at CERN has also

CP Parameter	Value
$\|\eta_{+-}\|[\times 10^{-3}]$	$2.312 \pm 0.043 \pm 0.032$
$\phi_{+-}[deg]$	$42.7 \pm 0.9 \pm 0.6$
$\phi_{00}[deg]$	$50.8 \pm 7.1 \pm 1.5$
$Re\ \eta_{+-0}[\times 10^{-3}]$	$6 \pm 13 \pm 1$
$Im\ \eta_{+-0}[\times 10^{-3}]$	$-2 \pm 18 \pm 3$
$\Delta m[\times 10^{10} \hbar s^{-1}]$	$0.5274 \pm 0.0029 \pm 0.0005$

Table 1.6: Recent measurements of CP parameters in the neutral Kaon system from the CPLEAR experiment at CERN. The results are based on data collected from 1990-1994. Δm was measured from semileptonic neutral K decays [17].

published results of measurements of CP violating parameters in two and three pion decays of the K meson. The results are given in Table 1.6 based on the 1990-1994 data. Another experiment, KLOE (K LOng Experiment), is designed to study Kaon physics at the Frascati INFN Laboratory (LNF) in Italy. It is schedule to begin in 1998. At a luminosity of 5×10^{32} cm$^2 s^{-1}$, 5×10^{10} Φs will be produced per year which then decay to two neutral Kaons. The KLOE detector is designed with a large geometrical acceptance to contain long-lived Kaon decays, good momentum and spatial resolution, good reconstruction efficiencies and background rejection. It aims to measure ϵ'/ϵ with a sensitivity of $\sim 10^{-4}$.

Due to large hadronic uncertainties a measurement of ϵ'/ϵ from K^0 decays to $\pi\pi$ provides limited useful information on the CKM quantities. Current experiments probably represent limit possible in sensitivity for the K system. With experimental developments now made possible, the B system will be a useful area to look for CP violation with better precision. However rare decay $K_L^0 \longrightarrow \pi^0 \nu\overline{\nu}$ offers interesting opportunities for precision measurements comparable to the B system. Several activities are under way to pursue this decay mode. The Standard Model prediction of the branching ratio is $(2.8 \pm 1.7) \times 10^{-11}$ [18]. Fermilab and KEK hope to measure the branching ratio with a

sensitivity in the order of 10^{-12} [19].

Chapter 2

CP violation with BABAR

2.1 Introduction

The PEP-II collider and the BABAR experiment have been designed primarily to study CP violation in B decays. The PEP-II collider (expected to begin operation in 1999) is an asymmetric e^+e^- collider with two independent rings, located on top of each other. At PEP-II, electrons and positrons will be accelerated to energies of 9 GeV and 3.1 GeV respectively and stored separately in the storage rings. The beams will then be collided head on with the aid of quadrupole magnets Q1, Q2, Q4, Q5 and B1 (see fig. 2.1) which will focus the beams to an interaction region. The centre of mass energy is 10.56 GeV corresponding to production of the $\Upsilon(4S)$ resonance. The $\Upsilon(4S)$ will then decay to charged and neutral B mesons

$$e^+e^- \longrightarrow \Upsilon(4S) \longrightarrow B^+B^-,\ B^0\overline{B}^0$$

where the pairs of charged and neutral B mesons are produced in approximately equal amounts. The asymmetric collision provides a boost of $\beta\gamma$ equals 0.56 in order to produce a measurable decay length for the B mesons. The initial luminosity is $3 \times 10^{33}\text{cm}^{-2}\text{s}^{-1}$. Surrounding the interaction point is the BABAR detector.

The main aim of BABAR is to explore in detail the Standard Model predictions concerning CP violation in the B sector and in particular to measure the asymmetries in B^0 mesons decay to CP eigenstates. It will also measure the magnitudes of V_{ub}, V_{cb} and V_{td} of the CKM matrix (see section 2.2). The CP asymmetry measurements will also give values for the CKM matrix elements $|V_{ub}|$ and $|V_{td}|$ (see eqns. 1.8 and 1.9 of

chapter 1). Accurate measured values of the CKM matrix elements over-constrains the unitarity triangle and gives the lengths of of its sides. This provides a useful means of probing the source of CP violation. Other elements of the CKM matrix have already been determined by other experiments. $|V_{ud}|$ has been measured from nuclear β decays and $|V_{us}|$ has been precisely measured using $K \longrightarrow \pi e \nu$ decays. $|V_{cd}|$ has been measured from neutrino and anti-neutrino charm production and $|V_{cs}|$ has been determined from charm decays. Measurements of $|V_{cb}|$ and $|V_{ub}/V_{cb}|$ have been made from semileptonic B meson decays. The results of the measured values are shown in Table 2.1

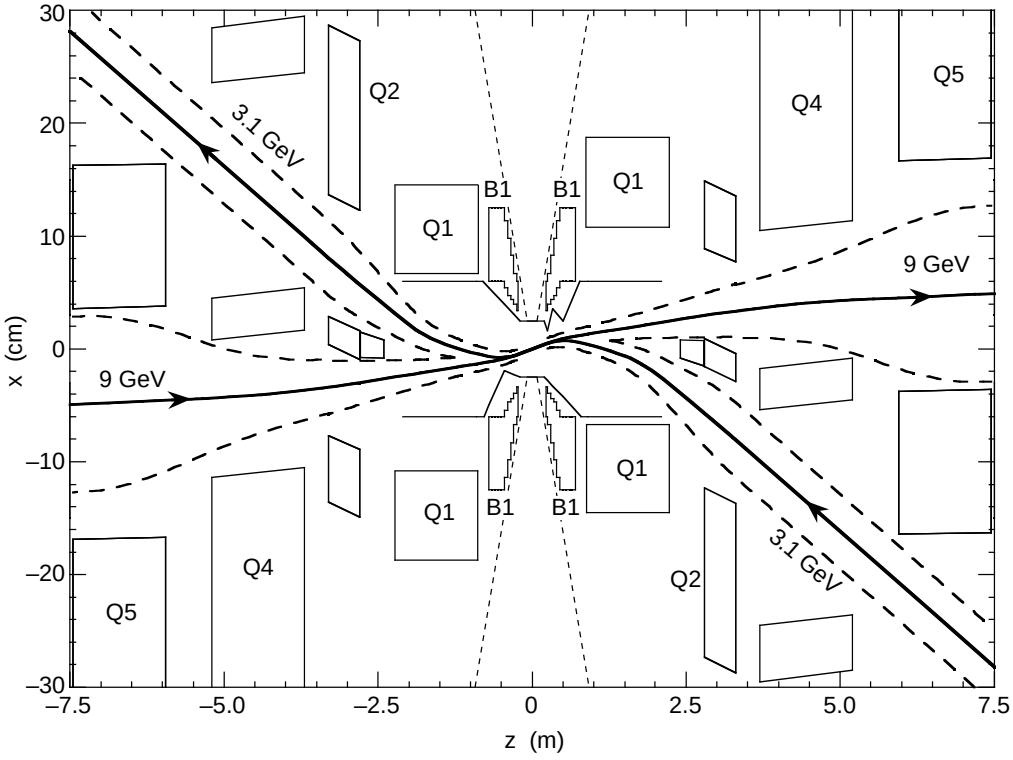

Figure 2.1: Plan view of the interaction region. The low-energy beam enters from the lower right and exits from the upper left. The high energy beam enters from the left and exits on the right. The vertical scale is highly exaggerated [11].

In figure 2.2 plots of the 95% confidence level allowed regions in the (ρ, η) plane of the unitarity triangle from current Standard Model measurements of Δm_d, ϵ_k and V_{ub}/V_{cb} are shown. Each shaded region correspond to the (ρ, η) values satisfying the equations relating to a measurement at the 95% confidence level (see equations of appendix A). The lines marking the boundaries of each region are the solutions in the (ρ, η) plane for the upper and lower limits of the relating measurement. The intercept of the various

CKM element	Measured Value
$\|V_{ud}\|$	0.9744 ± 0.0010
$\|V_{us}\|$	0.2205 ± 0.0018
$\|V_{cd}\|$	0.204 ± 0.017
$\|V_{cs}\|$	1.01 ± 0.18
$\|V_{cb}\|$	0.040 ± 0.005
$\|V_{ub}/V_{cb}\|$	0.08 ± 0.02

Table 2.1: Results of measurement of CKM matrix elements as given in reference [20].

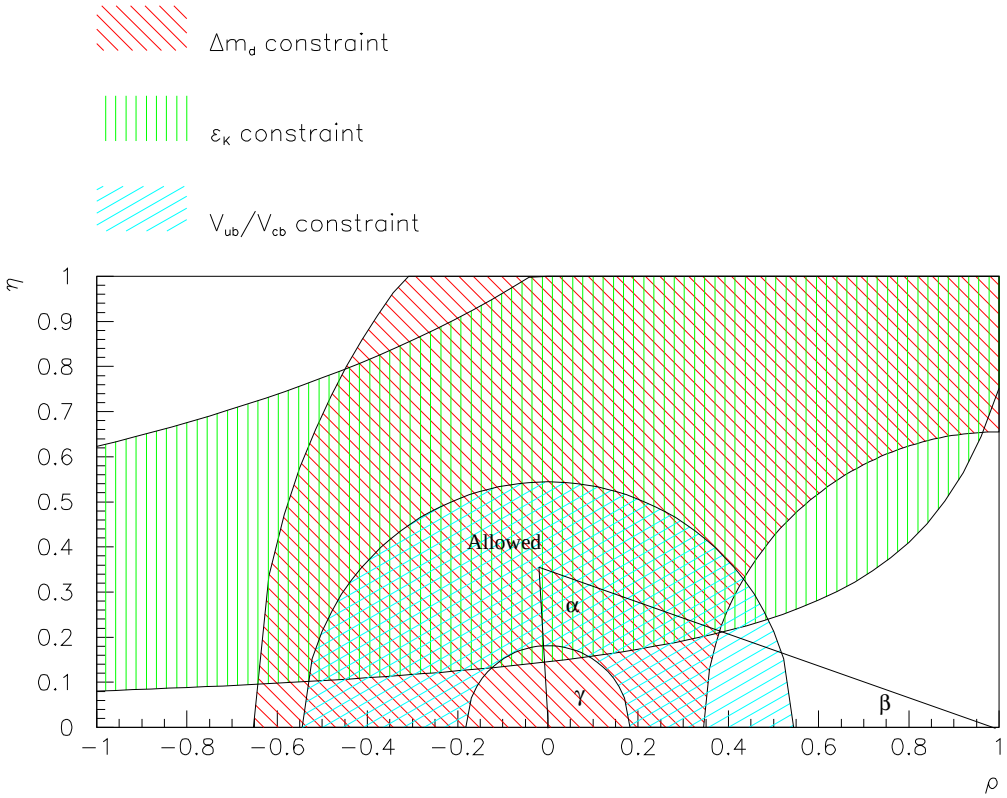

Figure 2.2: Plots showing the 95% confidence level region in the (ρ, η) plane of the unitarity triangle from current measurements of Δm_d, ϵ_k and V_{ub}/V_{cb}. The intersection of the shaded regions gives an indication of the allowed region for the apex of the triangle.

shaded zones signifies the Standard Model allowed region for the apex of the triangle. It is expected that measurements of CP asymmetry parameters will impose further constraints on this allowed region. BABAR will measure the elements V_{cb} and V_{ub} from semi-leptonic B decays such as $B \longrightarrow D^* l \nu_l$ (l is a lepton and ν_l is the lepton neutrino) and $B \longrightarrow X_u l \nu_l$ ($X_u = \pi$, ρ, or ω) respectively. In addition to these measurements, BABAR will also make searches for rare B decays such as $B \longrightarrow \tau\nu$, $s\gamma$, l^+l^- ($l = \tau$,μ, or e), $\gamma\gamma$ and also study charm, tau and two photon physics. Rare B decays offer a search for new physics. The Standard Model prediction for the branching ratio of $B \longrightarrow \gamma\gamma$ is very low (6×10^{-10}). This leaves plenty of opportunity for nonstandard effects to dominate. Dileptonic B decays such as $B \longrightarrow \mu e$ and τe are forbidden in the Standard Model. Search for such decay modes can expose weaknesses in the model [21]. Measurement of the branching ratio of $B \longrightarrow \tau\nu$ will give the value of the product $f_B^2 |V_{ub}|^2$, where f_B is the B-meson coupling constant. From this the CKM matrix element V_{ub} can be determined. With expected high D meson production rates at PEP-II, searches into $D\overline{D}$ mixing and CP violation in the charm sector will be feasible. Tau physics studies will be more difficult at BABAR due to expected large backgrounds from $q\overline{q}$ and two-photon physics. However with the expected large data sample, it will be possible for BABAR to uncover interesting physics beyond the Standard Model.

2.2 Overview of measurements to be made

2.2.1 Measurement of V_{ub} and V_{cb}

In semi-leptonic B decays, leptons from $b \longrightarrow u$ decays are primary leptons whilst $b \longrightarrow c$ decays produce both primary and secondary leptons, the secondary leptons coming from charm decays. For B decay to a charm final state, the lowest hadronic mass possible is that of the D^0 meson. This puts a limit of 2.32 GeV/c on the lepton momentum in the B rest frame. For $b \longrightarrow u$, the lowest hadronic mass possible is π^0 and the lepton momentum limit is 2.64 GeV/c. Hence by fitting the theoretical lepton momentum distribution to the experimental data, the relative contributions from $b \longrightarrow u$, $b \longrightarrow c$ and D meson decays can be determined and the magnitudes of the ratio of $|V_{ub}|/|V_{cb}|$ can be fixed as

well as the B meson semi-leptonic branching ratio. The fit function is of the form

$$T(p) = C_{cb}T_{cb}(p) + C_{ub}T_{ub}(p) + C_{cs}T_{cs}(p).$$

C_{cb}, C_{ub} and C_{cs} are the free parameters that will be obtained from the fit. T_{cb}, T_{ub} and T_{cs} are the theoretical momentum distributions for leptons from semi-leptonic decays $b \longrightarrow c$, $b \longrightarrow u$ and D meson decays. This method was used by CLEO, however it is model dependent and subject to theoretical errors. Another method is by measuring the charge and angular correlations of dilepton events. The measured correlations can be used to separate the primary and secondary leptons. Two classes of leptons are defined: isolated and non-isolated leptons. Isolated leptons are defined in the $\Upsilon(4S)$ centre of mass frame as those with no other charged track in the same hemisphere, i.e. at an angle of less than 90^o. This favours primary leptons from semi-leptonic B decays whilst the other class of lepton which is the complementary to the other, favours secondary leptons. The total energy of charged particles and photons in the same hemisphere as the lepton (for primary and secondary leptons) are correlated with the momentum. This helps to separate primary from secondary leptons. This method is not model dependent and hence free from theoretical errors. The statistical and systematic errors are better than the previous. A much better alternative method used by CLEO [22, 23] is by measuring the invariant mass of final hadrons in B-meson semi-leptonic decays. This selects $b \longrightarrow u$ and $b \longrightarrow c$ transitions more efficiently than the previous methods. The previous methods are basically centred on placing bounds on the lepton energy in the centre of mass frame to isolate the two transitions. To select $b \longrightarrow u$ transitions, it is required that

$$E_l > (m_B^2 - m_D^2 + m_l^2)/m_B,$$

where E_l ($l = e$, μ, or τ) is the energy of leptons in the centre of mass frame of $\Upsilon(4S)$, m_B is the mass of the B meson and m_D is the mass of the D meson. Since BABAR will use an asymmetric collider, the momenta of the leptons in the laboratory frame will have to be boosted to that of the centre of mass frame of $\Upsilon(4S)$. The disadvantage of this procedure is that it only selects 20% of $b \longrightarrow u$ transitions. A more efficient way is to measure the invariant mass of the final state hadrons m_x. To select $b \longrightarrow u$ events we require that $m_x < m_D$, where m_D is the mass of a D meson. With this method more than 90% of $b \longrightarrow u$ events are selected.

2.2.2 Measurement of V_{tb}

Indirect measurements of $|V_{tb}|$ will come from $B^0 - \overline{B}^0$ mixing (see fig. 1.4). The difference in the mass eigenstates of the two B mesons from the graphs is predicted to be [24]

$$\Delta M = \frac{G^2}{6\pi^2}|V_{tb}|^2|^2 m_W^2 m_B f_B^2 B_B \eta_B S(m_t^2/m_W^2) \tag{2.1}$$

where G is the Fermi coupling constant for weak decays, f_B is decay constant of the B meson, B_B is parameter describing the degree to which the two graphs dominate the mixing, η_B is a QCD correction and

$$S(x) \equiv \frac{x}{4}\left[1 + \frac{3-9x}{(x-1)^2} + \frac{6x^2 \ln x}{(x-1)^3}\right]$$

where $x = m_t^2/M_W^2$.

2.2.3 CP asymmetries in neutral B decays

Measurement of CP rate asymmetries in neutral B decays to CP eigenstates such as $B_d^0 \longrightarrow J/\Psi K_s^0$, $J/\Psi K_L^0$, $J/\Psi K^*$, D^+D^-, $D^{*+}D^{*-}$, $\pi^+\pi^-$ and $\rho\pi$ will be one of the important aspirations of BABAR in verifying CP violation. At PEP-II the $\Upsilon(4S)$ produced from the asymmetric e^+e^- collision is boosted in the forward direction. The boost energy is 6 GeV. The $\Upsilon(4S)$ decays to $B^0\overline{B}^0$ pair in a coherent state. This implies one neutral B meson cannot oscillate independently of the other. Since flavour is not conserved in weak interactions, the B^0 meson can transform to a $\overline{B}^0$ or the $\overline{B}^0$ to a B^0 before decaying. Thus we have interference of the amplitudes of the mixed and unmixed decays which leads to an asymmetry between the B^0 and $\overline{B}^0$. Due to this oscillation it is almost impossible to determine whether a B decay to a final state f was initially a B^0 or a $\overline{B}^0$ at time t_0 without tagging. The boost of 6 GeV ensures that the B mesons produced do not decay at their point of production. The very short lifetime of the B meson implies that without the boost the two B mesons will only travel a distance of 20 μm before decaying. This accuracy is beyond the capability of current detectors and will make it impossible to measure the decay positions. With the boost from the asymmetric collider, the two B mesons have a total momentum of about 6 GeV/c. Their average flight path before decay will then be about 250 μm. This makes it possible to measure the decay positions. By tagging, we reconstruct one B decay to CP eigenstate f and determine the flavour

of the other from its semi-leptonic decay. The flavour of one B tells the flavour of the other. The time-dependent asymmetry is a function of the proper lifetime difference (t) between the two B mesons and is given by

$$a(t) = \frac{N(B^0 - tag \longrightarrow f) - N(\overline{B}^0 - tag \longrightarrow f)}{N(B^0 - tag \longrightarrow f) + N(\overline{B}^0 - tag \longrightarrow f)} = D \sin(2\phi) \sin(\Delta M t), \qquad (2.2)$$

where $\phi = \alpha$, β or γ. D is the dilution factor and describes how much the amplitude of the

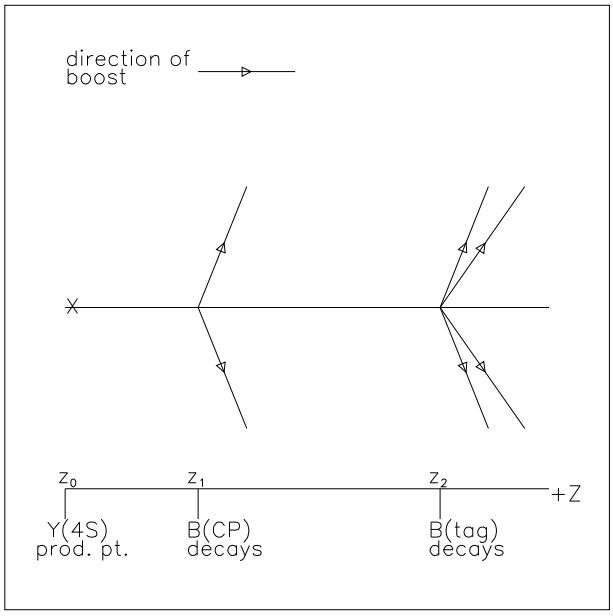

Figure 2.3: Flight paths of the B^0_d and $\overline{B}^0_d$ mesons produced at the $\Upsilon(4S)$ resonance.

time dependent CP-asymmetry is degraded due to wrong tags. It has two contributions known as D_t and D_r with $D_t = 1 - 2w$, where w is the wrong tag fraction due to tagging misidentification. The second contribution, D_r, is due to the finite resolution of the measured proper time difference (t) and is given by $D_r = e^{-\frac{1}{2}(x\sigma_t/\tau)^2}$, where τ is the lifetime of B^0, $x = \Delta M \tau$ is the mixing parameter, and σ_t is the resolution in t. The total dilution factor D is the product of D_t and D_r.

2.2.4 CP sensitivity

Measurements of $\sin 2\alpha$ will come from decay modes, $B^0 \longrightarrow \pi^+\pi^-$, $\rho\pi$ and $a_1\pi$. The decay modes $B^0 \longrightarrow J/\Psi K^0_s$, $J/\Psi K^0_L$, $J/\Psi K^*$, D^+D^- and $D^{*+}D^{*-}$ will give values for

CP Mode	Branching Ratio	Expected No. Events	CP Reach $\Delta[\sin(2\phi)]$
$\pi^+\pi^-$	1.2×10^{-5}	432	0.20
$\rho\pi$	5.8×10^{-5}	2088	0.11
$a_1\pi$	6×10^{-5}	2160	0.24
Combined			0.085
$J/\Psi K_s^0$	5×10^{-4}	2160	0.098
$J/\Psi K_L^0$	5×10^{-4}	2160	0.16
$J/\Psi K^*$	1.6×10^{-3}	788	0.19
D^+D^-	6×10^{-4}	993	0.21
$D^{*+}D^{*-}$	7×10^{-4}	3130	0.15
Combined			0.059

Table 2.2: Assumed branching ratios, cross sections and CP-reach estimates for B decays to CP Modes.

$\sin 2\beta$. In Table 2.2 [25] the results obtained from a fast parameterised Monte Carlo simulation of the BABAR detector conducted for the BABAR Technical Design Report, showing the number of events expected for B decays to CP modes for a standard year's running at design luminosity (corresponding to an integrated luminosity L=$30 fb^{-1}$) and the CP sensitivity for $\sin 2\alpha$ and $\sin 2\beta$ is presented. The combined sensitivity for $\sin 2\alpha$ and $\sin 2\beta$ is ± 0.085 and ± 0.059 respectively. Chapter four of this thesis reports a new study of the BABAR detector and the expected sensitivity on $\sin 2\alpha$.

2.3 The detector

The BABAR detector has as its main elements: a silicon vertex detector, a drift chamber, an internal reflected Cherenkov radiation detector (DIRC), an electromagnetic calorimeter, a superconducting solenoid and an instrumented flux return (hadron calorimeter). The DIRC and drift chamber form the particle identification system of the detector. Figs. 2.4 and 2.5 show a cross-sectional and three-dimensional view of the detector.

Figure 2.4: Cross-sectional view of the BABAR detector (dimensions are in mm).

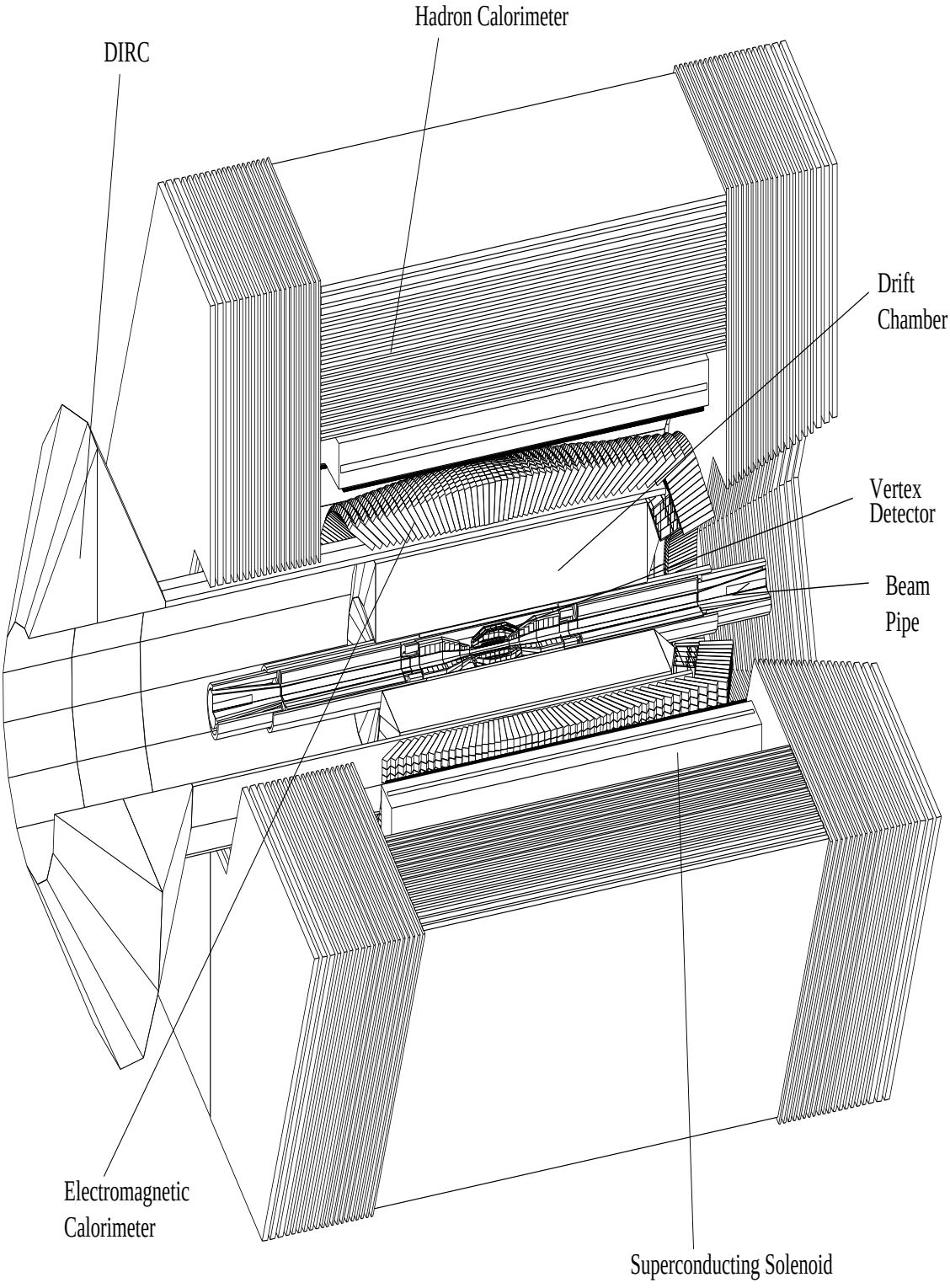

Figure 2.5: Three-dimensional view of the BABAR detector.

2.3.1 The silicon vertex detector

The design of the vertex detector is based on a double-sided microstrip detector. It is made up of five layers and is located between the beam pipe and the drift chamber. The detector has a total of 340 silicon detectors and 150,000 readout channels. The total area of the detector is 0.94 m^2 and covers a solid angle of $17.2^0 < \theta_{lab} < 150^0$ which is equivalent to $-0.95 < \cos\theta_{cm} < 0.87$. The main task of the detector is to reconstruct the decay vertices of the two B mesons. The mean separation ($\Delta z = Z_{CP} - Z_{tag}$) of the two B mesons is 250 μm. The target position resolution required for CP asymmetry measurements is $\delta(\Delta Z) = 50/p_t \oplus 15$ μm (addition in quadrature) and the target angular resolution is $\delta\theta = 1.6\ mrad/p_t$ (with p_t in GeV/c). This is well within the reach of the silicon detector. For particles with low transverse momenta (p_t <100 MeV/c), which may not be reconstructed in the drift chamber, the silicon detector may be used to provide tracking information and thus acts as a tracking device as well as a vertex detector. The main source of background in the vertex detector comes from bremsstrahlung and Coulomb scattering of beam particles from residual gas molecules in the beam pipe, the result of which produce high energy particles which create electromagnetic showers of electrons and photons. The ionization produced by these particles causes radiation damage and may eventually degrade the performance of the silicon sensors and the front-end electronics.

2.3.2 The drift chamber

The chamber is designed with low Z materials which includes a mixture of helium and butane gas and aluminium wires. It has been designed with the aim of minimising the amount of material in the chamber, thus permitting the best possible measurement of the relatively low momentum tracks necessary for CP asymmetry studies. It is 280 cm in length and occupies a radial space between 22.5 cm and 80 cm, just outside the vertex detector. It covers a polar angle of $-0.87 < \cos\theta_{lab} < 0.96$. The chamber is filled with a mixture of helium and butane gas in a ratio of 80:20, with a radiation length of about 800 m. The target momentum resolution is $\delta(p_t)/p_t = [0.21 + (0.14 \times p_t)]\%$. For low momentum particles, i.e. particles with momentum less than 1 GeV/c, the ionization loss (dE/dx) information provides a means of particle identification. Thus it can be used

for π/K separation up to momenta of 700 MeV/c. However most of the charged particles at PEP-II fall within this low momentum range. Apart from its function as a particle identification device, it forms part of the trigger system for BABAR. Another important use is for reconstruction of secondary vertices such as K^0 which will be missed by the vertex detector.

2.3.3 The DIRC

The DIRC (Detection of Internally Reflected Cherenkov light) meet an additional requirement for detection of particles of momenta greater than 0.7 GeV/c. It occupies the barrel region and covers a solid angle of $25.5^0 < \theta < 147^0$ It comprises of 156 quartz bars arranged in a 12-sided polygon around the beamline. Each quartz bar is 4.7 m long, 1.75 cm thick and 3.5 cm wide. Charged particles passing through the detector emit Cherenkov photons which are carried through internal reflection to a photon detector (photomultiplier tubes) located at the ends of the bar. The angle of emission of the detected Cherenkov photons is proportional to the velocity of the transversing charged particle. From this relation and information from the drift chamber of the particles momentum, the mass of the charged particle can be measured. The DIRC provides a π/K separation up to 4.3 GeV/c. The main source of background are: photons from synchrotron radiation, beam-gas interactions, radiative Bhabha, cosmic rays and phototube dark noise. These backgrounds might also affect the performance of the detector.

2.3.4 The electromagnetic calorimeter

A high sensitivity is required for measuring the CP violation asymmetries. This requires a high efficiency and good resolution for effective reconstruction and tagging of the two B^0 mesons. Achieving this high efficiency and good resolution implies a need for a calorimeter with an excellent photon energy resolution and efficiency at low energies (as low as 20 MeV) to give a good π^0 and B mass resolution. The ideal choice to meet this requirements is the CsI(TI) calorimeter. It is made up of 6780 CsI crystals doped with thallium iodide. The thallium iodide doping is for enhancing the light yield of the crystals. The calorimeter is located between the DIRC and the superconducting solenoid. It consists of two sections: the barrel and the forward endcap. The barrel

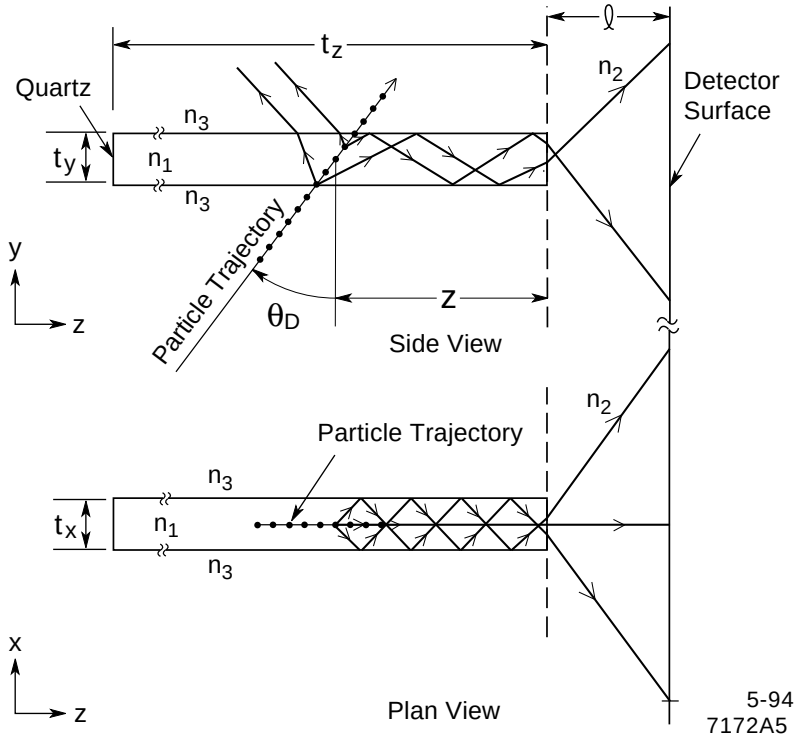

Figure 2.6: Schematic of a single radiator bar of a DIRC counter. The trajectory of the particle is shown by connected dotted lines and those of the photons are shown by lines with arrows.

section is cylindrical, comprises 5880 crystals, weighs 23.5 tonnes and covers a solid angle of $-0.8 \leq \cos\theta \leq 0.89$. It has a volume of 5.2 m^3. The forward endcap weighs 3.2 tonnes

Figure 2.7: Side view of the calorimeter, dimensions (in mm) showing the barrel and forward endcap.

with a solid angle coverage of $0.89 \leq \cos\theta \leq 0.97$. It has a total volume of 0.7 m^3. The crystals have trapezoid cross sections and tapered along their lengths. Each crystal is 4.8×4.7 cm at the front face and 6×6 cm at the back face. They vary in length in $0.5X_O$ steps from $17.5X_0$ in the forward part of the barrel to $16.0X_0$ in the backward part, with $17.5X_0$ in the forward endcap, where X_0 is the radiation length (1.86 cm). The readout system consist of silicon PIN photodiodes coupled to low-noise charge-sensitive preamplifiers. This could be attached either directly with optically conductive glue to the ends of the crystals or indirectly by means of wavelength shifters. The idea of the wavelength shifters is to shift the scintillation light emitted from the crystals to a more sensitive region of the photodiode. Results of tests using both techniques are presented in chapter 3. For reasons of simplicity the direct coupling solution was ultimately chosen. At a polar angle of 90^0 the target energy resolution for photons is [25]

$$\frac{\delta E}{E} = \frac{1\%}{\sqrt[4]{E(GeV)}} \oplus 1.2\%$$

Momentum	Events	Electron	π^+	π^-
	Generated	1000	5000	5000
0.5 GeV/c		926	3	7
1.0 GeV/c	Surviving	968	1	1
5.0 GeV/c		972	0	1

Table 2.3: Results of a GEANT study of e/π separation.

and the target angular resolution is [20]

$$\delta\theta = \frac{3}{\sqrt{E(GeV)}} \oplus 2\ mrad.$$

The calorimeter serves three main purposes: (1) a neutral trigger, (2) π^0 detection and (3) lepton identification (e/π and e/μ separation) for tagging purposes. A simulation of the full BABAR detector and the expected π^0 detection efficiency is discussed in chapter 4. Results of a GEANT study of e/π separation done for the BABAR Technical Design Report is shown in Table 2.3 [26]. The main source of background is the low-energy photons from showers of lost beam particles. Mean photon energies from these showers can be as low as 500 keV which is below the detection power of the calorimeter to be detected as extra photons. This degrades the energy resolution of the calorimeter and also causes radiation damage. Results from the testbeam of the prototype calorimeter is shown in chapter 3.

2.3.5 Superconducting solenoid

The superconducting solenoid provides a magnetic field of 1.5 T with a hexagonal flux return. It is energised with a constant current of 7110 A. The current density is graded in three regions connected in series. The central region is 1728 mm long with 240 turns and the each of the two end regions is 864 mm long with 240 turns. The current density in the end region is twice that of the central region.

2.3.6 Hadron calorimeter

The hadron calorimeter is made of large iron structure called the instrumented flux return (IFR). It consists of three main parts: the barrel, backward and forward endcap. The barrel extends radially from 1.78 to 3.01, m and is divided into sextants. The length of each sextant is 3.75 m and the width varies from 1.88 to 3.23, m. Each endcap consists of hexagonal plates divided vertically into two parts. The calorimeter provides an external flux path for the magnetic field of the superconducting solenoid and serves as a muon identification device and a neutral hadron detector. Muon identification is very important for B meson tagging. The main goal of the detector is to achieve the highest possible tagging efficiency. As a neutral hadron detector, it will allow the detection of K_L^0 and other neutrons which escape detection by the other detectors. This enables the study of CP-violation channels such as $B^0 \longrightarrow J/\Psi K_L^0$. A study of the detector done for the Technical Design Report, showed a 2% misidentification of pions as muons and a K_L^0 detection efficiency of 68% [26]. Background sources such as cosmic rays, lost beam particles, synchrotron radiation etc. are expected to be negligible due to shielding of the detector by the CsI calorimeter, magnet and return flux steel.

Chapter 3

Testbeam results of the BABAR prototype calorimeter

3.1 Introduction

The electromagnetic calorimeter has a very essential and crucial role to play in the BABAR experiment since most of the channels of interest for CP violation studies contain one or more π^0's which need to be detected and well reconstructed. In September 1995, a prototype calorimeter for BABAR was tested in the "πM1" beamline at the Paul Scherrer Institute (Zurich). The aim of the test was to obtain results needed for the design of the calorimeter, to make measurements to validate the Monte Carlo and to start the learning process of operating and calibrating a CsI calorimeter. The "πM1" secondary beam was derived from a primary proton beam with beam rate of 50 MHz or 20 ns between pulses with a pulse width of 1 ns, incident on a 7 mm thick graphite target (TM). The distance of the beam line from the TM target to the experimental area was 20.6 m. The beam was a mixture of electrons and pions with momentum range of 100 MeV/c to about 450 MeV/c. There was almost equal amounts of electrons and pions at 215 MeV, more electrons than pions at lower energies and more pions than electrons at higher energies. Two planes of multiwire proportional chambers were used to measure the position and direction of the beam particles and the timing was done with scintillators. Particle identification was done by using the time of flight. The 20.6 m flight path gives large time separation for electrons and pions. However with the 20 ns repetition rate of

the machine some momentum ranges are not usable, since the flight time difference is an integral multiple of 20 ns. Figure 3.1 shows the time difference between electrons and

Figure 3.1: Apparent difference in arrival time between pions and electrons at the experimental hall versus beam momentum (This figure was produced by P. Dauncey of the Rutherford Appleton Laboratories, UK and R. Seitz of Dresden University, Germany).

pions and which momentum ranges would be usable. Assuming a 2 ns resolution on the arrival of the beam particle, then the momentum ranges giving three sigma separation are:

- p < 105 MeV/c;
- 125 MeV/c < p < 150 MeV/c, optimum 135 MeV/c;
- 210 MeV/c < p < 325 MeV/c, optimum 250 MeV/c.

The prototype electromagnetic calorimeter used for the study was a 5 by 5 array of CsI crystals, as a small scale version of the final detector of 6580 crystals. The size of each crystal was 5 × 5 cm at the front face, 6 × 6 cm for the back and 36 cm long. Each crystal

was wrapped in 140 μm Tyvek, 25 μm of Aluminium and 160 μm of Teflon(PTFE) and placed inside a 250 μm thick kevlar box. The crystals were enclosed in a light-tight and radio frequency tight environmental box with a cooling system to keep the temperature within $1^0\,C$ of $18^0\,C$. The box was mounted on a turntable which could thus be rotated at several angles for data taking. Data was also taken for the staggered configuration of the crystals for studying the barrel section of the real BABAR calorimeter, and data for gaps and material between the crystals was taken for studying endcap barrel interface. The experimental setup is shown in fig. 3.2. The scintillation light emitted from the

Figure 3.2: The experimental configuration. A Monte Carlo simulation is shown of an electron passing through the first set of wire chambers, the small scintillator, the second wire chambers and the large scintillator, before showering in the crystal matrix.

crystals was sensed by two photodiodes (to compare the performance of the two) coupled to the back of each crystal. Thirteen of the crystals were coupled directly with two 20 $\times$ 10 mm^2 Hamamatsu S 2744-08 photodiodes, with a Silicon Nitride upper layer. The other twelve crystals were coupled to two photodiodes (S 3588-03 model 5400) of active area 30 $\times$ 3 mm^2 glued on the adjacent lateral faces to a 3 mm^2 thick wavelength shifter of surface area 5 $\times$ 5 cm^2. The purpose of the wavelength shifter was to shift the emitted light to a higher wavelength and thus increase the quantum efficiency. Signals from the two photodiodes were then amplified and shaped separately by P196 preamplifiers and a shaper attached to the photodiodes. The signals were then connected to a set of receiver

boards to an ADC-32 12 bit ADC which digitised the signals and then passed them on to a DAQ system (see fig. 3.3).

Event triggering was done at intervals of 20 μsec with an AND of the two beam scintillators. Calibration was done with both electron and pions. Each crystal was first calibrated with electrons at 215 MeV/c at normal incidence to the front face of the crystal. Each diode produced two outputs: low gain and high gain. The calibration constant for the high gain output was 80 keV per ADC channel and 2 MeV per ADC channel for the low gain. It was assumed that the number of ADC counts is linear with energy over the range energy range up to 325 MeV (80% of maximum beam energy). This assumption was valid due to linearity of light yield with energy and electronic gain. Calibration with pions was done with 9 central crystals and was based on a specified energy loss of pions [27]. The calibration constants from both methods were found to agree to within 0.5%.

Figure 3.3: General schematic of a crystal readout scheme.

Electronic noise was monitored using pedestal runs which were recorded at 3 minutes intervals alongside the data. A pedestal event was triggered with a 1 KHz internal clock outside the 20 μs data window. Fig. 3.4 shows noise measurements from pedestal events for both low and high gain channels (for direct readout and wavelength shifter). The mean

Figure 3.4: Single channel noise obtained from pedestal events for all low gain and high gain channels. The direct readout are shown as the hatched histograms [27].

noise measurement per photodiode for direct readout, the wavelength shifter (WLS) and for both combined is shown in Table 3.1. The mean noise for all high gain channels was measured to be 411 keV and 881 keV for all low gain channels. Full details of the

	Low Gain Channels Noise (keV)	High Gain Channels Noise keV
All	881	411
WLS	846	349
Direct	921	450

Table 3.1: Mean noise measured per photodiode for wavelength shifter (WLS) and direct readouts and for both combined [27].

experiment are described in Ref. [27]. Analyses of these data were carried out using both electrons and pions and a comparison was made with Monte Carlo predictions.

3.2 Response to electrons

The electron spectrum at 215 MeV is shown in fig. 3.5. This was obtained by taking the

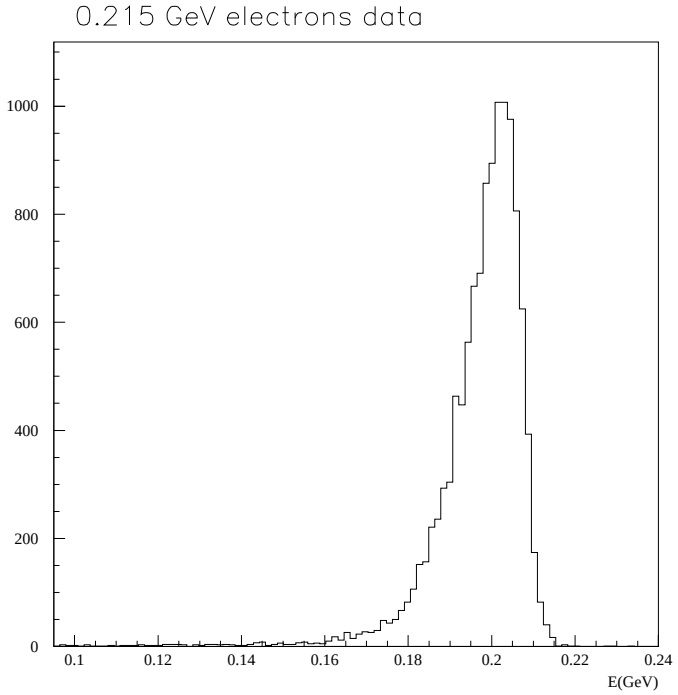

Figure 3.5: Measured energy for electrons at 215 MeV showing low energy tail.

energy deposited in the 25 crystals for each electron event. A threshold of 0.5 MeV was put on this energy, requiring that the energy deposited in each crystal for each electron event be more than 0.5 MeV. It can be seen that the response of the calorimeter to electrons has a relatively narrow, asymmetric peak, with a tail on the low energy side and which is due to the effect of bremsstrahlung. It is interesting to find a function that will fit this shape.

3.2.1 Fitting of the electron spectrum

Three different fit functions: (1) a Single Gaussian; (2) a Logarithmic Normal Distribution; (3) a Product of Landau and a Gaussian; were each fitted to the data at three energy points: 100, 215 and 405 MeV respectively. The energy resolution is defined as $\sigma_E = FWHM/2.36$, where FWHM is the full width at half maximum. The relative

energy resolution is

$$\frac{\sigma_E}{E} = \frac{FWHM}{2.36E_p}, \tag{3.1}$$

where E_p is the energy at the peak of the distribution. The resolution function described by a single Gaussian is

$$f(x) = Ne^{-0.5(\frac{x-\mu}{\delta})^2},$$

where μ is the mean of the distribution and δ is the standard deviation or error on the mean and N is the normalisation. The fit of a single Gaussian to the data at 215 MeV is shown in fig. 3.6. It can be seen from the figure that the tail at the lower edge of the data is the principal cause of the poor χ^2. The energy resolutions and the means (μ) obtained from the fits to the data at 100, 215 and 405 MeV respectively were:

Figure 3.6: Electron energy distribution at 215 MeV with a fitting to two different functions.

- $(4.46 \pm 0.02)\%$ $\mu = (93.55 \pm 0.36)$ MeV at 100 MeV;
- $(3.46 \pm 0.04)\%$ $\mu = (207.78 \pm 0.02)$ MeV at 215 MeV;
- $(2.50 \pm 0.15)\%$ $\mu = (400.25 \pm 0.38)$ MeV at 405 MeV.

The second function tested was the logarithmic normal distribution. The purpose was to fit the tail of the data. This function has three parameters a, b and c. It is given by

$$f(x) = \frac{a}{x_0 - x} e^{(-(\frac{\ln(x_0 - x) - b}{c})^2)}$$

The full width at half maximum is given by

$$FWHM = x_0 - e^{(b - 0.5c^2)} \frac{2\sinh(\sqrt{2}c)}{x_0 e^{0.5c^2 - b} - 1}$$

Comparing this function to a normal distribution, the variable x has been replaced by $\ln(x_0 - x)$ where x_0 is the endpoint of the distribution (a parameter for fitting the tail), b is the mean (μ) and c is the error on the mean. The fit result at 215 MeV is shown in fig. 3.6. The energy resolutions from the fits were:

- $(4.04 \pm 0.02)\%$ $\mu = (91.25 \pm 0.67)$ MeV at 100 MeV;
- $(3.19 \pm 0.03)\%$ $\mu = (208.19 \pm 0.53)$ MeV at 215 MeV;
- $(2.71 \pm 0.03)\%$ $\mu = (400.02 \pm 0.25)$ MeV at 405 MeV.

The third function tested was a product of Landau and a Gaussian. This is a product of a Landau distribution with a tail on the left multiplied by a Gaussian to damp the Landau. The function is given by

$$f(x) = N \times denlan(\frac{\mu_1 - x}{\delta_1}) e^{-0.5(\frac{\mu_2 - x}{\delta_2})^2}.$$

It has five parameters. μ_1, δ_1 are the mean and mean error of the distribution. μ_2, δ_2 are the mean and width of the additional Gaussian and N is the normalisation. The denlan function can be found in the CERN program library manual and is given by

$$\phi(\lambda) = \frac{1}{2\pi i} \int_{c-i\infty}^{c+i\infty} e^{(\lambda s + s \ln s)} ds, \tag{3.2}$$

where c is real. The results of the fit to the data at energies 100, 215 and 405 MeV respectively is shown in fig. 3.7. The energy resolutions obtained from the fits were

- $(3.01 \pm 0.20)\%$ $\mu = (90.55 \pm 0.42)$ MeV at 100 MeV;
- $(2.40 \pm 0.21)\%$ $\mu = (210.02 \pm 0.73)$ MeV at 215 MeV;
- $(1.95 \pm 0.20)\%$ $\mu = (400.86 \pm 0.34)$ MeV at 405 MeV;

Figure 3.7: Electron energy distributions at three energy points: 100, 215 and 405 MeV with a fitting to a product of landau and a Gaussian function.

Function	100 MeV	215 MeV	405 MeV
Single Gaussian	24.48	9.87	5.58
Log Normal distribution	12.12	7.65	3.21
Product of Landau and a Gaussian	5.57	5.70	2.46

Table 3.2: Chi-squared per degree of freedom for the different fit functions at each energy point.

The χ^2 per degree of freedom was much better than any of the 2 other functions (see Table 3.2). The product of Landau and a Gaussian thus proved to be the best of the three functions and hence was used for fitting the electron spectrum.

3.2.2 Energy resolution vs energy

With the product of Landau and a Gaussian a study was made of:

- the energy resolution vs energy;
- the effects on this of materials between and in front of the crystals;
- the beam hitting the crystal face at an angle;
- summing the energy deposited over nine crystals instead of twenty five.

The energy resolutions vs energy was determined using Monte-Carlo simulations and data at the five energy points 100, 135, 215, 320 and 405 MeV. The energy resolution is shown as a function of energy in fig. 3.8. The fitting to the data and the Monte Carlo is parameterised by

$$\frac{\delta E}{E(GeV)} = \frac{a}{\sqrt[4]{E(GeV)}} \oplus \frac{b}{E(GeV)} \oplus c,$$

where the term a is the empirically observed low energy behaviour, b is electronic noise contribution and c is a constant term due to shower leakage fluctuations, inter-calibration errors and non-uniformities in the crystal response. The target energy resolution laid down in the TDR is

$$\frac{\delta E}{E(GEV)} = \frac{1\%}{\sqrt[4]{E(GeV)}} \oplus 1.2\%.$$

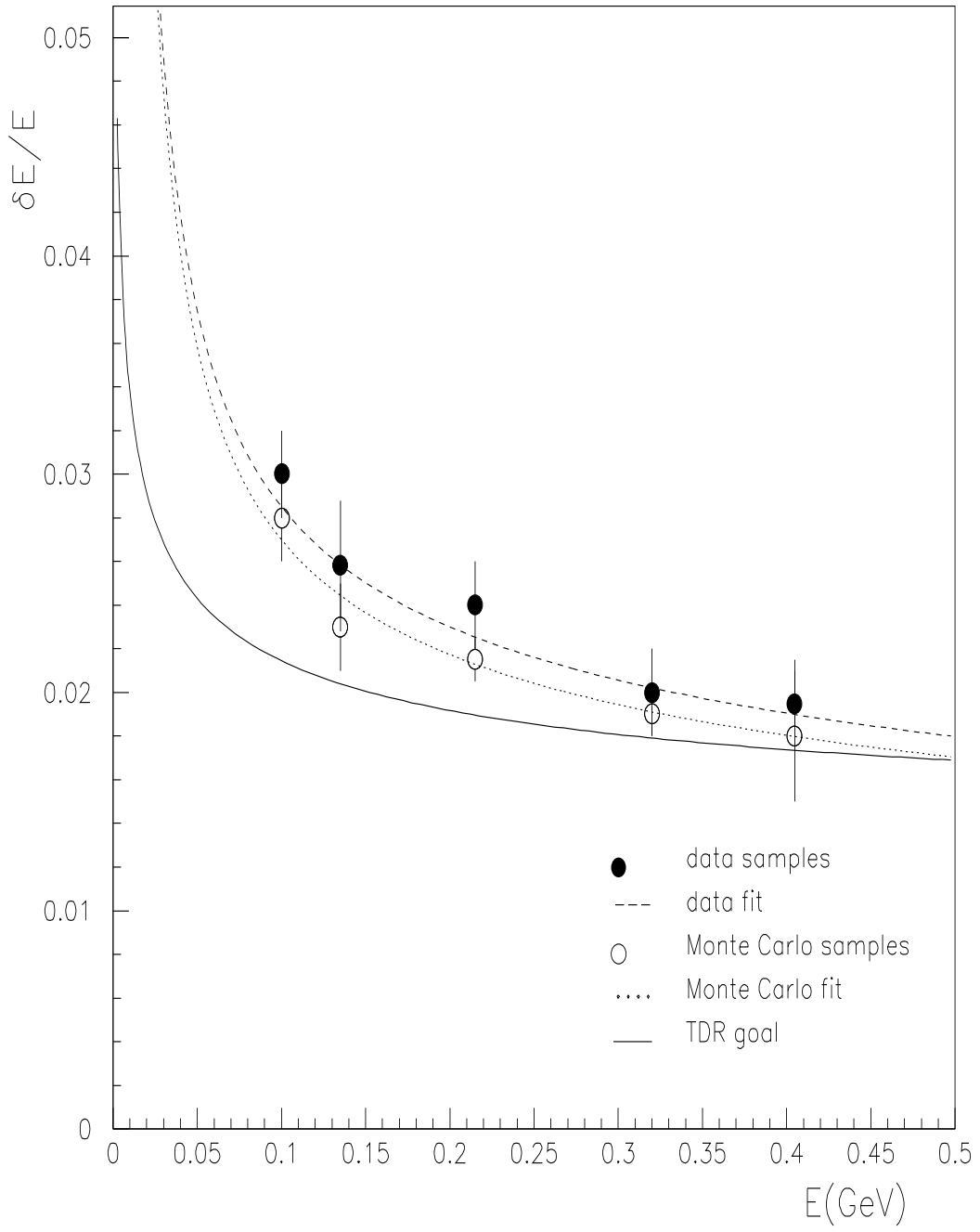

Figure 3.8: Energy resolution vs energy for Monte Carlo and data. Also shown are the TDR goal without electronic noise.

This excludes electronic noise contribution which was assumed to be negligible for typical clusters of 16 to 25 crystals.

The Monte Carlo are fitted by:

$$\frac{\delta E}{E(GeV)} = \frac{(1.41 \pm 0.09)\%}{\sqrt[4]{E(GeV)}} \oplus \frac{(1.61 \pm 0.11) \times 10^{-3}}{E(GeV)} \oplus (0.3 \pm 0.02)\%$$

The real data is fitted by:

$$\frac{\delta E}{E(GeV)} = \frac{(1.50 \pm 0.10)\%}{\sqrt[4]{E(GeV)}} \oplus \frac{(1.59 \pm 0.10) \times 10^{-3}}{E(GeV)} \oplus (0.10 \pm 0.01)\%$$

From fig. 3.8 we could see that the Monte Carlo and data agree reasonably well but showed a significant deviation from the BABAR Technical Design Report proposal. The reason for this difference is that the TDR resolution is without electronic noise. All three however agree with 1/fourth root of energy dependence. Fig. 3.9 shows plots of energy resolution vs energy with 9 crystals compared with 25 crystals, with the beam hitting the crack of the centre crystal. The solid curve is the fitted function to the data for the 25 crystals and the dotted curve is for the 9 crystals. The resolution from the 9 crystals was worse than for the 25 crystals. This is attributed to side leakage, the fluctuations in energy lost beyond the sides of the 9 crystals array is more than for the 25 crystal array. The resolution for the 9 crystals is given by

$$\frac{\delta E}{E(GeV)} = \frac{(2.1 \pm 0.10)\%}{\sqrt[4]{E(GeV)}} \oplus \frac{(1.98 \pm 0.13) \times 10^{-3}}{E(GeV)} \oplus (0.70 \pm 0.05)\%$$

and for the 25 crystals

$$\frac{\delta E}{E(GeV)} = \frac{(1.50 \pm 0.10)\%}{\sqrt[4]{E(GeV)}} \oplus \frac{(1.59 \pm 0.10) \times 10^{-3}}{E(GeV)} \oplus (0.10 \pm 0.01)\%.$$

In Table 3.3 results of energy resolution vs energy with no material in front of the crystal stack, and the effects on the resolution when materials are put in front and in between the crystals are shown. In run 1, no materials were put in front of crystals. This was the normal set-up. For run 2, columns 1 and 2 of the crystal stack were moved 5mm to the left, leaving an air gap. Run 3 gives the resolution for 2 mm of aluminium plus 4 mm air "sandwich" put 11mm away from the front of the crystal stack. For run 4, 5 mm of aluminium plate was put 12 mm in front of the crystal stack. For run 5, the air gap in stack 1 was filled with 1 mm of carbon fibre. For run 6, the air gap was filled with 1 mm

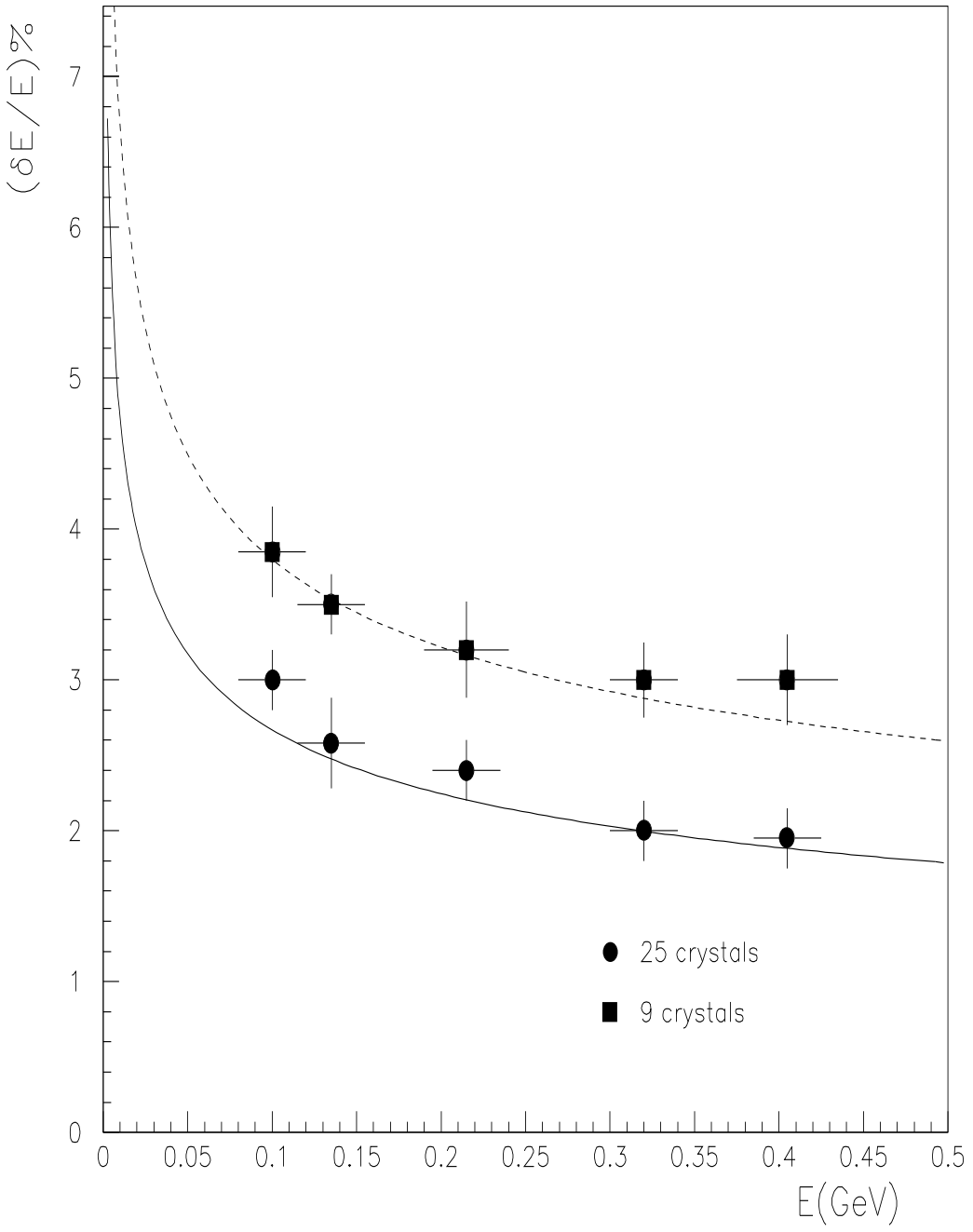

Figure 3.9: Energy resolution vs energy for data - solid curve 25 crystals, dotted curve 9 crystals.

Run	Configuration	$(\delta E/E(GeV))\%$
1	No material in front of stack	2.40
2	5mm Air gap between crystal columns 1&2	2.40
3	2mm Al + 4mm Air, 11mm in front	2.41
4	5mm Al, 12mm in front	2.57
5	Air gap in 2 filled with 1mm of carbon fibre	2.98
6	Air gap in 2 filled with 1mm sheet of Aluminium	3.62

Table 3.3: Energy resolutions obtained at 215 MeV for different crystal configurations.

Energy(MeV)	0 mrad	14 mrad	56 mrad
135	2.58%	-	2.71%
215	2.40%	2.58%	2.58%
405	1.95%	2.01%	2.44%

Table 3.4: Energy resolution vs energy for different beam angles at three energy point

sheet of aluminium. It can be seen from the table that the energy resolutions obtained for runs 5 and 6 were worse, with run 6 being the worst of all. The purpose of placing materials in between the crystals stack as in runs 5 and 6 was to study the effects on the resolution due to the endcap/barrel interface in the real BABAR electromagnetic calorimeter. Table 3.4 shows the energy resolution vs energy for different beam angles to the face of the crystal stack This study was done at 3 energies, 135, 215 and 405 MeV, and three beam angles, 0, 14 and 56 mrad. The 0 mrad was the normal incidence and was the situation where the beam hits the crack of the central crystal whilst 14 mrad is the situation where the beam hits the centre of the central crystal in the 5 by 5 array. The reason for choosing these angles for the studies was due to the fact that one of the chief aims of the beamtest was to study projective versus non-projective cracks in θ for BABAR. Given the fact that the crystal taper is 14 mrad, 0 and 56 mrad are truly projective. There is a suggestion of a slight decrease in resolution as the angle increases.

3.3 Response to pions

3.3.1 Introduction

GEANT Monte Carlo has two codes available: GHEISHA and FLUKA, which are used to simulate hadronic interactions. GHEISHA (Gamma-Hadron-Electron-Interaction SH(A)ower code) is a general code to handle interactions, showers and tracking of all particles within the materials setup and defined by the user. The GHEISHA code generates hadronic interaction with the nuclei of the current tracking medium, evaluating cross-sections and sampling final state multiplicity and kinematics. The elastic and inelastic cross-sections are parameterised using data from interactions of pions, Kaons and protons on free protons. The parameterisation is based on the QCD parton model and describes the cross-sections on free protons in terms of quark scattering amplitudes which are determined from a fit to the cross-section data on the free protons [28].

FLUKA (Fluctuating KAskade) is a stand alone program which simulates showers from high energy particles ($\sim$ TeV) to energies as low as 20 MeV. It uses many models for different energy regions. One example is the "pre-equilibrium and evaporation model" which is applied to energies below 300 MeV. This model involves two stages: the pre-equilibrium stage and the evaporation stage. The pre-equilibrium stage involves the intranuclear cascade (INC) algorithm and the exciton model [29, 30]. At this stage non-stopping hadrons (those with energy above the cut-off energy) are made to interact elastic or inelastically with the nucleus. The secondary nucleons from the pion interactions are converted to "excitons" [29] if their energy is below the energy threshold, otherwise they are passed on for further tracking. In the exciton model, independent-particle-model states are classified according to the number of particles and holes ("excitons") excited from the even-even ground state. A full description of this model is given in Refs. [29, 30]. The evaporation stage follows at the end of the exciton chain. At this stage the residual nucleus is a thermal equilibrated system with a certain amount of excitation energy that can be spent in particle evaporation.

At the start of an event, the hadronic packages, GHEISHA or FLUKA is called. This generates the hadronic interaction and calculates the hadronic cross sections and the distance for the next hadronic interaction. Tracking of the particle is done throughout

the particles trajectory. Tracking is done in defined step sizes. For a particle of a given energy the step size depends on the intrinsic properties of the particle (mass, charge, lifetime, etc.), and on the characteristics of the medium. After the elastic or inelastic interaction, if there are new particles and their energy is below the energy threshold, they are not stored but only their kinetic energy is stored. A routine is called which leads to nuclear absorption of negative pions, Kaons and neutrons. However if the particle can decay (eg. π^+, $K^\pm$), it is forced to decay [31]. If the energy of the particle is greater than the cut-off energy, they are passed on for further tracking. For each step size, the trajectory and total energy loss of the particle is stored. This is repeated for each volume the particle enters

It has been suggested for sometime that FLUKA provides better agreement with low energy pion energy deposition spectra than does GHEISHA. To allow this effect to be studied some low energy positive beam data was taken at PSI in addition to the negative beam data used in the other studies. The momentum range was 100 MeV/c to about 450 MeV/c. The pion events were selected from the data by the time of flight and making cuts on pion probabilities of 5%. 100k π^- and π^+ events at momentum points 215 and 405 MeV/c were simulated with FLUKA and GHEISHA and compared with the data.

3.3.2 Results

A simulated event is shown in fig. 3.10. The deposited energy spectra for pions of the indicated polarity and momentum are shown in fig. 3.11 along with predictions from the FLUKA and GHEISHA Monte Carlos. At 215 MeV/c FLUKA fits the data better at the upper shoulder of the peak whilst GHEISHA does better at the lower shoulder. For 405 GeV/c negative pions both programs do equally badly away from the peak, although the deviations are different. A clear distinction is shown in the 405 GeV/c positive pion data where FLUKA shows better agreement than GHEISHA. The lower energy tail of the data is due to interaction of pions with nuclei in flight. This part of the data is not well simulated by FLUKA due to the fact that the inelastic cross-sections for negative pions calculated in FLUKA is lower than their actual values. Although neither of the two programs matches the data perfectly, possibly as a result of a poor approximation

of the cross sections for nuclear interactions for low energy hadrons in both programs, what is clear is that FLUKA does indeed provide, overall a more adequate description of the data than GHEISHA. A previous report from BELLE showed that there were significant differences in the results of the FLUKA and GHEISHA simulations and the GEANT/FLUKA Monte Carlo simulations agrees better with the experimental data than using GEANT/GHEISHA.

Based on the results presented here, the cross sections for hadronic interactions has been modified in a new version of GEANT.

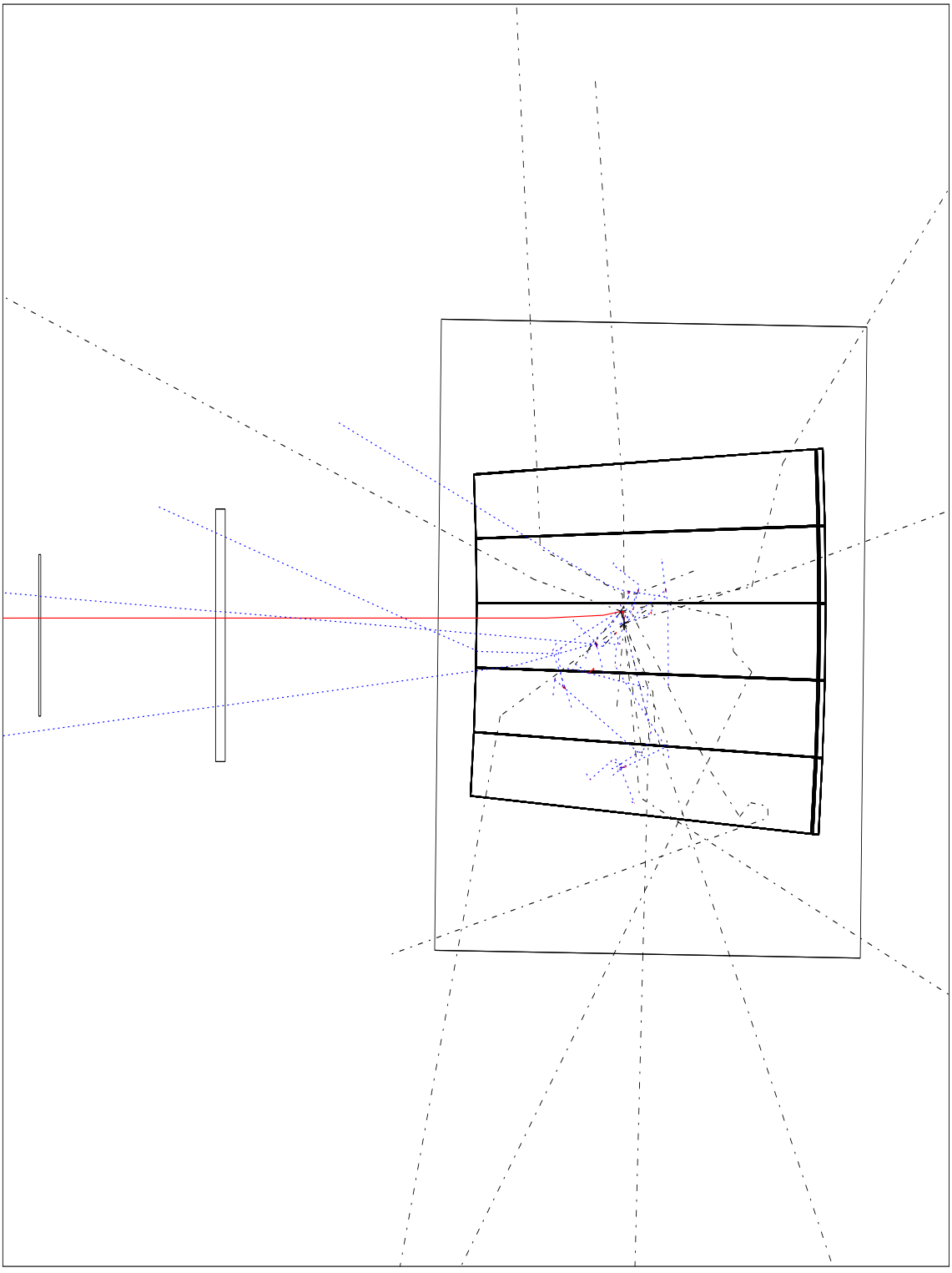

Figure 3.10: Simulation of a π^- event at 215 MeV.

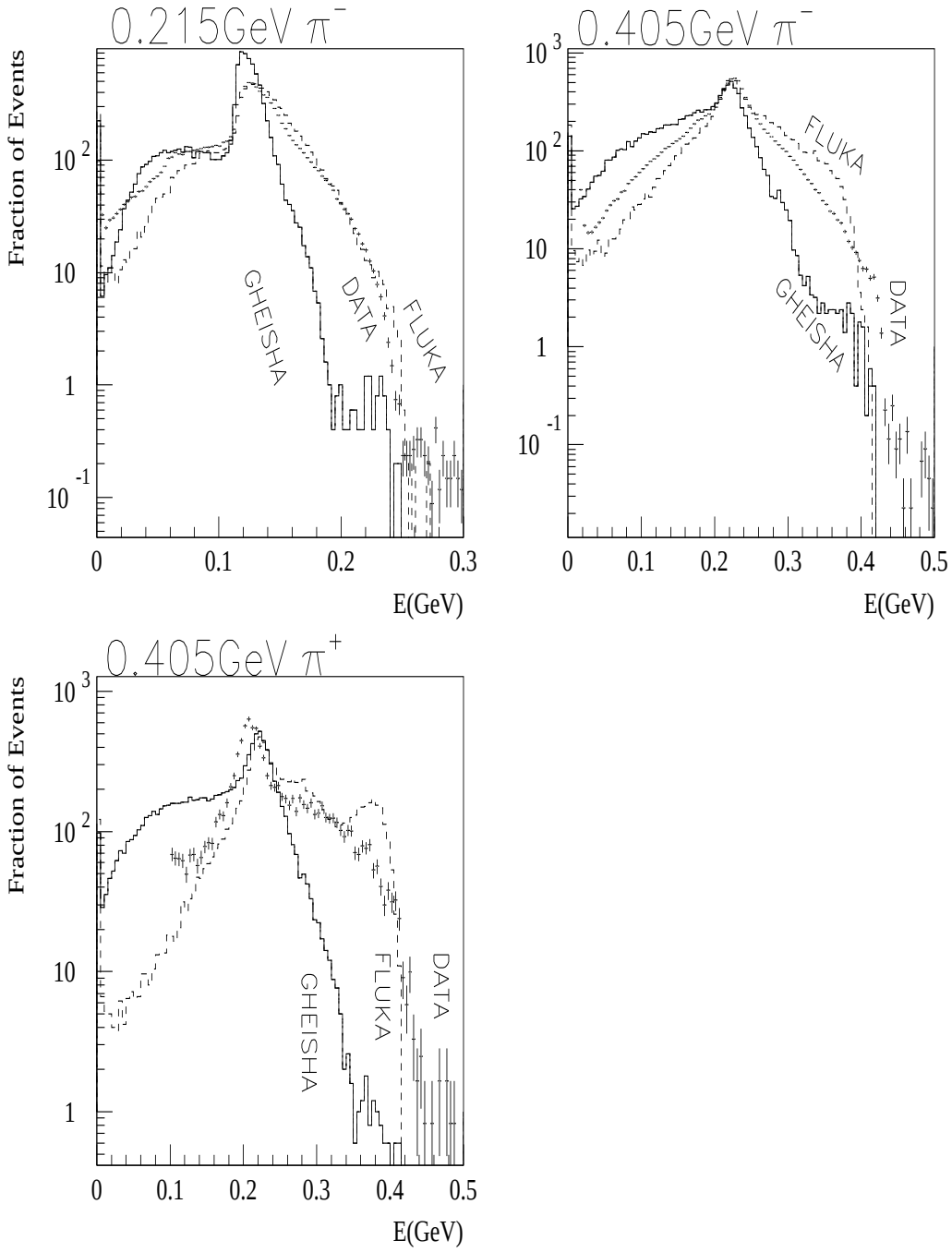

Figure 3.11: The energy deposited in CsI(Tl) by pions

Chapter 4

The sensitivity of the BABAR detector to CP violation studies

4.1 Introduction

In chapter 1 the use of isospin symmetry to extract $\sin 2\alpha$ from penguin contamination was demonstrated. This requires measurement of the time dependent rates of B decays to $\pi^0\pi^0$, $\pi^+\pi^0$ and $\pi^+\pi^-$ as well as their conjugate decays and which requires tagging to identify the B and $\overline{B}$ with the exception of the charged B decay which is self-tagged (the charge of the B is identified by the charge of the pion from the decay).

Since a precise measurement of the vertex for $B \longrightarrow \pi^0\pi^0$ and $\overline{B} \longrightarrow \pi^0\pi^0$ is not possible, only integrated rates can be obtained. Extraction of these decay rates will not be simple. There are two complications which conspire to make this task a difficult one: the anticipated low branching fractions due to colour suppression of the tree diagram of the decay process, and the experimental problems in reconstructing the required final state. Current theoretical predictions place the branching in the order of 10^{-7}. CLEO measurements give an upper limit as 9×10^{-6} [32]. This small branching fraction has two implications. Firstly the low event rate will lead to significant statistical errors. It also makes the channel particularly susceptible to continuum contamination. In addition to these there are also difficulties in the reconstruction of the B meson from an all neutral final state since the only available information is from the electromagnetic calorimeter (EMC) clusters.

$B \longrightarrow \pi^+\pi^0$ and $\overline{B} \longrightarrow \pi^-\pi^0$ involve only tree diagrams. If a negligible electroweak penguin contribution is assumed, then the rates of B and $\overline{B}$ are the same and only one decay rate measurement is needed. CLEO measurements of the upper limit of the branching ratio is 2×10^{-5} [32]. This channel relies on a good particle identification for Kaon and pion separation.

B decays to $\pi^+\pi^-$ allow one to measure the mixing parameter $\sin 2\alpha$. Measurement of this also requires a good π/K separation and good vertex resolution to measure time difference between the B and $\overline{B}$ decays. CLEO's upper limit for the branching ratio is 1.5×10^{-5} [32].

In all three studies a maximum likelihood fitting procedure has been developed in preference to event counting to achieve effective separation between signal and background. The ability of the BABAR detector to make measurements of these rates and the sensitivity on $\sin 2\alpha$ due to penguin contributions is demonstrated. In general $B\overline{B}$ events give negligible background in the $B \longrightarrow \pi\pi$ mode thus the dominant background source is from continuum $q\overline{q}$ events. A description of the Monte Carlo simulation is given below.

4.2 Monte Carlo simulation

The analysis to be discussed is based on Aslund (Asymmetric LUND). This is a BABAR fast parameterised Monte Carlo simulation package. Events are generated with JETSET 7.3 [33]. Once an event is generated, i.e. $\Upsilon(4S)$ decaying to a pair of B mesons, a routine called "asmxcp" mimics the effect of mixing (if there is no CP eigenstate) or CP violation (if one of the B mesons decays to a CP eigenstate) by charge conjugating one or both of the B mesons and all of the daughters with a probability that depends on the decay times. A particle table is then created and detector simulation follows. The detector response to charged particles is simulated by a subroutine called "trksim" and the response to neutrals is simulated by the subroutine "neusim". The beam pipe, vertex detector and the drift chamber form the tracking system. The drift chamber, the electromagnetic calorimeter and the DIRC form the particle identification system. A description and resolution parameters of the detectors are set in a data file by the user which are read

by the two subroutines. Track identification probabilities from each possible particle identification system are calculated based on these error parameters. There are two ways of operation in "trksim": (a) uses a routine called "trackerr" to develop a simple diagonal parameterisation of error matrix of each track based on estimates of the errors from parameters previously generated, and the track acceptance is determined by simple geometrical cuts, and (b) uses "trackerr" to generate a complete error matrix for each track, and determine acceptance by counting hits on the track [34]. Mode (a) is a faster process and is appropriate in situations where large number of events is needed but a detailed understanding of the resolutions is not essential e.g. combinatorial backgrounds. Mode (b) is much slower and appropriate for studies of specific channels where a detailed knowledge of the resolution is required. The subroutine "neusim" uses the information provided by "trackerr" on the electromagnetic calorimeter to smear the energies of the neutral tracks and calculate the four vectors of the tracks from information of track positions in the calorimeter. Photon resolution is based on parameterised histograms obtained from a full GEANT simulation of the BABAR detector (BBSIM). In GEANT, the hadronic package FLUKA, is chosen. Photons with ranges of energy and angles are generated with a flat distribution in energy and isotropic in direction in the centre of mass system and passed through the detector. Showers were then reconstructed from the hits in the EM calorimeter using a clustering algorithm method. For each photon generated the energy resolution is given by $x_E = (E_{rec} - E_{gen})/E_{gen}$ and angular resolution is given by $\Delta\theta = (\theta_{rec} - \theta_{gen})$, where E_{rec} is the reconstructed energy and E_{gen} is the generated energy and similarly for the angle θ. Histograms of the distributions of x_E and Δ_θ are then made for various bins of energy and $\cos\theta_{lab}$. The histograms are read into Aslund and for each photon generated and entering the electromagnetic calorimeter, generates a random variable distributed according to the shape of the histogram corresponding to energy and angular range the photon belongs and calculates the reconstructed energy. A full description of this method is given in reference [35]. The version of Aslund used for this analysis had certain known problems which are:

- Charged tracks due to neutrals that decay beyond the first tracking layer are not handled properly by "trackerr". The position of the decay is not accounted for, so all tracks are treated as if they come from the origin. This has an effect of worsening

the mass resolution of the reconstructed B meson;

- It gives a rough estimate of the true signal resolution for the following reasons: (a) no correct modelling of electromagnetic showers i.e. no split offs are included; (b) assumes 100% track matching efficiency; and (c) due to the substantial boost on the π^0 from the B decays, the opening angle of its decay to two photons is small, hence an overlap of clusters will be formed in the calorimeter which reduces photon efficiency. This is not accounted for in Aslund.

The best determination of signal resolution can be obtained from full reconstruction.

4.2.1 Obtaining the event sample

For the study presented here, the expected number of $B \longrightarrow \pi\pi$ events for a year at design luminosity, which equals $3.6 \times 10^7 \times R$, where R is an assumed branching fraction, is generated. For each decay mode, 8.1×10^6 $q\overline{q}$ continuum events is expected. Generating this huge continuum events will take a lot of CPU time. In order to reduce the time and burden on the CPU, cuts were applied at the generator level with the intention of rejecting a significant fraction of the continuum events before the detector simulation is made. The cuts have been kept loose in order to avoid the introduction of bias into the final event sample. The generator cuts applied for the continuum sample corresponding to each decay mode and the rejection factor obtained are given in Table 4.1.

4.3 Tagging

For $\pi^+\pi^-$ and $\pi^0\pi^0$ decay modes, separate measurements of the B^0 and $\overline{B}^0$ rates is needed and these require tagging. The idea of tagging is to identify the flavour of the B mesons. Thus events are studied where one of the B mesons from the coherent $B^0\overline{B}^0$ state decays to the CP violation mode being investigated, and the other B meson decays to a tag mode. The decay products of the tag mode is then used to identify the flavour of its parent B meson. By knowing the flavour of the tag mode, the flavour of the CP mode can be easily deduced.

In this study a standard BABAR tagging package called CORNELIUS (the combined optimal reconstruction with neural network and likelihood for identification usage) has

Decay Mode	Cut	Rejection Factor
$\pi^0\pi^0$	$4.0 < M_B < 6.5\,GeV/c^2$ $1.5 < p_B^{lab} < 6.0\,GeV/c$	0.95
$\pi^+\pi^0$	$4.0 < M_B < 6.5\,GeV/c^2$ $1.5 < p_B^{lab} < 6.0\,GeV/c$	0.97
$\pi^0\pi^0$	$4.0 < M_B < 6.1\,GeV/c^2$ $1.5 < p_B^{lab} < 6.0\,GeV/c$	0.98

Table 4.1: A table of cuts applied to continuum events at generator level and the rejection factor obtained for the three decay modes. M_B is the invariant mass of the B meson and p_B^{lab} is its momentum in the $\Upsilon(4S)$ rest frame.

been used. CORNELIUS [36] uses a set of event related discriminating variables to evaluate the probabilities of an event to come from a B^0 or a $\overline{B}^0$ meson. It uses four different techniques to evaluates these probabilities but there are no significant differences in the outputs of these four. One of these techniques which has been used here is the parameterised technique. This is a statistical method where the probabilities are evaluated using a likelihood analysis. With this method the correlations among the variables are accounted for but not fully exploited [37]. For any given event the output from this which is the tag value and which gives the probability of the event to come from a B or $\overline{B}$ take values between -1 and 1. A negative tag value implies the tag particle was from a $\overline{B}$ and a positive tag value implies from a B. It is worth mentioning that version V00-01-03 of CORNELIUS used here assumes perfect particle identification, hence a degradation of mis-tag probability should be expected in the more realistic situation.

4.4 Methods for separating the signal from the background

There are two methods which can be adopted to separate the signal component of the data from the continuum: (a) an event counting method and (b) a fitting method. In the event counting method, a series of cuts are made to the data and optimised to obtain

the best possible signal to background ratio. The aim is to keep the level of background contamination to the minimum. This method however can lead to significant reduction in signal efficiency and hence worsens the statistical error, making it unsuitable for channels with low branching ratios. Also systematics errors from background contamination are incurred since it is almost impossible to obtain a pure event sample. In the fitting method the aim is to use all available information from the data to make the best possible measurements of the signal and background components. This is achieved by making fits to the data using a maximum likelihood method. The advantages of this approach over the previous is that the background contamination does not have to be estimated from the Monte Carlo thereby eliminating systematic uncertainties. Also a better signal efficiency is achieved.

4.4.1 The maximum likelihood method

In the maximum likelihood method a likelihood function L, which is a measurement of the quality of a given hypothesis is defined in general as [38]

$$L = \prod_i f(x_i, \alpha) \tag{4.1}$$

where $f(x_i; \alpha)$ is a probability density function (p.d.f) for each independent measurement of a set of quantities x_i and α are the unknown parameters to be determined. The motive is to optimise these parameters to obtain the maximum value of L. In most situations it is convenient to consider the logarithm of the likelihood function i.e.

$$\begin{aligned} \mathcal{L} &= lnL \\ &= \sum_{i=1}^{n} \ln f(x_i, \alpha). \end{aligned} \tag{4.2}$$

For the studies presented here $\mathcal{L}$ is defined as

$$\mathcal{L} = \sum_n - \ln \frac{f(x_i, \alpha)}{\int f(x_i, \alpha) d(x_i)}, \tag{4.3}$$

where n is the number of events and the p.d.f is a sum of the p.d.f's of the signal and background components of the data as defined in the sections that follow. The denominator is the normalisation. The minimisation of $\mathcal{L}$ is done with the function minimisation and error analysis package (MINUIT) [39].

4.5 Event selection

To obtain the most effective signal measurement and a better determination of the background components of the data (the combined sample of signal and background distributions) from the fit described above, it is essential that events which fall in regions far from the signal region and which can degrade the quality of the fit due to statistical fluctuations in these regions have to be removed. This is achieved by making cuts against a set of discriminating variables. For those discriminating variables that will be used in the fit, the cuts are made at sideband regions around the signal just enough for the fit to trace the line shape of the background.

4.6 Fitting strategy

In a low statistics environment as expected in the very early life of the experiment and as considered here, in order to avoid having poor convergence of the fit, it is necessary that the number of parameters in the fit are kept to the minimum. This will require developing a strategy to fix some of these parameters. The strategy is to fix the signal line shape according to the Monte Carlo which however is at the expense of introducing more systematic errors. However in a low statistics environment the statistical errors dominate over the systematic errors. As more statistics becomes available as the experiment proceeds, it will then be possible to determine all the parameters directly from the fit without the need for the Monte Carlo. For the continuum there will be no statistical limitation and hence the line shape can be determined directly from the data at any stage in the experiment. A way of achieving this will be shown in the sections that follow.

4.7 $B^0 \longrightarrow \pi^0\pi^0$

From figure 4.1 there are significant differences in signal and background distributions and hence the discriminating variables selected are:

- M_π = the invariant mass of the π^0
- M_B = the invariant mass of the B^0

Cut	% of events passed	% of events passed with a correct solution	No. of combinatorial solutions per event
No Cuts	98	77	808
$0.11 < M_\pi < 0.155$ (GeV/c^2)	90	57	20.60
$4.65 < M_B < 5.55$ (GeV/c)	56	55	1.09
$0.15 < p^* < 0.40$ (GeV/c)	49	48	1.05
$-0.85 < \cos\theta^* < 0.85$	43	42.8	1.04
$\|tag\| > 0.05$	39.8	39.2	1.04
No. Solutions = 1	39.8	37.0	1.00

Table 4.2: Signal efficiencies for the applied cuts. The quoted efficiencies are cumulative.

- p^* = the momentum of the B^0 in the $\Upsilon(4S)$ rest frame.
- $\cos\theta^*$ = Cosine of the B sphericity angle in the $\Upsilon(4S)$ rest frame.
- tag = the tag value.

M_π, M_B and p^* are discriminating quantities which depend on the kinematics of the event whilst $\cos\theta^*$ is an "event shape" based quantity. For B decays to $\pi^0\pi^0$, $\pi^+\pi^0$ or $\pi^+\pi^-$, the two B mesons decay in independent directions, leading to a flat distribution in $\cos\theta^*$ whilst for the background the events are jet-like with a $\cos\theta^*$ distribution peaked at -1 and 1. Cuts are made against these variables with an additional cut requiring that only one combinatorial solution in a given event passes. Events are rejected if more than one solution is found. This cut helps to reduce the background from misconstructed events, without significantly affecting signal efficiency. In figure 4.1 projections of the event distributions are shown. Plots are shown for true signal events, their associated combinatorial background and for continuum events. Table 4.2 shows the cuts applied in selecting the events and the efficiencies obtained. The background efficiency obtained after all cuts is $(9.0 \pm 0.3) \times 10^{-6}$. Projections for the selected events are shown in

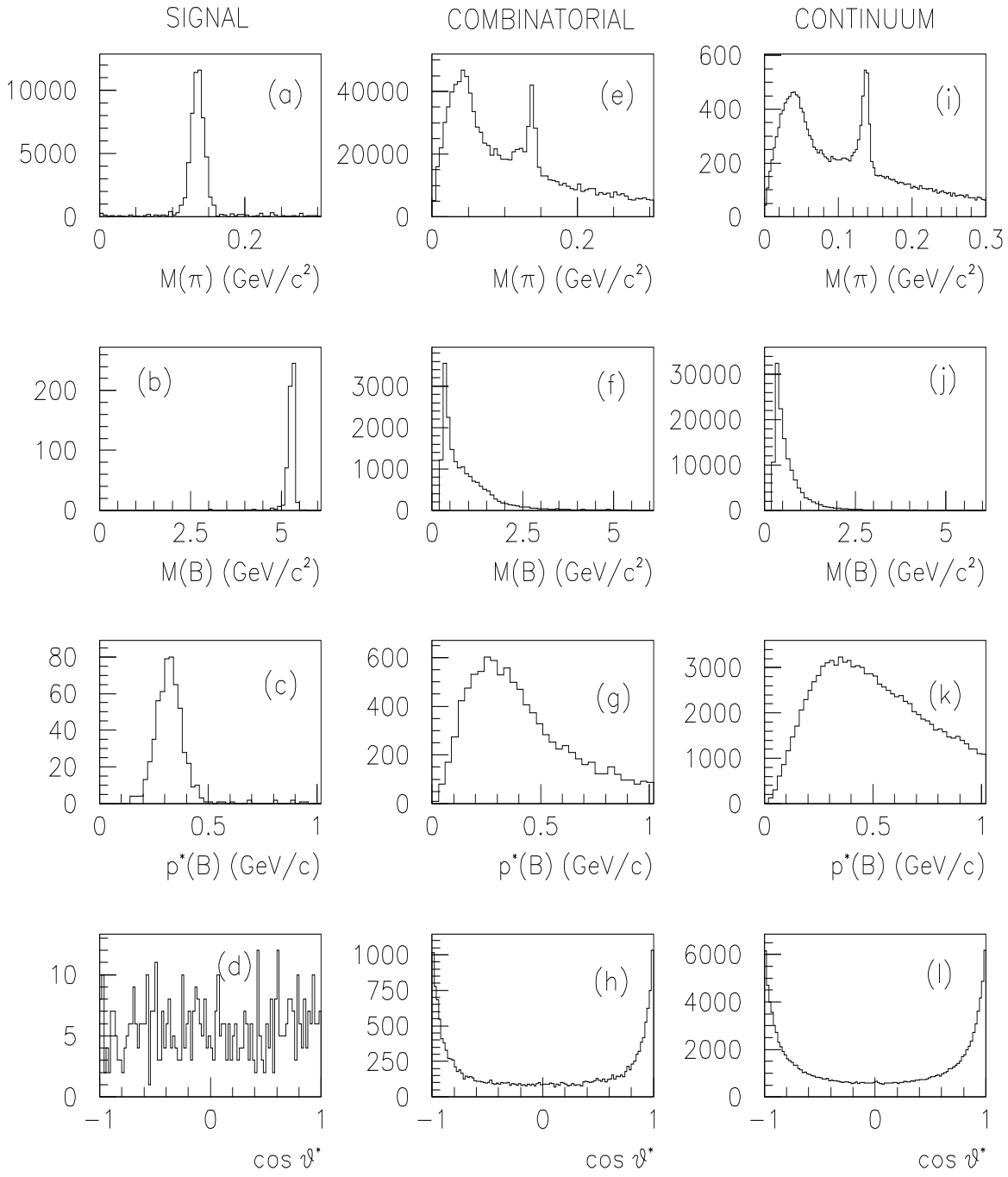

Figure 4.1: Projections of the event distributions for (a-d) correctly constructed signal, (e-h) combinatorial background, and (i-l) continuum background. No cuts are applied for the π^0 mass plots. For all other plots it is required that $0.11 < M_\pi < 0.155\,GeV/c^2$. No further cuts have been applied. The plots are shown with arbitrary normalisation.

figure 4.2. Distributions for the tag are shown for the selected signal and continuum events in figure 4.3. After event selection, fits are then made to the data to separate the signal and background and extract the parameters required. The discriminating variables selected in constructing the fit function are M_B, $\cos\theta^*$ and the tag value which were found to have no correlations with each other. The discriminating variable M_{π^0} is neglected since it was found that out of the π^0 candidates selected from the continuum 89% are true π^0's, and p^* is neglected due to possible correlations with M_B. The p.d.f function $f(M_B, \cos\theta^*, tag)$ is the sum of the B, $\overline{B}$ and continuum contributions and is defined by

$$\begin{aligned} f(M_B, \cos\theta^*, tag) &= N g_{sig}(M_B).h_{sig}(\cos\theta^*).s(-tag) \\ &\quad + \overline{N} g_{sig}(M_B).h_{sig}(\cos\theta^*).s(tag) \\ &\quad + g_{back}.h_{back}. \end{aligned} \tag{4.4}$$

Thus the log likelihood function $\mathcal{L}$ as defined in eqn 4.3 is given by

$$\mathcal{L} = \sum_n -\ln \frac{f(M_B, \cos\theta^*, tag)}{\int\int\int f(M_B, \cos\theta^*, tag) d(M_B) d(\cos\theta^*) d(tag)}. \tag{4.5}$$

N and $\overline{N}$ are free parameters which give the relative probabilities of the B and $\overline{B}$ with respect to the background contribution. The aim of the fit is to optimise the free parameters to get the minimum value of $\mathcal{L}$. The M_B distribution for the signal as shown in figure 4.2 can be parameterised by two functions: (a) a Gaussian (see eqn. B.1 of Appendix B.1) or (b) a log normal distribution (see eqn. B.2 of Appendix B.1). The Gaussian does not account for the lower mass tail of the distribution and thus the log normal provides a better fit as seen in figure 4.4. The disadvantage of using the log normal distribution over the Gaussian is that it has one extra free parameter which will be unfavourable in a low statistics environment as discussed in section 4.6. The M_B distribution of the background is fitted by the function given in eqn. B.3 of Appendix B.1. Figure 4.2d shows that the distribution in $\cos\theta^*$ for the signal is flat and a constant was used in the fit. The parameterisation of the background component has been chosen to be Gaussian in $|\cos\theta^*|$ plus a constant term (see eqn. B.4 of Appendix. B.2). The function s in eqn. 4.4 is given by

$$s(x) = \int_{-\infty}^{x} \delta(x')dx'. \tag{4.6}$$

In minimising $\mathcal{L}$, the free parameters in the fit functions are determined from the Monte Carlo, leaving only N and $\overline{N}$ as free parameters to be determined by the fit. The

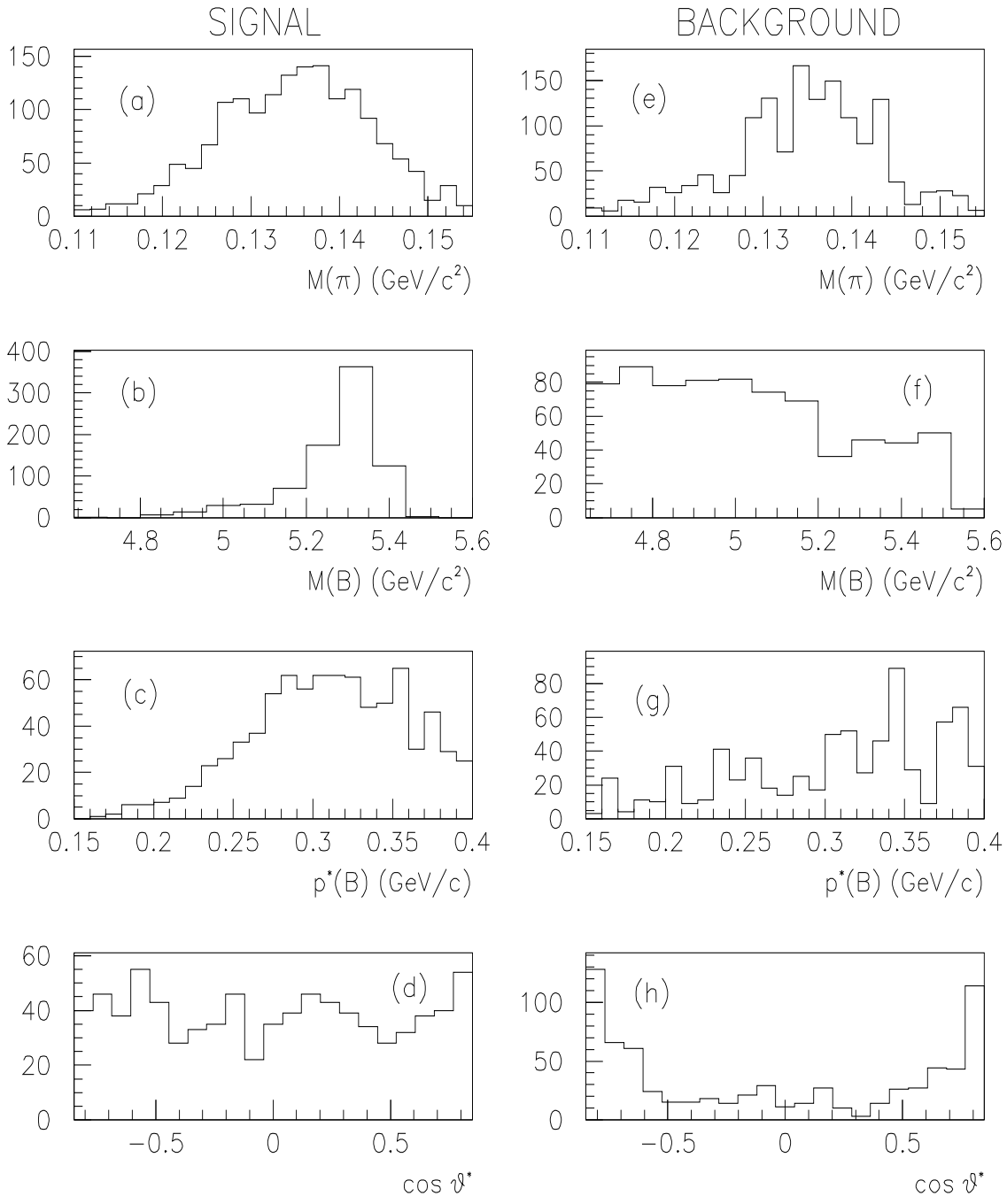

Figure 4.2: Projections of event distributions after selection for (a-d) signal, (e-h) continuum background. The relative normalisation is arbitrary.

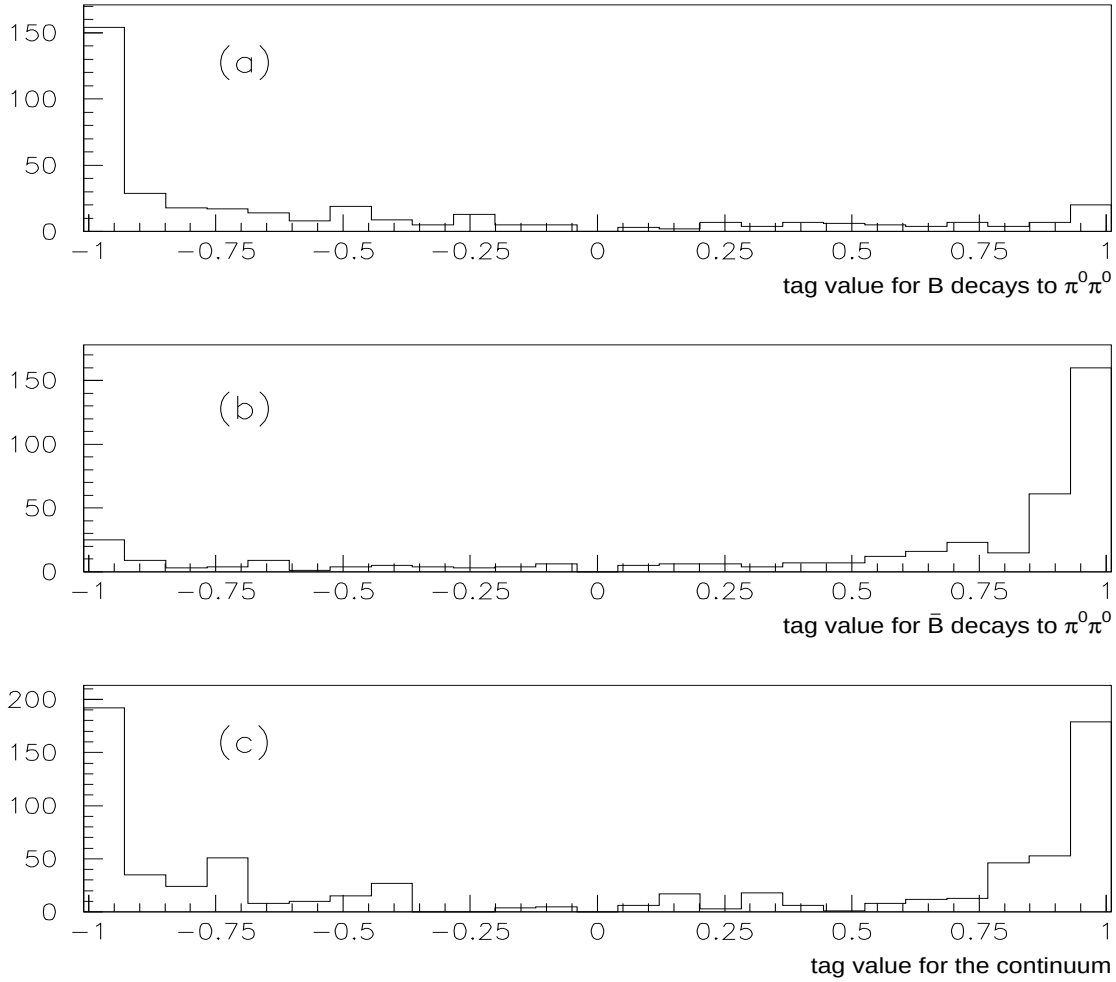

Figure 4.3: Tag value distributions for (a) $B \longrightarrow \pi^0\pi^0$; (b) $\overline{B} \longrightarrow \pi^0\pi^0$ and (c) continuum events.

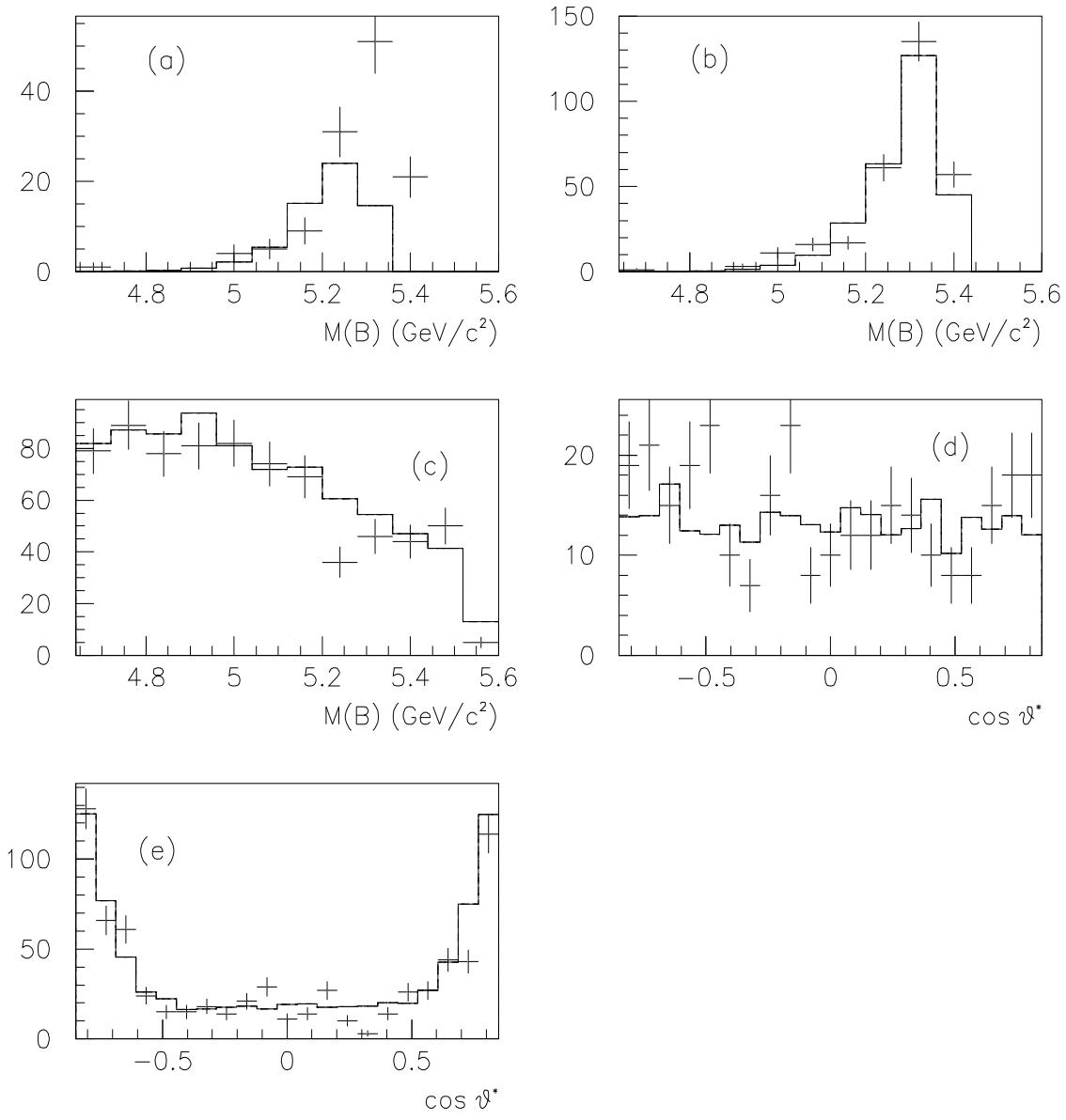

Figure 4.4: Comparisons of the fit functions used with the actual distributions. The functions are the solid lines, and the Monte Carlo distributions are the crosses. (a) shows the signal M_B described as a Gaussian; (b) describes signal M_B using a log normal distribution; (c) shows the continuum M_B distribution; (d) shows the signal $\cos\theta^*$ distribution; and (e) shows the continuum $\cos\theta^*$ distribution.

Rate of $B \longrightarrow \pi^0\pi^0$	Measured Rate	Rate of $\overline{B} \longrightarrow \pi^0\pi^0$	Measured Rate
0.0	$(0.9 \pm 0.8) \times 10^{-6}$	0.0	$(0.02 \pm 0.65) \times 10^{-6}$
1×10^{-6}	$(1.8 \pm 0.9) \times 10^{-6}$	1×10^{-6}	$(0.63 \pm 0.76) \times 10^{-6}$
5×10^{-6}	$(4.8 \pm 1.4) \times 10^{-6}$	5×10^{-6}	$(4.7 \pm 1.3) \times 10^{-6}$
9×10^{-6}	$(8.3 \pm 1.7) \times 10^{-6}$	9×10^{-6}	$(7.7 \pm 1.7) \times 10^{-6}$

Table 4.3: Table of measured branching fractions for a series of fits.

systematic errors arising as a result of determining these parameters from the Monte Carlo are discussed in section 4.7.2. The fit functions compared to their respective components within the data are shown in figure 4.4.

4.7.1 Fit results and interpretation

The mis-tag probability, ϵ, determined from the tag distributions in figure 4.3 is 0.2. Given b_m and $\overline{b}_m$ as the uncorrected B and $\overline{B}$ fractions determined from the fit, the measured rates for $B \longrightarrow \pi^0\pi^0$ and $\overline{B} \longrightarrow \pi^0\pi^0$ are given by:

$$b_r = \frac{(1-\epsilon)b_m - \epsilon\overline{b}_m}{(1-2\epsilon)E} \tag{4.7}$$

$$\overline{b}_r = \frac{(1-\epsilon)\overline{b}_m - \epsilon b_m}{(1-2\epsilon)E}, \tag{4.8}$$

where E is the signal reconstruction efficiency. The statistical errors arising from these fits for a selection of branching fractions are shown in Table 4.3 and the projections for these fits are shown in figure 4.5. If the expectation values of the errors for the given branching fractions are to be the mean of the B and $\overline{B}$ errors as given Table 4.3, then the time evolution of errors given in terms of the statistical significance is shown in figure 4.6. The statistical significance is defined as the number of observed events divided by the error of the measurement. It gives an indication of how well these branching fractions can be measured with time. For branching fractions of 9×10^{-6}, 5×10^{-6} and 1×10^{-6}, the expected number of events for a year's running at design luminosity are 324, 180 and 36 respectively.

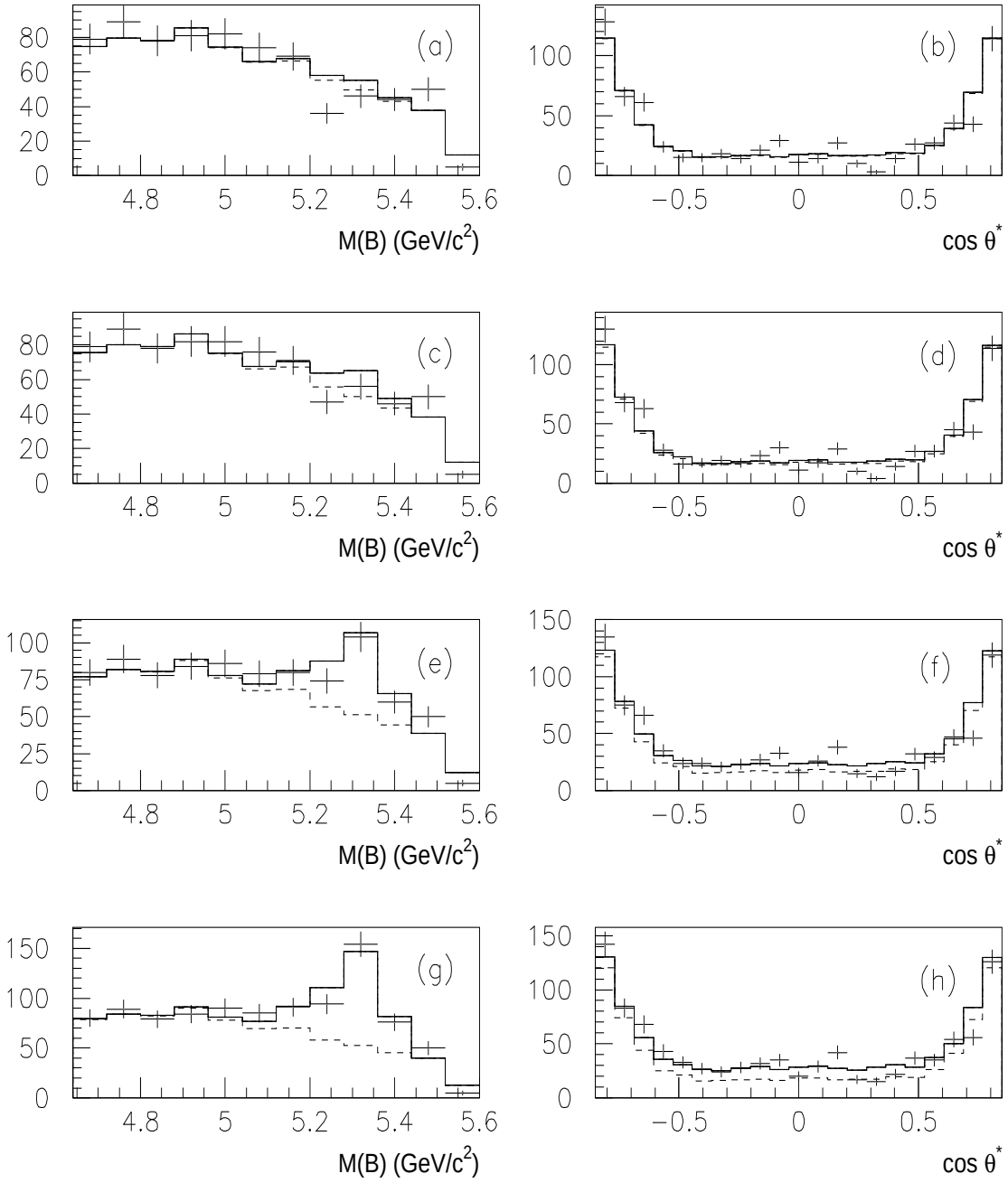

Figure 4.5: Projections showing results from a selection of fits. The crosses are the distributions from the Monte Carlo, the overall fit is the solid line, and the dashed line is the extracted continuum component. Plots are shown for a $B \longrightarrow \pi^0\pi^0$ rate of (a-b) 0.0, (c-d) 1×10^{-6}, (e-f) 5×10^{-6}, and (g-h) 9×10^{-6}. The rate for $\overline{B}$ decays is assumed to be identical to the B rate.

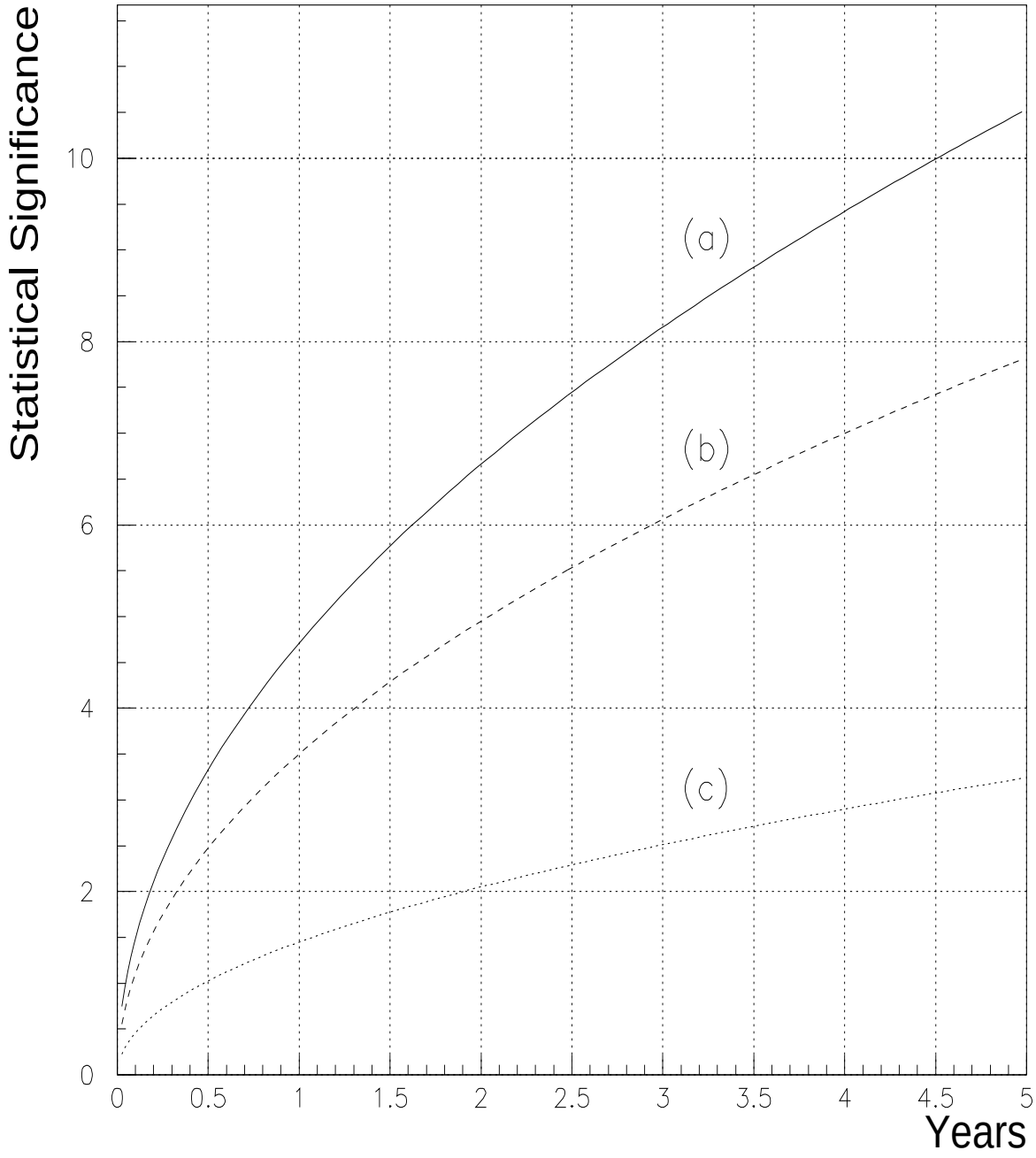

Figure 4.6: Projections of the statistical significance of the fit measurement of the branching fraction for branching fractions of (a) 9×10^{-6}; (b) 5×10^{-6}; and (c) 1×10^{-6}.

4.7.2 Evaluation of systematic errors

Some possible systematic errors in the fit arise from uncertainties in the mis-tag probability, the signal reconstruction efficiency and the signal and background line shapes It

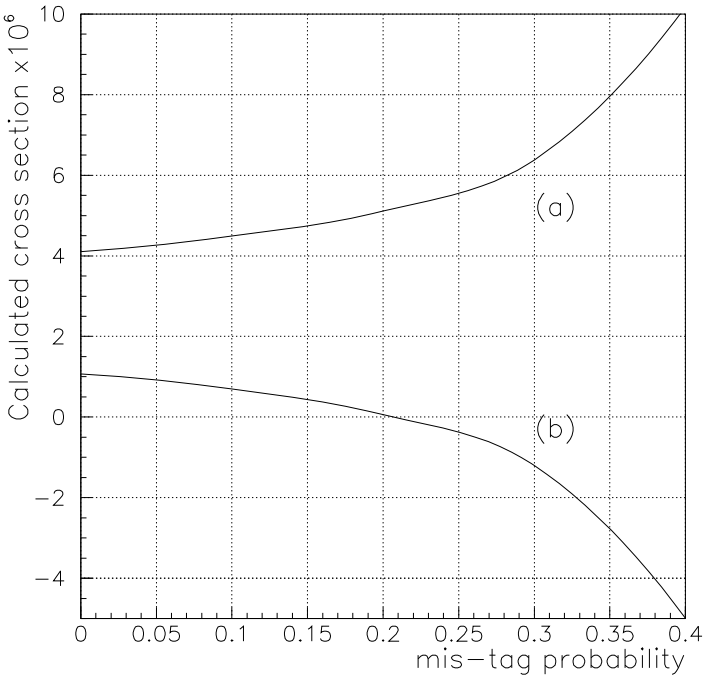

Figure 4.7: Sensitivity of the fit results to the measured mis-tag probability. The results shown are for a fit where the rate of $B \longrightarrow \pi^0\pi^0$ is 5×10^{-6}, and the rate of $\overline{B} \longrightarrow \pi^0\pi^0$ is zero. The curves are for the calculated rates of (a) $B \longrightarrow \pi^0\pi^0$ and (b) $\overline{B} \longrightarrow \pi^0\pi^0$.

will be possible to determine the mis-tag probability directly from the data by studying the tag results of events where both the B and $\overline{B}$ decay to tag modes. The degree of uncertainty in the determination of this can be a potential source of error as seen in eqns. 4.7 and 4.8. The sensitivity of the measured rates to the mis-tag probability has been investigated by performing a fit with a $B \longrightarrow \pi^0\pi^0$ branching fraction of 5×10^{-6} and no $\overline{B}$ events. By stepping the assumed mis-tag probability a variation in the measured rates is observed with no strong sensitivity in the 0.2 region (see figure 4.7). The systematic errors from the reconstruction efficiency is unavoidable since the Monte Carlo is the only way of determining the efficiency. The degree of accuracy to which the Monte Carlo can determine this to be the true value in the data will determine the level of this

error. For this study it is arbitrarily decided that the reconstruction efficiency can be determined to within $\pm 5\%$ (ϵ_{reco}). Systematic errors arise due to the uncertainties in the determination of the signal line shapes from the Monte Carlo. The systematic errors due to fixing of the parameters in the background function are negligible. The reason being that in the real data there will always be enough continuum events and hence it will be possible to extract the background line shape of the fit function from the data to any degree of accuracy by considering sideband regions around the signal in M_B and $\cos\theta^*$ distributions. To investigate the effect of this on the measurements made, the resolution on the M_B^{mean} (σ) has been varied with respect to the optimal value. If it is assumed that the Monte Carlo can be trusted to within $\pm 5\%$, then an error of $\pm 2\%$ is observed on the measured cross section as seen in figure 4.8(a). By varying M_B^{mean} about the optimal value and assuming that the distribution can be determined to within $\pm 10 MeV/c^2$, an error of $\pm 2\%$ is also observed. A conservative estimate of $\pm 6.5\%$ is chosen as the systematic error if it is assumed that a Gaussian rather than a log normal distribution is used to describe the M_B line shape. The overall error on the measured rates is then obtained by adding in quadrature the statistical error and the systematic errors and is given by

$$\epsilon_{total} = \epsilon_{fit} \oplus \epsilon_{reco} \oplus \epsilon_{lineshape}. \tag{4.9}$$

The time evolution of errors showing the effects of the systematics is shown in figure 4.9.

4.8 $B^+ \longrightarrow \pi^+\pi^0$

Plots in figures 4.10 and 4.11 show significant differences in signal and background distributions hence the selected list of discriminating variables is:

- M_B = the invariant mass of the B^+;
- p^* = the momentum of the B^+ in the $\Upsilon(4S)$ rest frame;
- $\cos\theta^*$ = cosine of the B sphericity angle in the $\Upsilon(4S)$ rest frame;
- Prob(π) = the probability that the selected charged particle is a pion;
- Prob(k) = the probability that the selected charged particle is a Kaon.

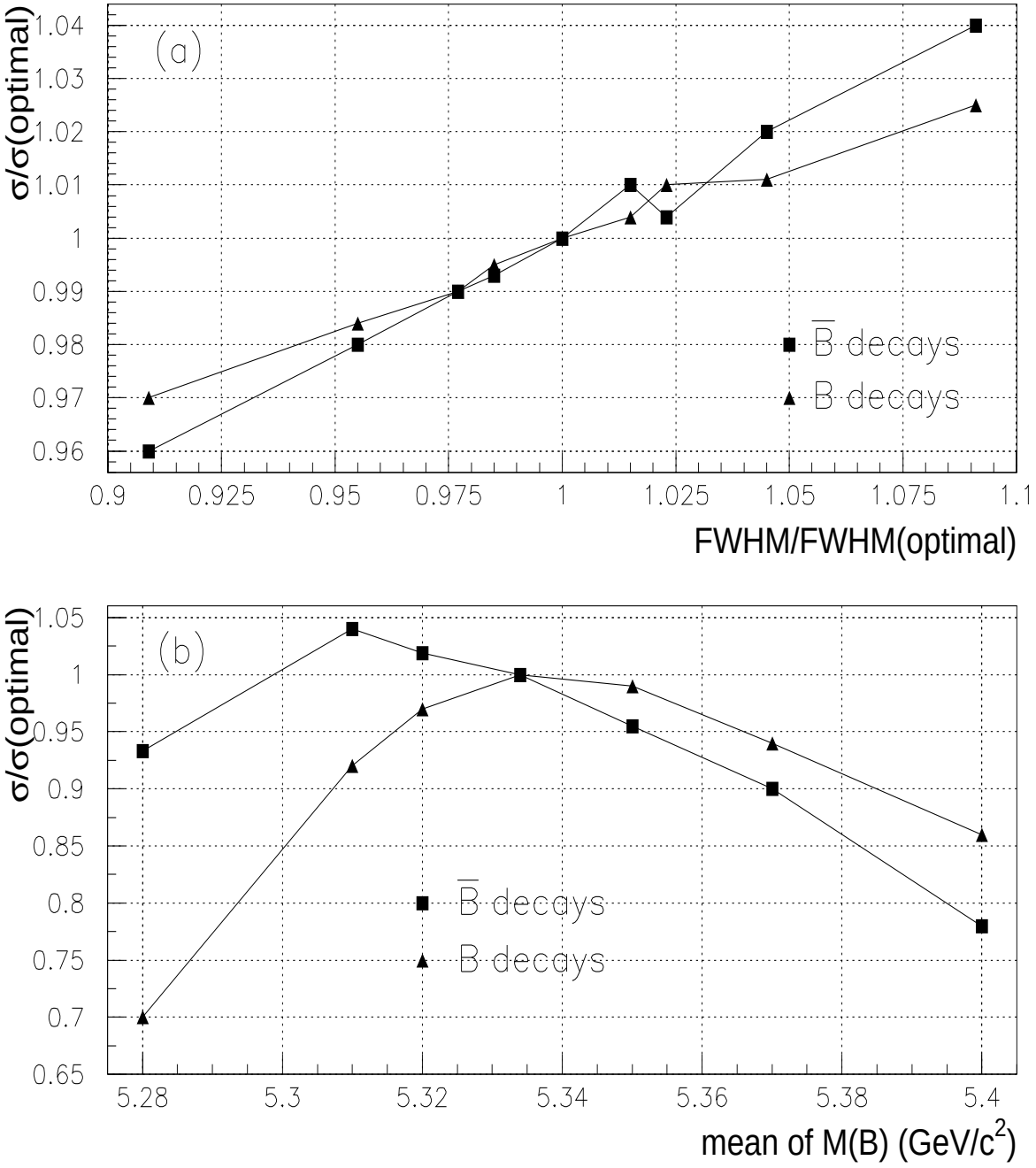

Figure 4.8: Variation of the measured cross section with respect to (a) the FWHM of the signal M_B distribution and (b) the mean of the signal M_B distribution. Curves are shown for the $\overline{B} \longrightarrow \pi^0\pi^0$ and $B \longrightarrow \pi^0\pi^0$ components. The true rates for B and $\overline{B}$ decays has been taken to be 9×10^{-6} for these fits.

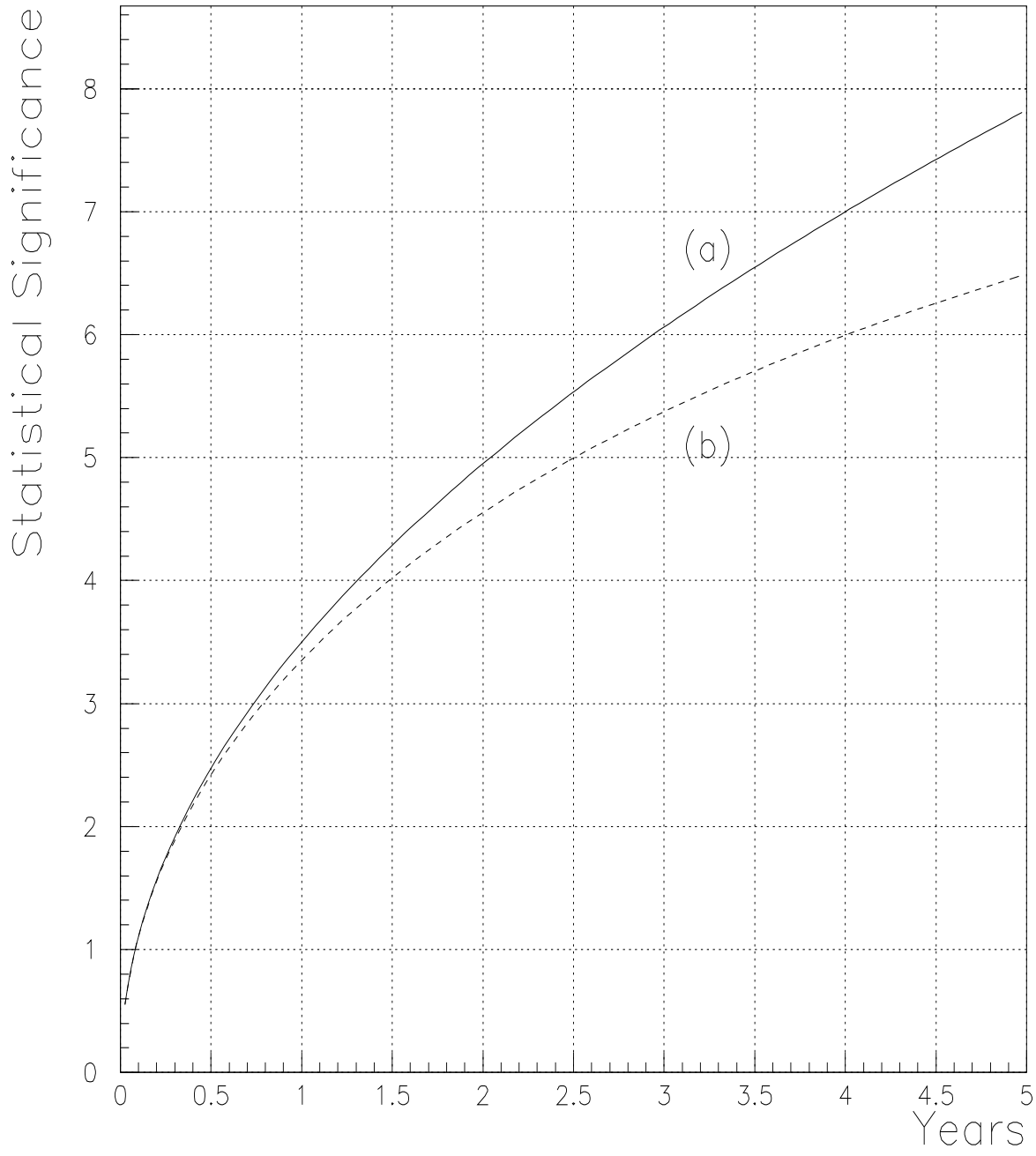

Figure 4.9: Time evolution of errors when the rate of $B \longrightarrow \pi^0\pi^0$ is 5×10^{-6}. Curves are shown for (a) the statistical error arising from the fit and (b) the statistical and the systematic errors added in quadrature.

Cut	% of events passed	% of events passed with a correct solution	No. of combinatorial solutions per event
No Cuts	98.6	73.5	24.4
$0.11 < M_\pi < 0.155$	96.6	70.5	23.9
$5.0 < M_B < 5.55$ (GeV/c)	70.7	69.8	1.05
$0.15 < p^* < 0.40$ (GeV/c)	60.3	59.6	1.03
$-0.85 < \cos\theta^* < 0.85$	50.1	49.5	1.02
Prob(π) > 0.05 and Prob(k) < 0.05	46.9	46.4	1.02
No. Solutions = 1	46.9	45.9	1.00

Table 4.4: Signal efficiencies for the applied cuts. The quoted efficiencies are cumulative.

Cuts are made against these variables with an additional cut requiring that only one combinatorial solution in a given event passes these cuts. The benefits of this additional cut is as explained in section 4.7. Figures 4.10 and 4.11 show projections of the event distributions obtained from the simulation. Plots are shown for true signal events, their associated combinatorial background and for continuum events.

Table 4.4 shows the cuts applied and the efficiencies obtained. The background efficiency of $(7.33 \pm 0.30) \times 10^{-6}$ is obtained after all cuts. Projections for the selected events are shown in figure 4.12. In fitting the data two discriminating variables are considered: M_B and $\cos\theta^*$. The aim is to minimise the log likelihood function $\mathcal{L}$ given by

$$\mathcal{L} = \sum_n -\ln \frac{f(M_B, \cos\theta^*)}{\int\int f(M_B, \cos\theta^*) d(M_B) d(\cos\theta^*)}, \tag{4.10}$$

where $f(M_B,\ \cos\theta^*)$ is the sum of the B and background distributions as defined by eqn. 4.11.

$$\begin{aligned} f(M_B, \cos\theta^*, tag) &= N g_{sig}(M_B).h_{sig}(\cos\theta^*) \\ &\quad + g_{back}.h_{back}, \end{aligned} \tag{4.11}$$

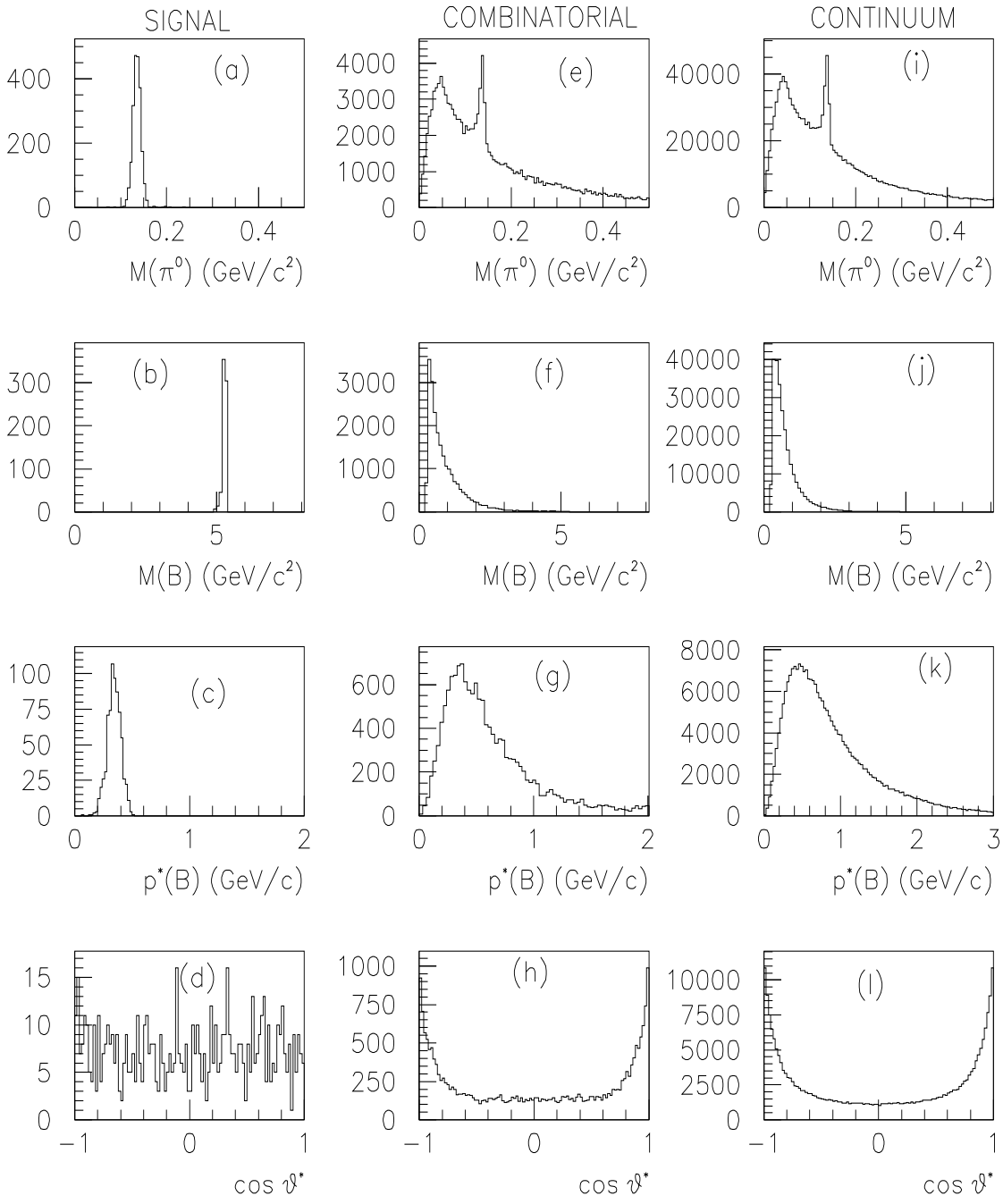

Figure 4.10: Plots of reconstructed π^0's for (a) signal, (b) combinatorial (c) continuum and projections of the selected discriminating variables for (b-d) correctly constructed signal, (f-h) combinatorial background, and (j-l) continuum background. No cuts are applied for the π^0 mass plots. For all other plots it is required that $0.11 < M_\pi < 0.155\,GeV/c^2$. The plots are shown with arbitrary normalisation.

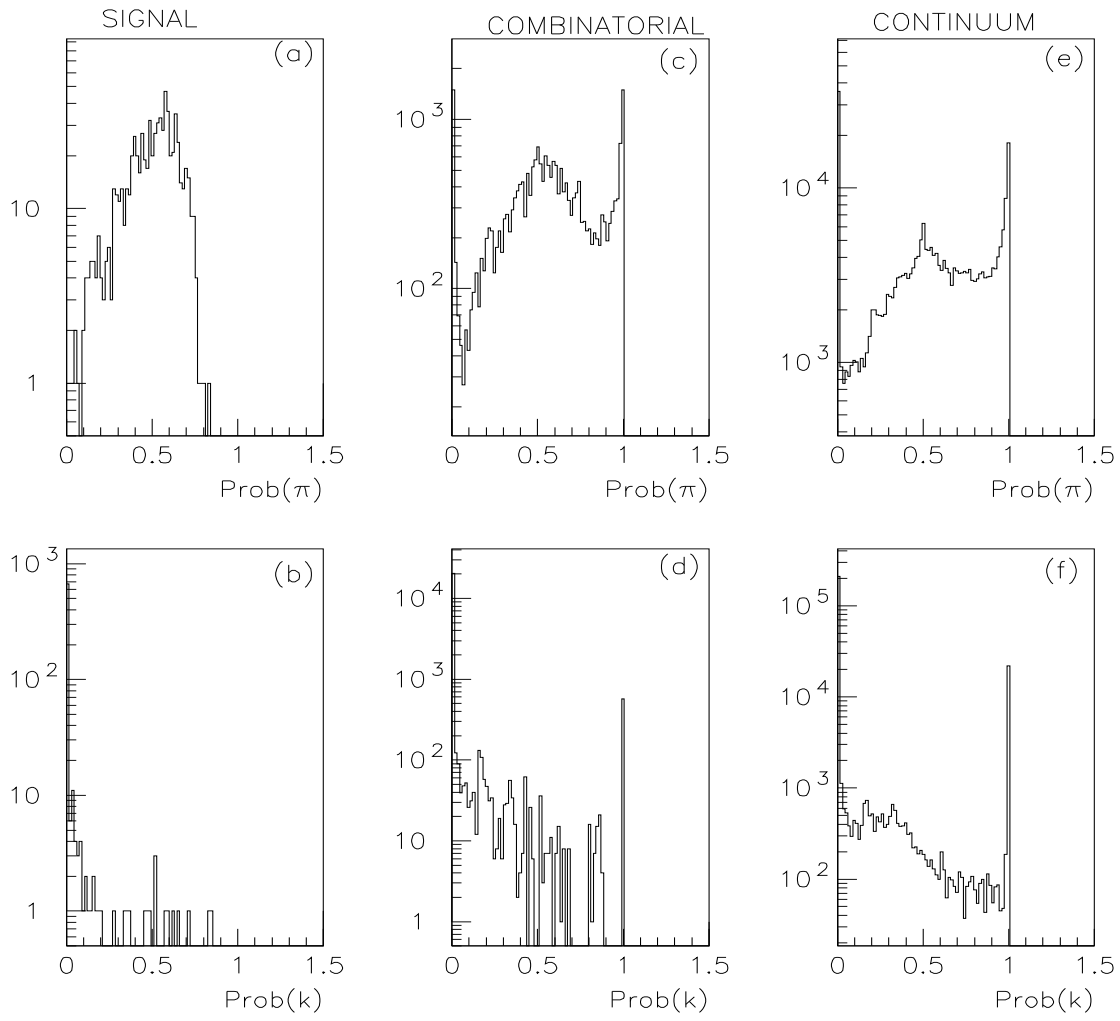

Figure 4.11: Projections of pion and Kaon probability distributions for (a-b) correctly constructed signal, (c-d) combinatorial background and (e-f) continuum background. The plots are shown with arbitrary normalisation.

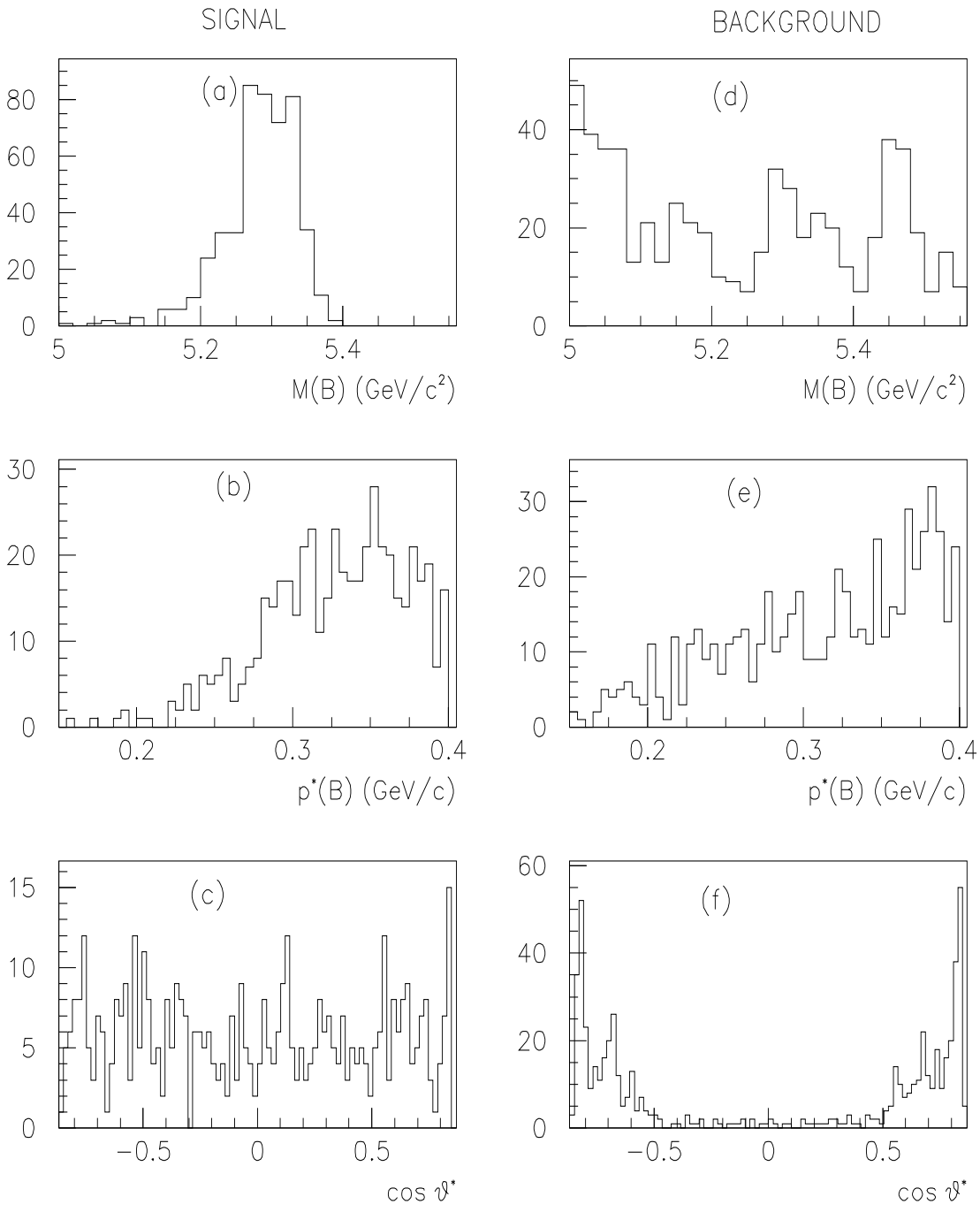

Figure 4.12: Projections of event distribution after selection for (a-c) signal, (d-e) continuum background. The relative normalisation is arbitrary.

where N is a free parameter to be determined by the fit and which gives the relative probabilities of the B and background contributions. The signal distribution is parameterised by a Gaussian, i.e. $g_{sig}(M_B)$ as defined in eqn. B.1 of Appendix B.1. The parameterisation of the background distribution, i.e. $g_{back}(M_B)$ is defined in eqn. B.3 of Appendix B.1. The $\cos\theta^*$ distribution for the signal is flat as shown in figure 4.12(c),

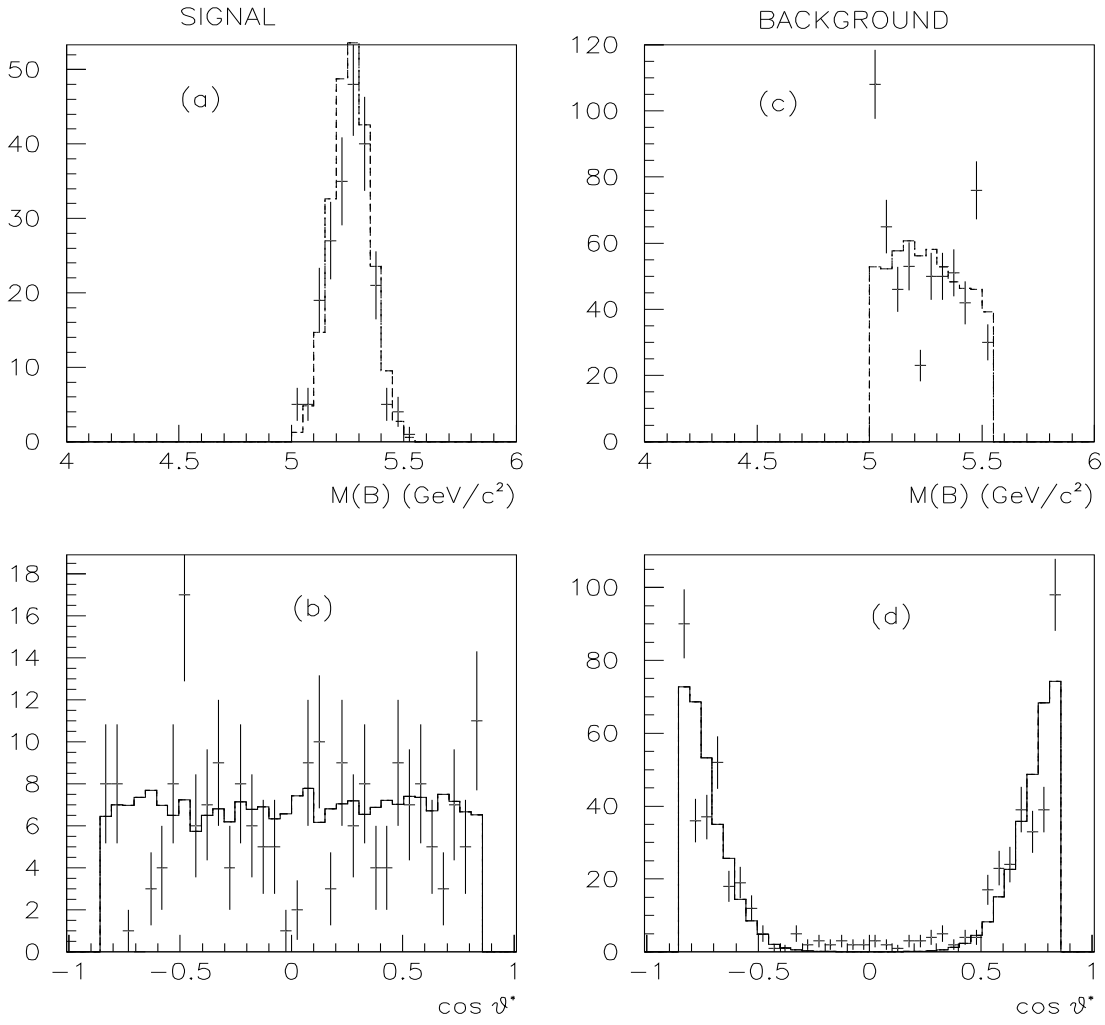

Figure 4.13: Comparisons of the fit functions used with the actual distributions. The functions are the solid lines, and the Monte Carlo distributions are the crosses. (a) shows the signal M_B described as a Gaussian, (b) describes signal $\cos\theta^*$ distribution, (c) shows the continuum M_B distribution and (d) shows the continuum $\cos\theta^*$ distribution.

thus a constant was used in the fit. The background distribution is parameterised by

a Gaussian with a constant term (eqn. B.4 of Appendix B.2). In minimising $\mathcal{L}$ all free parameters in the signal (see eqn. 4.10) are determined from the Monte Carlo and the parameters in the background function have been fixed by considering sideband regions around the signal in the in M_B and $\cos\theta^*$ distributions of the data, leaving N as the only free parameter to be determined by the fit. The systematic errors as result of this are discussed in section 4.8.2. The fit functions compared to their respective components within the data are shown in figure 4.13.

4.8.1 Fit results and interpretation

Given b_{m1} as the B fraction determined from the fit and the signal reconstruction efficiency, the measured rate for $B \longrightarrow \pi^+\pi^0$ can be obtained.

Rate of $B \longrightarrow \pi^+\pi^0$	Measured Rate
0.25×10^{-5}	$(0.35 \pm 0.08) \times 10^{-5}$
0.5×10^{-5}	$(0.58 \pm 0.10) \times 10^{-5}$
1.2×10^{-5}	$(1.33 \pm 0.13) \times 10^{-5}$
2×10^{-5}	$(1.98 \pm 0.14) \times 10^{-5}$

Table 4.5: Table of measured branching fractions for a series of fits.

Table 4.5 shows the statistical error from the fit for a selection of the branching fraction. Projections of the fits are shown in figure 4.14. The effects of systematic errors are discussed in section 4.8.2. The evolution of errors with time are shown in figure 4.15. The errors are quoted in terms of the statistical significance of the measurement.

4.8.2 Evaluation of systematic errors

Sources of systematic errors that have been considered are the uncertainty in the signal reconstruction efficiency and the uncertainty in the signal and background line shapes. For this study the systematic error arising from the signal reconstruction efficiency has been arbitrarily chosen to be within $\pm 5\%$. In determining the systematics due to signal line shapes, the M_B resolution used in the fit has been varied with respect to the optimal value. The error on the observed number of events due to this effect assuming that the

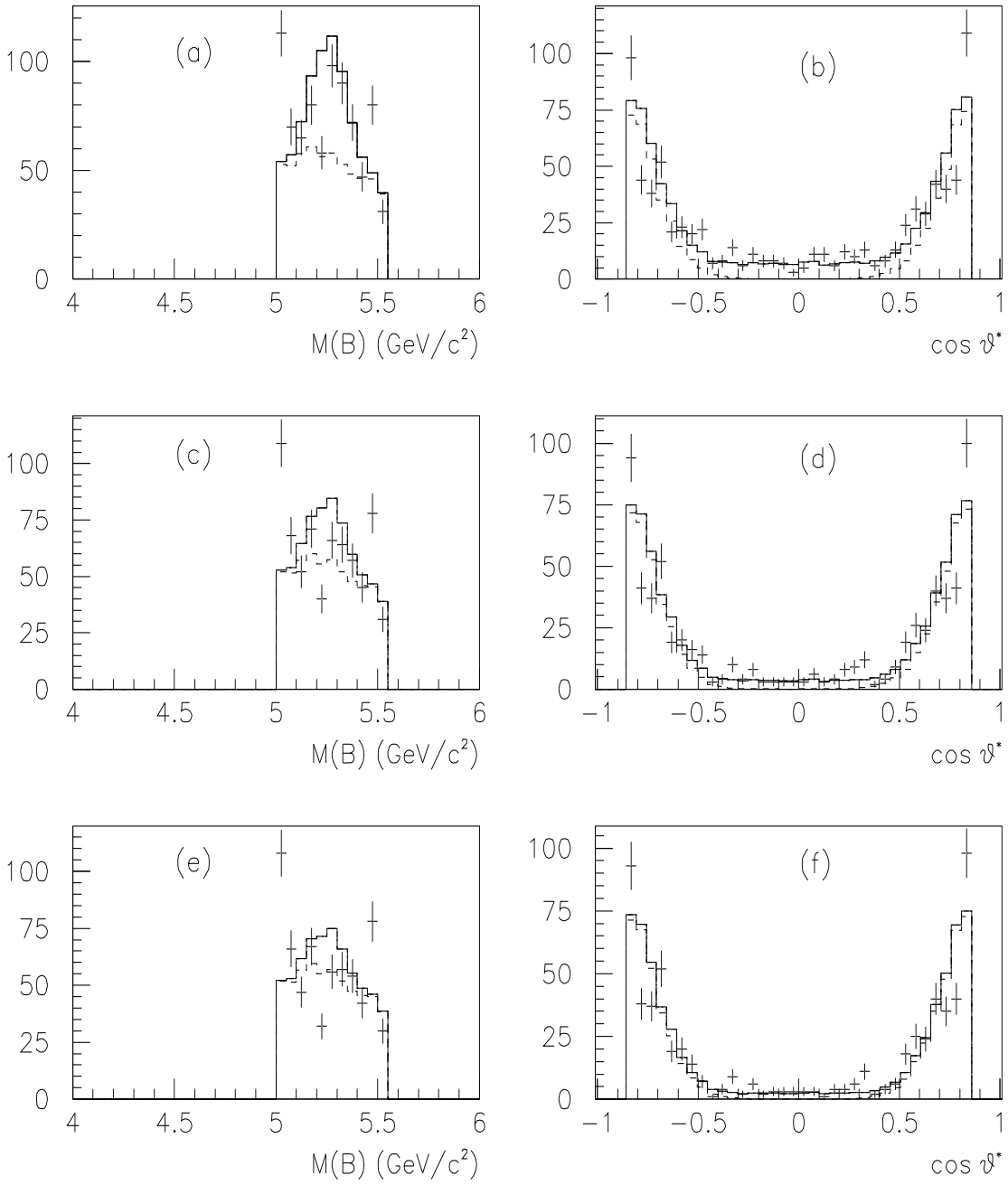

Figure 4.14: Projections showing results from a selection of fits. The crosses are the data, the overall fit is the solid line, and the dashed line is the extracted continuum component. Plots are shown for a $B \longrightarrow \pi^+\pi^0$ rate of (a-b) 1.2×10^{-5}, (c-d) 0.5×10^{-5} and (e-f) 0.25×10^{-5}

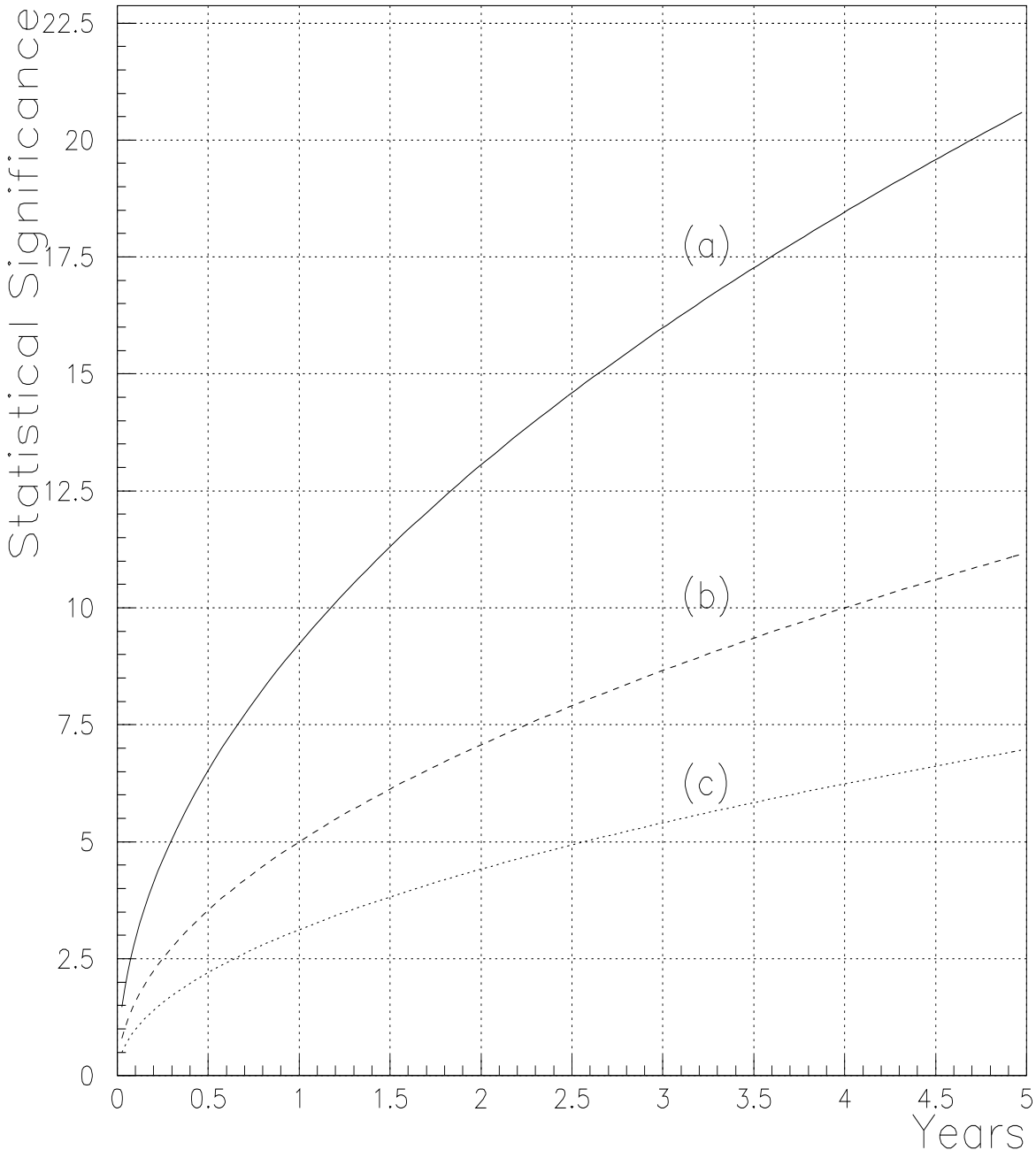

Figure 4.15: Projections of the statistical significance of the fit measurement of the branching fraction for branching fractions of (a) 1.2×10^{-5}; (b) 0.5×10^{-5}; and (c) 0.25×10^{-5}.

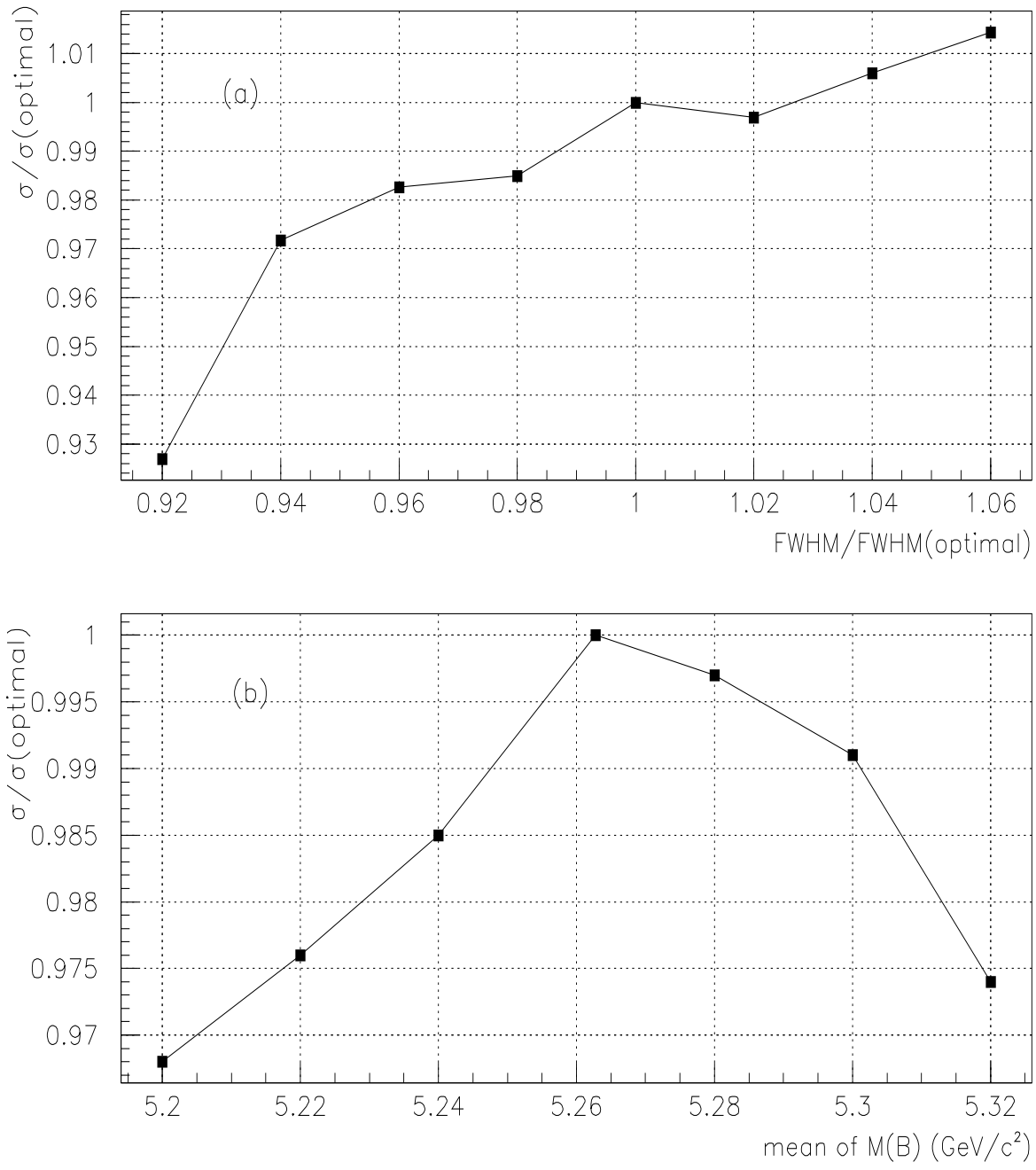

Figure 4.16: Variation of the measured cross section with respect to (a) the FWHM of the signal M_B distribution and (b) the mean of the signal M_B distribution. Curves are shown for $B^+ \longrightarrow \pi^+\pi^0$. The true rate has been taken to be 2×10^{-5} for these fits.

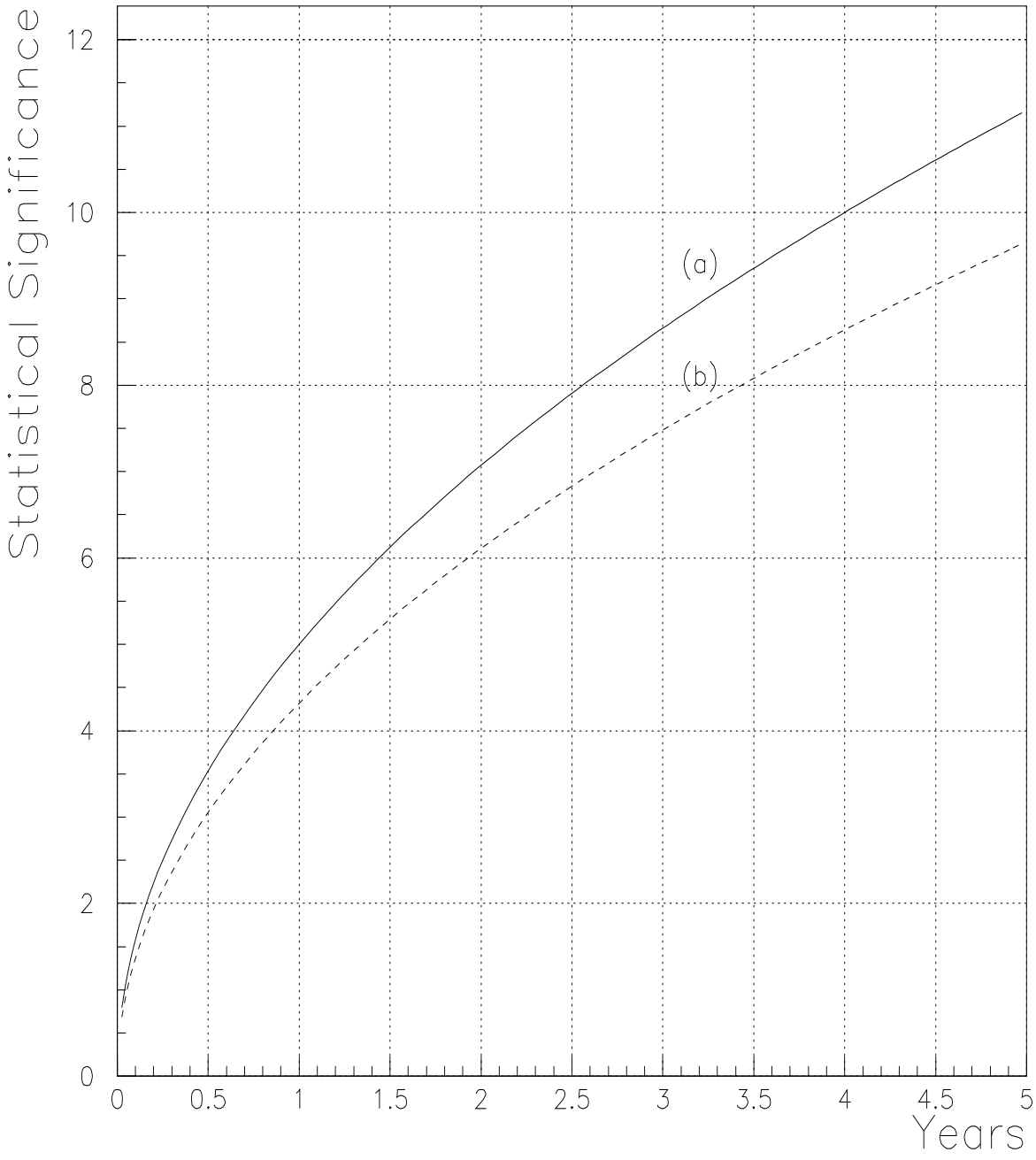

Figure 4.17: Time evolution of errors when the rate of $B^+ \longrightarrow \pi^+\pi^0$ is 0.5×10^{-5}. Curves are shown for (a) the statistical error arising from the fit and (b) the statistical and the systematic errors added in quadrature.

Monte Carlo simulation can be trusted to within ±5%, is ±3% (see figure 4.16(a)). If it is assumed that the mean of the M_B can be determined to within $\pm 10 MeV/c^2$, then an error of ±1% can be observed (see figure 4.16(b)). The systematics due to the background line shape is negligible for the same reasons as discussed in section 4.7.2. The final error on the measured rate is then given by

$$\epsilon_{total} = \epsilon_{fit} \oplus \epsilon_{reco} \oplus \epsilon_{lineshape}. \tag{4.12}$$

Adding the errors in quadrature results in the plot given in figure 4.17.

4.9 $B^0 \longrightarrow \pi^+\pi^-$

From figures 4.13 and 4.14 significant differences are shown in signal and background distributions. Thus the selected discriminating variables are:

- M_B = the invariant mass of the B^0;
- p^* = the momentum of the B^0 in the $\Upsilon(4S)$ rest frame;
- $\cos\theta^*$ = cosine of the B sphericity angle in the $\Upsilon(4S)$ rest frame;
- Prob(π) = the probability that the selected charged particle is a pion;
- Prob(k) = the probability that the selected charged particle is a Kaon;
- tag = the tag value;
- t = the time difference between B^0 and $\overline{B}^0$ decays.

Cuts are made against these variables with an additional cut requiring that only one combinatorial solution in a given event passes these cuts. There is no effect on signal efficiency as a result of this additional cut. Figures 4.18 and 4.19 show projections of the event distributions obtained from the simulation. Plots are shown for true signal events, their associated combinatorial background and for continuum events. Projections of the tag distributions for the B, $\overline{B}$ and the continuum are shown in figure 4.21. Table 4.6 shows the cuts applied and the efficiencies obtained. Projections for the selected events are shown in figure 4.22. An overall background efficiency of $(1.29 \pm 0.04) \times 10^{-5}$ is

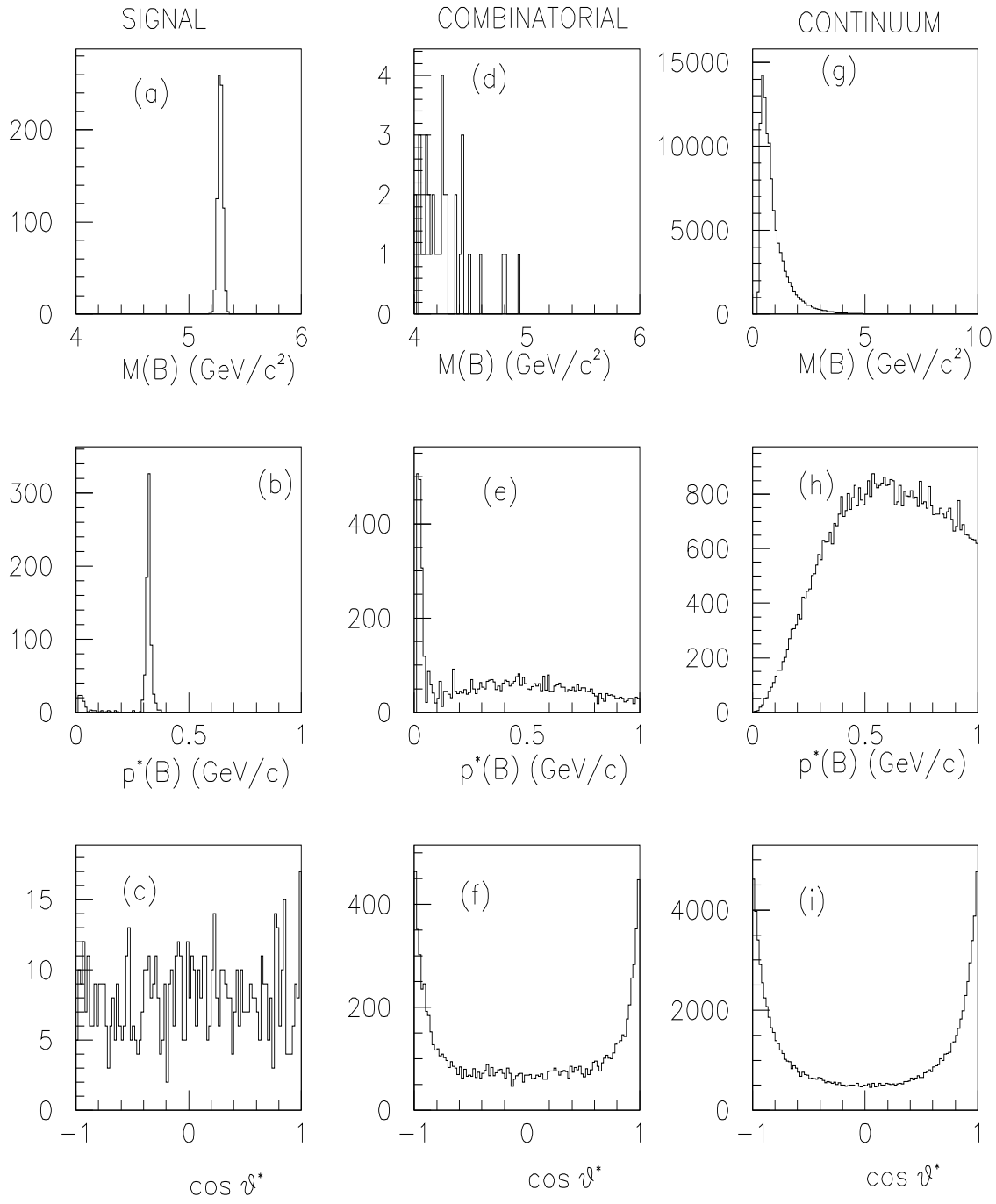

Figure 4.18: Projections of the selected discriminating variables for (a-c) correctly constructed signal, (d-f) combinatorial background, and (g-i) continuum background. The plots are shown with arbitrary normalisation.

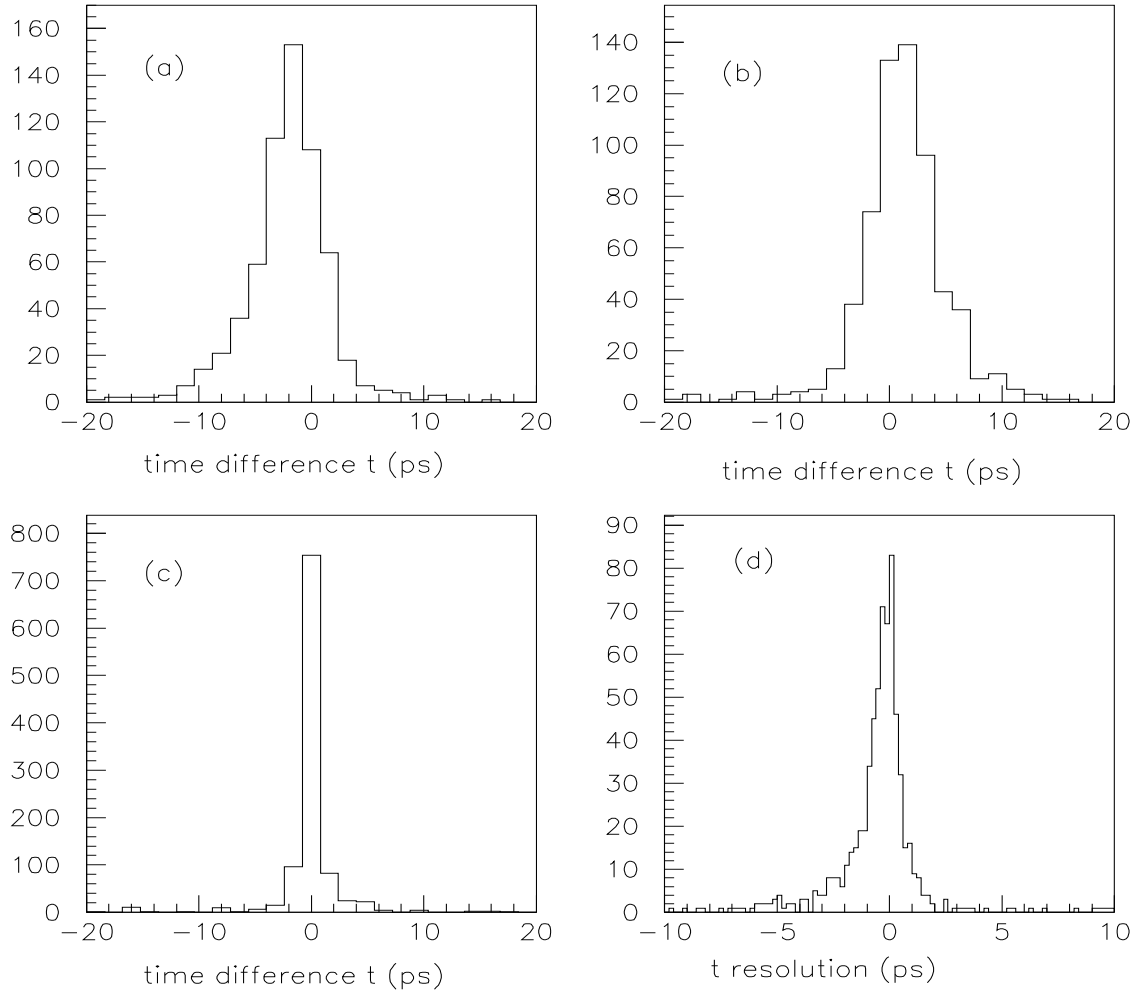

Figure 4.19: Projections of time difference for (a) correctly constructed B decays to $\pi^+\pi^-$, (b) correctly constructed $\overline{B}$ decays to $\pi^+\pi^-$ and (c) continuum background. Plot (d) is the time difference resolution for $B \longrightarrow \pi^+\pi^-$, i.e. the difference between the reconstructed time difference and that from the Monte Carlo truth information. The plots are shown with arbitrary normalisation.

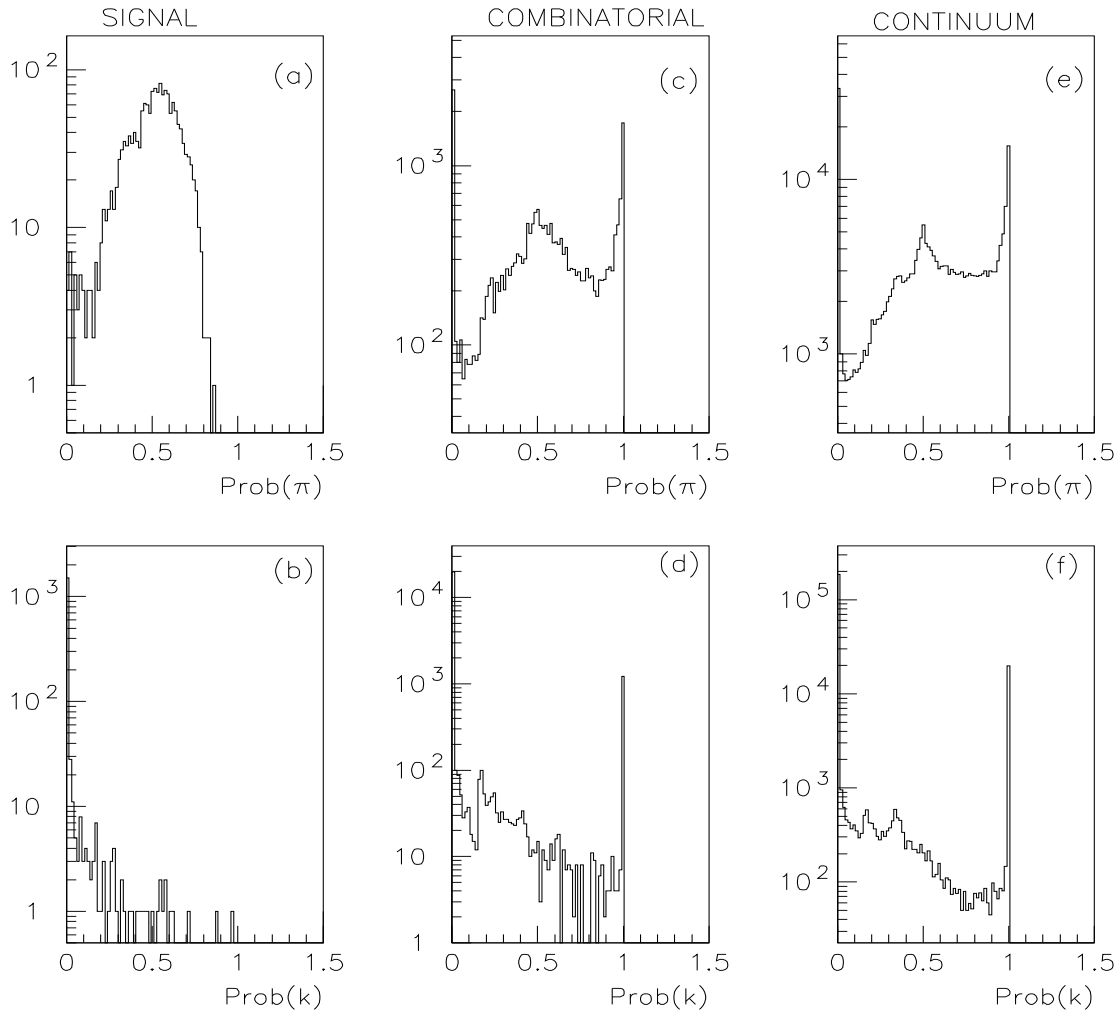

Figure 4.20: Projections of pion and Kaon probability distributions for (a-b) correctly constructed signal, (c-d) combinatorial background and (e-f) continuum background. The plots are shown with arbitrary normalisation.

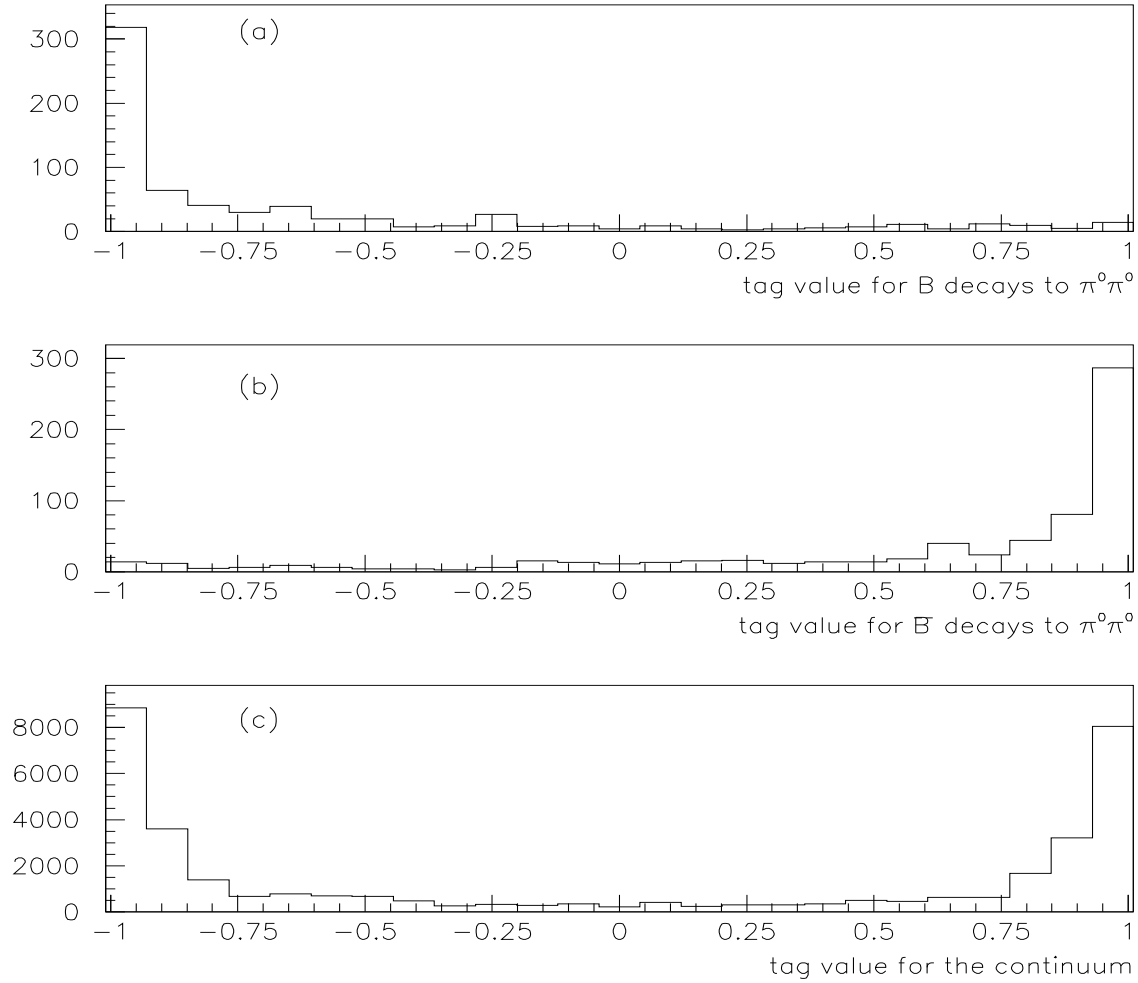

Figure 4.21: Tag value distributions for (a) $B \longrightarrow \pi^+\pi^-$; (b) $\overline{B} \longrightarrow \pi^+\pi^-$ and (c) continuum events.

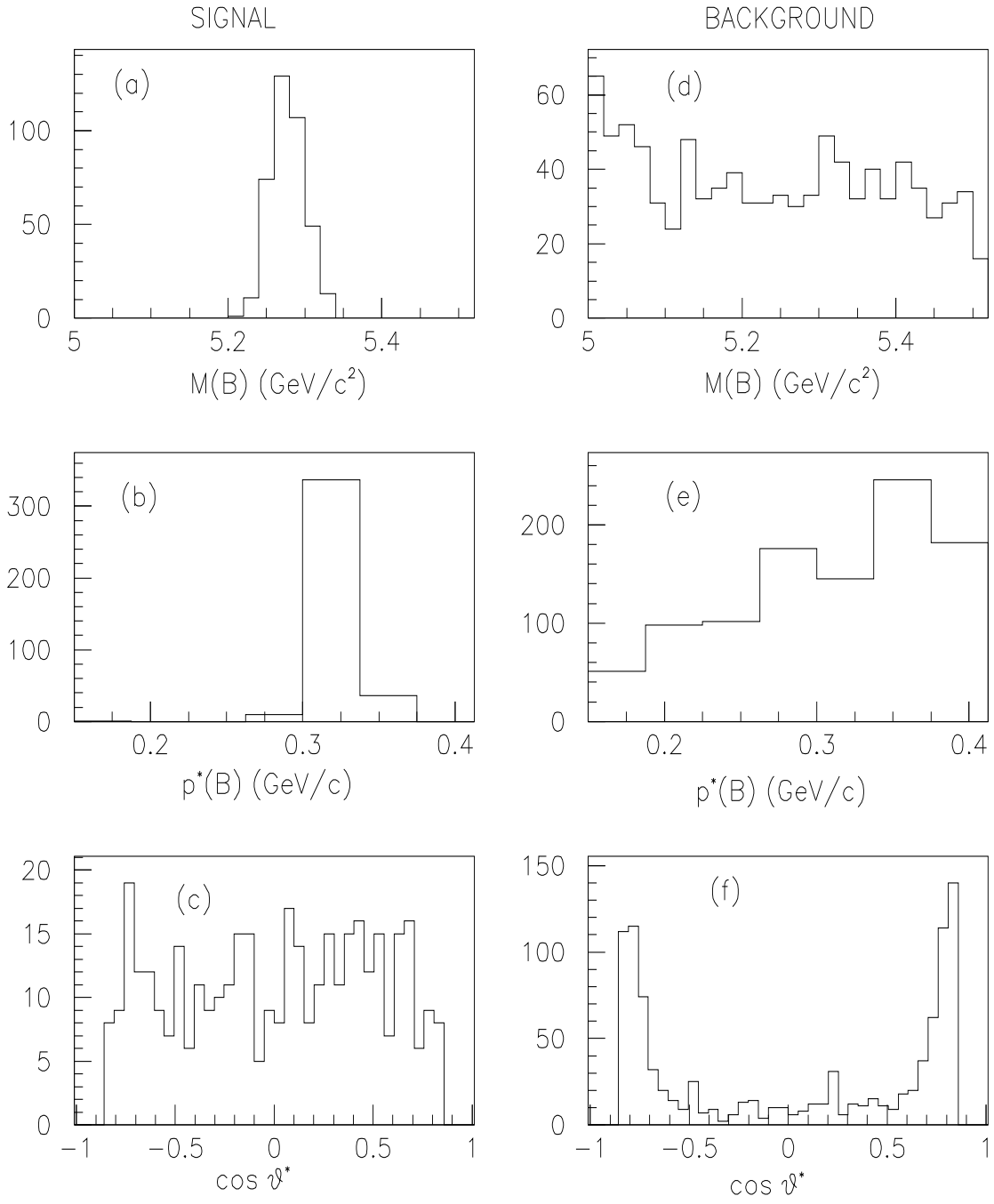

Figure 4.22: Projections of event distribution after selection for (a-c) signal and (d-f) continuum background. The relative normalisation is arbitrary.

Cut	% of Events Passed	% of Events Passed With a Correct Solution	No. of Combinatorial Solutions per event
No Cuts	99.1	85.7	1
$5.0 < M_B < 5.55$ (GeV/c)	85.7	85.7	1
$0.15 < p^* < 0.40$ (GeV/c)	77.9	77.9	1
$-0.85 < \cos\theta^* < 0.85$	63.6	63.6	1
$\|tag\| > 0.05$	62.8	62.8	1
Prob(π) > 0.05 and Prob(k) < 0.05	55.8	55.8	1
$\|t\| < 100$ ($10^{-12}s$)	55.1	55.1	1
No. Solutions = 1	55.1	54.9	1

Table 4.6: Signal efficiencies for the applied cuts. The quoted efficiencies are cumulative.

obtained after all cuts.

In constructing the fit function the discriminating variables considered here are: M_B, $\cos\theta^*$, the tag value and t. The log likelihood function $\mathcal{L}$ to be minimised is given by

$$\mathcal{L} = \sum_n -\ln \frac{f(M_B, \cos\theta^*, tag, t)}{\int\int\int\int f(M_B, \cos\theta^*, tag, t) d(M_B) d(\cos\theta^*) d(tag) d(t)}, \tag{4.13}$$

where $f(M_B, \cos\theta^*, tag, t)$ is the sum of the B, $\overline{B}$ and continuum contributions as defined by eqn. 4.13. M_B, $\cos\theta^*$, the tag value and the time difference (t) are treated as independent variables.

$$\begin{aligned} f(M_B, \cos\theta^*, tag, t) \;=\; & g_{sig}(M_B).h_{sig}(\cos\theta^*).s(-tag).P(t) \\ & + g_{sig}(M_B).h_{sig}(\cos\theta^*).s(tag).\overline{P}(t) \\ & + g_{back}.h_{back}.P_{back}. \end{aligned} \tag{4.14}$$

The free parameters N and $\overline{N}$ which form part of the $P(t)$ and $\overline{P}(t)$ functions, scale the B and $\overline{B}$ components relative to the background. From the signal distribution in figure 4.18 the most appropriate parametrisation is a Gaussian. Thus the fit function $g_{sig}(M_B)$ is as defined in eqn. B.1 of Appendix B.1. The background distribution is parameterised by the function $g_{back}(M_B)$ as defined in eqn. B.3 of Appendix B.1. Figure 4.22(c) shows the distribution in $\cos\theta^*$ for the signal component is flat and a constant was used in the fit. The background is fitted by the function described in eqn. B.4 of Appendix B.2. The function s is as given in eqn. 4.6. The time difference (t) component for the signal is described by the functions $P(t)$ and $\overline{P}(t)$ for the B and $\overline{B}$ decays respectively. $P(t)$ is the time dependent rate for B decays to $\pi^+\pi^-$ and $\overline{P}(t)$ is the time dependent rate for $\overline{B}$ decays to $\pi^+\pi^-$ (see eqns 1.14 and 1.15) defined as follows:

$$P(t) = \frac{A_n}{2} e^{-|t|/\tau} \left\{ 1 + R^{+-} \cos\Delta M t - K^{+-} \sin\Delta M t \right\} \tag{4.15}$$

$$\overline{P}(t) = \frac{A_n}{2} e^{-|t|/\tau} \left\{ 1 - R^{+-} \cos\Delta M t + K^{+-} \sin\Delta M t \right\}, \tag{4.16}$$

where $A_n = N + \overline{N}$ (the normalisation), $R^{+-} = (N - \overline{N})/(N + \overline{N}) = (|A^{+-}|^2 - |\overline{A}^{+-}|^2)/(|A^{+-}|^2 + |\overline{A}^{+-}|^2)$ (the direct CP violation parameter), $\Delta M = 0.46$ (the mass difference), $\tau = 1.5ps$ (the B lifetime) and K^{+-} is the parameter containing $\sin 2\alpha$. $|A^{+-}|$ and $|\overline{A}^{+-}|$ are the amplitudes of B and $\overline{B}$ respectively. The above equations hold in the ideal case of a detector with perfect time resolution. In the more realistic situation of

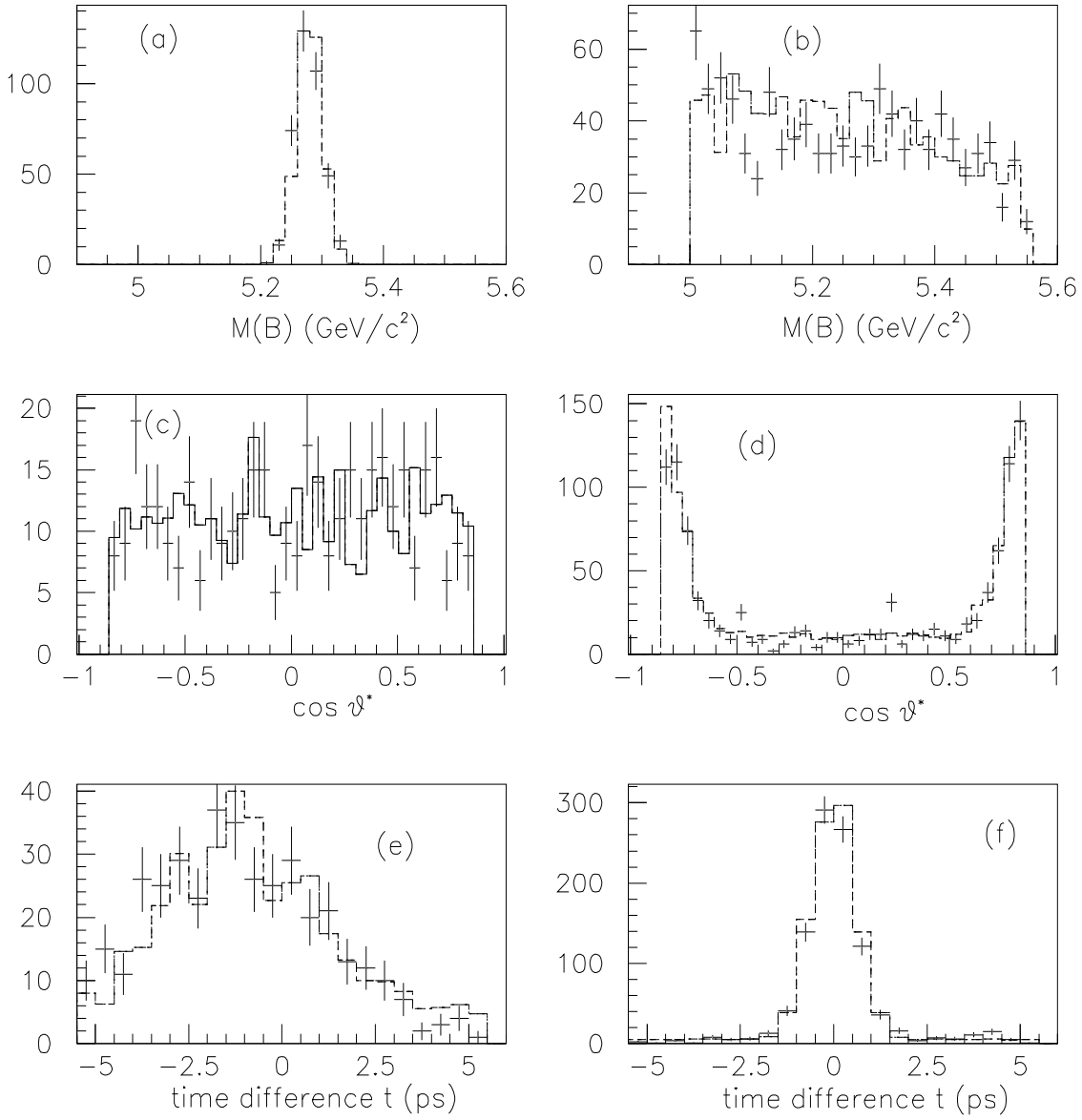

Figure 4.23: Comparisons of the fit functions used with the actual distributions. The functions are the solid lines, and the Monte Carlo distributions are the crosses. (a) shows the signal M_B described as a Gaussian, (b) shows the continuum M_B distribution, (c) describes signal $\cos\theta^*$ distribution, (d) shows the continuum $\cos\theta^*$ distribution, (e) plot of time difference distribution for B decays and (f) the time difference distribution for continuum events fitted with a double Gaussian.

a detector with finite resolution (σ_t), the correct equations are obtained from a convolution of the above equations with the Gaussian errors on t (see eqns. B.6 and B.16 of Appendix B.3). The time difference (t) component for the background is parameterised

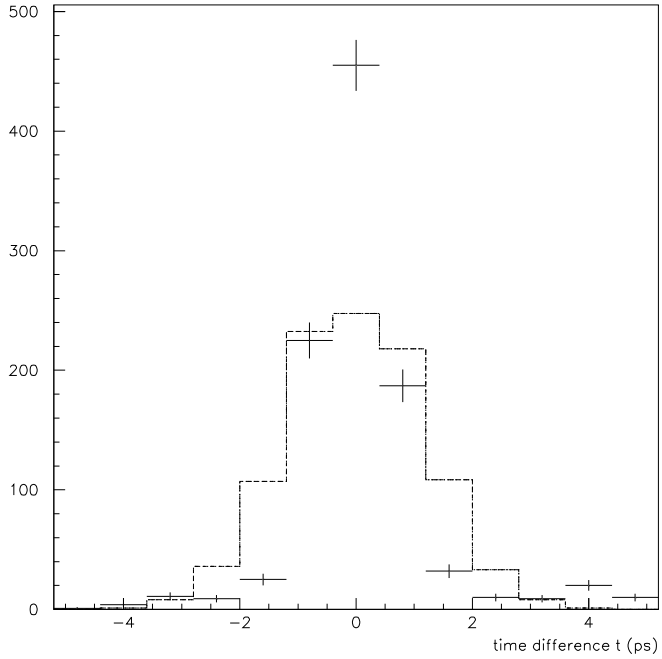

Figure 4.24: Plot of time difference distribution for the continuum fitted with a single Gaussian.

by the double Gaussian given in eqn. B.17 of Appendix B.3. The choice of a double Gaussian over a single Gaussian is for the fact that it gives a better fit as can be seen in figures 4.23f and 4.24. In minimising $\mathcal{L}$ the only free parameters to be determined by the fit are N, $\overline{N}$ and K^{+-}. All others have been determined in the same manner as discussed in sections 4.7 and 4.8. The systematic errors as a result of this are discussed in section 4.9.2. Plots of the fit functions compared to their respective components within the data are showed on figure 4.23.

Rate of $B \longrightarrow \pi^+\pi^-$	Measured Rate	Rate of $\overline{B} \longrightarrow \pi^+\pi^-$	Measured Rate
0.3×10^{-5}	$(0.21 \pm 0.06) \times 10^{-5}$	0.3×10^{-5}	$(0.22 \pm 0.06) \times 10^{-5}$
1.1×10^{-5}	$(0.88 \pm 0.11) \times 10^{-6}$	1.1×10^{-5}	$(0.94 \pm 0.11) \times 10^{-5}$
1.3×10^{-5}	$(1.06 \pm 0.11) \times 10^{-5}$	1.3×10^{-6}	$(1.13 \pm 0.12) \times 10^{-5}$
1.5×10^{-5}	$(1.23 \pm 0.13) \times 10^{-5}$	1.5×10^{-5}	$(1.32 \pm 0.13) \times 10^{-5}$

Table 4.7: Table of measured branching fractions for a series of fits with input value of $\sin 2\alpha = 1$.

4.9.1 Fit results and interpretation

The measured fraction of $B \longrightarrow \pi^+\pi^-$ and $\overline{B} \longrightarrow \pi^+\pi^-$ events within the sample are given by eqn. 4.17 and 4.18 respectively:

$$b_{r2} = \frac{(1-\epsilon_2)b_{m2} - \epsilon\overline{b}_{m2}}{1-2\epsilon_2}, \tag{4.17}$$

$$\overline{b}_{r2} = \frac{(1-\epsilon_2)\overline{b}_{m2} - \epsilon_2 b_{m2}}{1-2\epsilon_2}, \tag{4.18}$$

where b_{m2} and $\overline{b}_{m2}$ are the corrected B and $\overline{B}$ fractions as measured by the fit and ϵ_2 is the mis-tag probability which is measured to be 0.16. From this and the reconstruction efficiency the measured rates can be obtained. Evidence of CP violation can be observed from the values of R^{+-} and K^{+-} obtained from the fit. $R^{+-} \neq 0$ implies direct CP violation and $K^{+-} \neq 0$ implies CP violation due to mixing (see chapter 1). K^{+-} is given by (see eqns. 1.14, 1.19 and 1.49)

$$\begin{aligned} K^{+-} \;=\; & \frac{4}{|A^{+-}|^2 + |\overline{A^{+-}}|^2}[\sin 2\alpha(|A_{i2}|^2 - |A_{i2}|(|\overline{A_{i0}}|\cos\overline{\theta} \\ & + |A_{i0}|\cos\theta) + |A_{i0}||\overline{A_{i0}}|\sin(\theta-\overline{\theta})) \\ & + \cos 2\alpha(|A_{i2}|(|\overline{A_{i0}}|\sin\overline{\theta} - |A_{i0}|\sin\theta) \\ & + |A_{i0}||\overline{A_{i0}}|\sin(\theta-\overline{\theta}))]. \end{aligned} \tag{4.19}$$

If $R^{+-} = 0$ and it is assumed that there are no penguin diagrams, then $K^{+-} = \sin 2\alpha$. For $R^{+-} = 0$ and $K^{+-} = 1$, the measured value of K^{+-} from the fit is 0.949 ± 0.082. The statistical errors arising from the fit for a selection of branching fractions are given

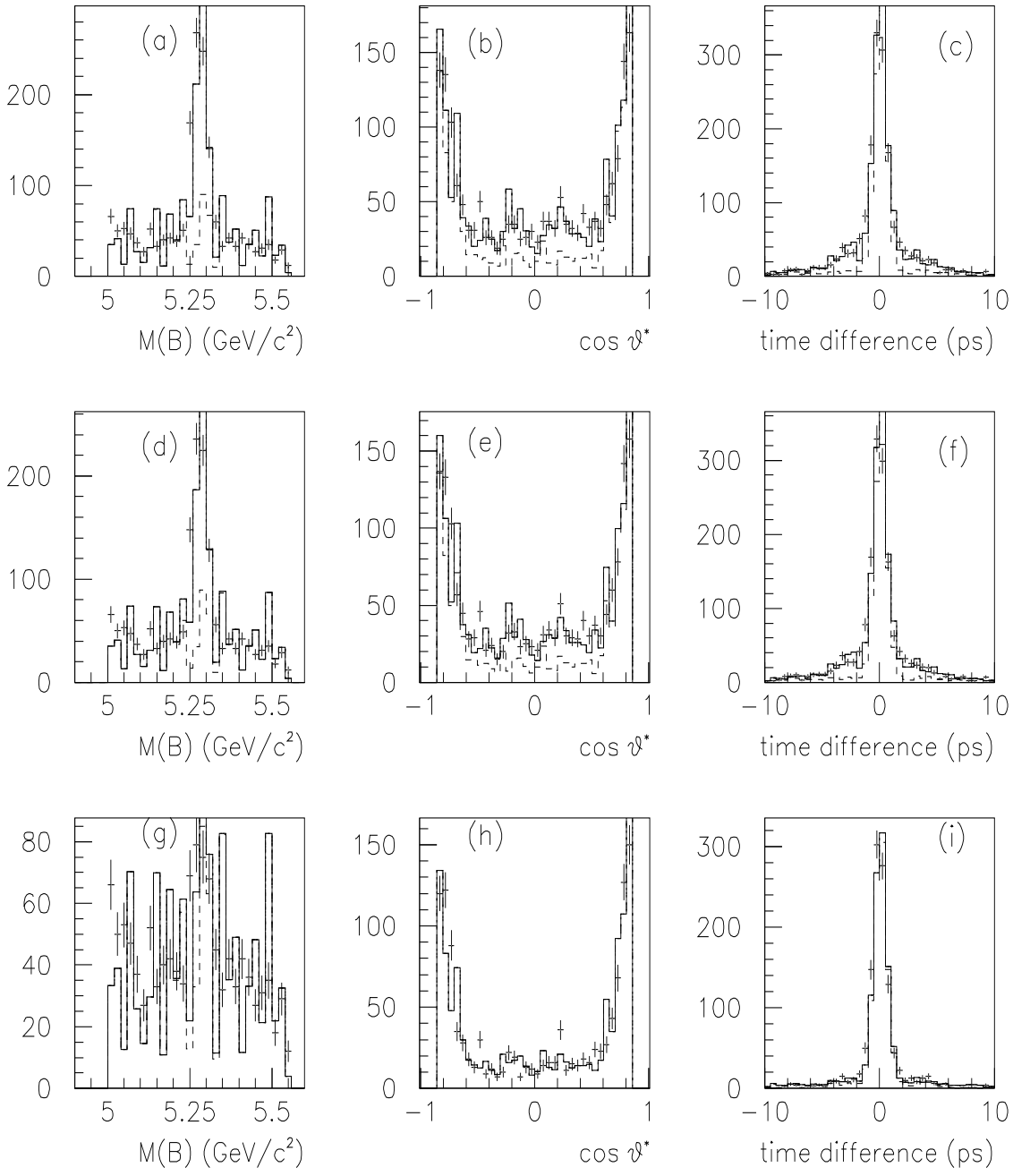

Figure 4.25: Projections showing results from a selection of fits. The crosses are the data, the overall fit is the solid line and the dashed line is the extracted continuum component. Plots are shown for a $B \longrightarrow \pi^+\pi^-$ rate of (a-c) 1.5×10^{-5}, (d-f) 1.3×10^{-5} and (g-i) 0.3×10^{-5}.

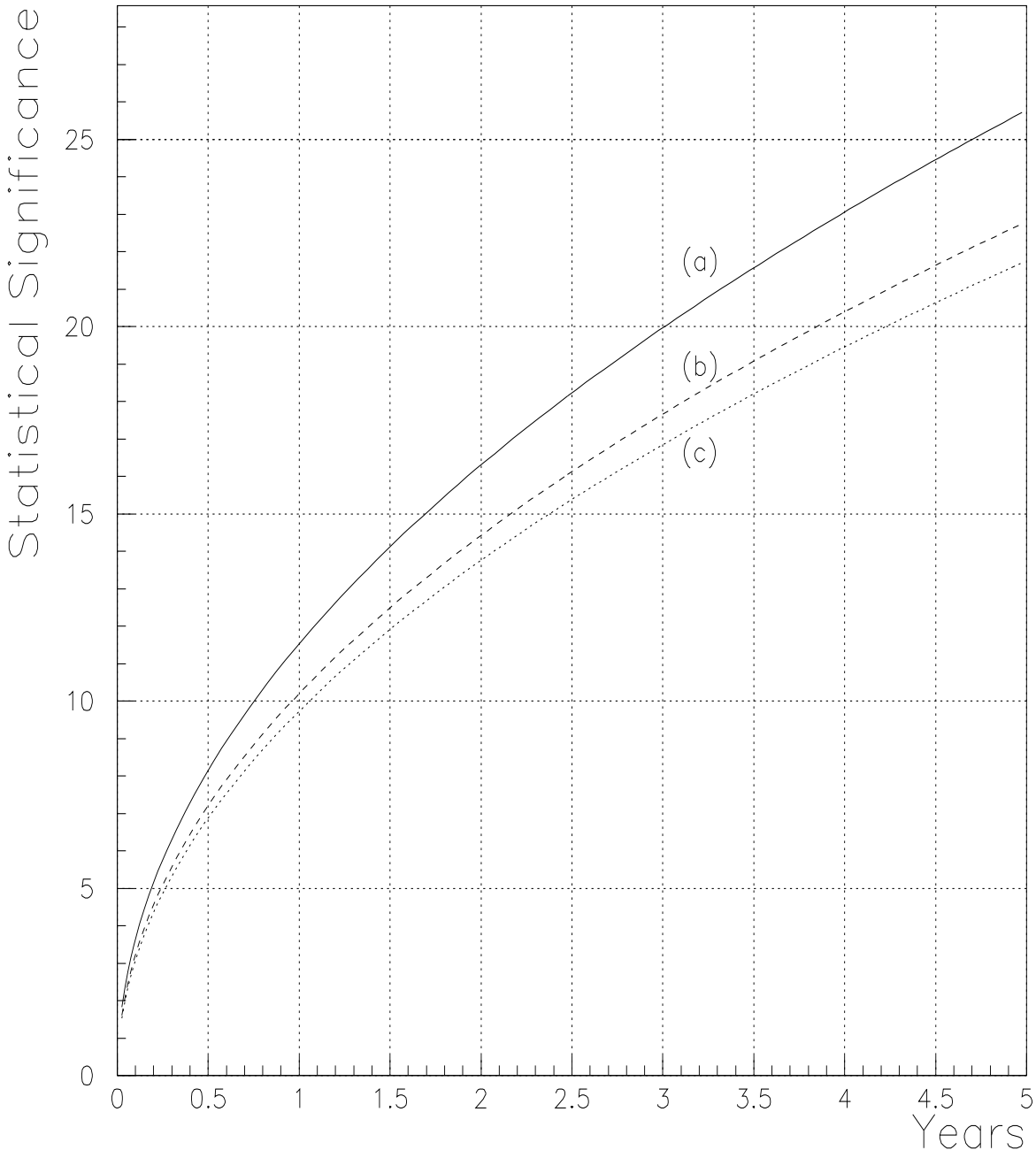

Figure 4.26: Future projections of the statistical significance of the fit measurement of the branching fraction for branching fractions of (a) 1.5×10^{-5}, (b) 1.3×10^{-5} and (c) 1.1×10^{-5}.

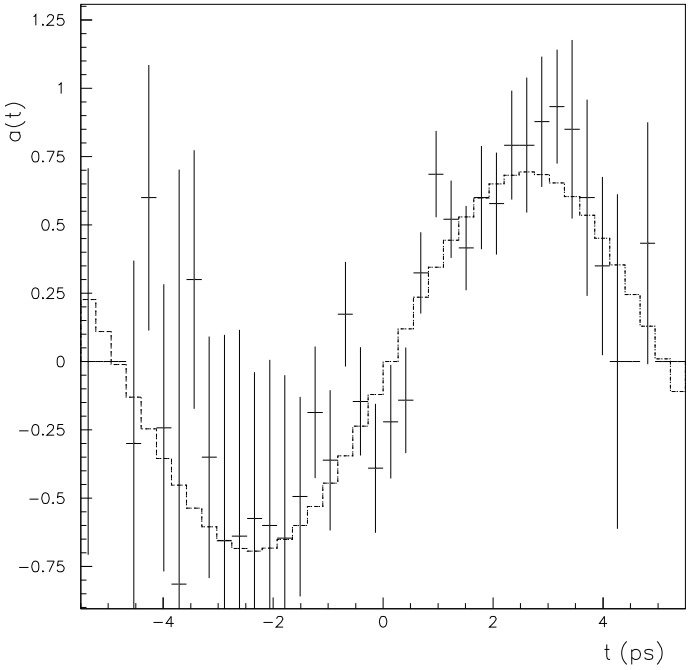

Figure 4.27: The observed asymmetry for $\sigma_t = 0.87ps$ (Δz resolution of $146\mu m$).

in Table 4.7. Figure 4.25 shows projections for these fits. For these fits it has been assumed that the B and $\overline{B}$ rates are identical. Taking the expectation value of the errors to be the mean of the B and $\overline{B}$ errors in a given fit, then the time evolution of errors are shown in figure 4.26. Figure 4.27 shows the fitted CP asymmetry for a time difference resolution (σ_t) of $0.87ps$ (Δz resolution of $146\mu m$). The plot shows larger statistical errors for negative than for positive time differences. This could possibly be attributed to mis-tagging of the B and $\overline{B}$ events. The plots of the measured errors on $\sin 2\alpha$ vs (a) the cross section for $B \longrightarrow \pi^+\pi^-$ and $\overline{B} \longrightarrow \pi^+\pi^-$ and (b) the Δz vertex resolution are shown in figure 4.28. The effect of systematic errors is discussed in section 4.9.2.

4.9.2 Evaluation of systematic errors

Sources of systematic errors which have been considered here are the uncertainty in the mis-tag probability, the uncertainty in the signal reconstruction efficiency and the uncertainty in the signal and background line shapes. The mis-tag probability can be measured from the data in the same way as discussed in section 4.7.2. Figure 4.29 shows

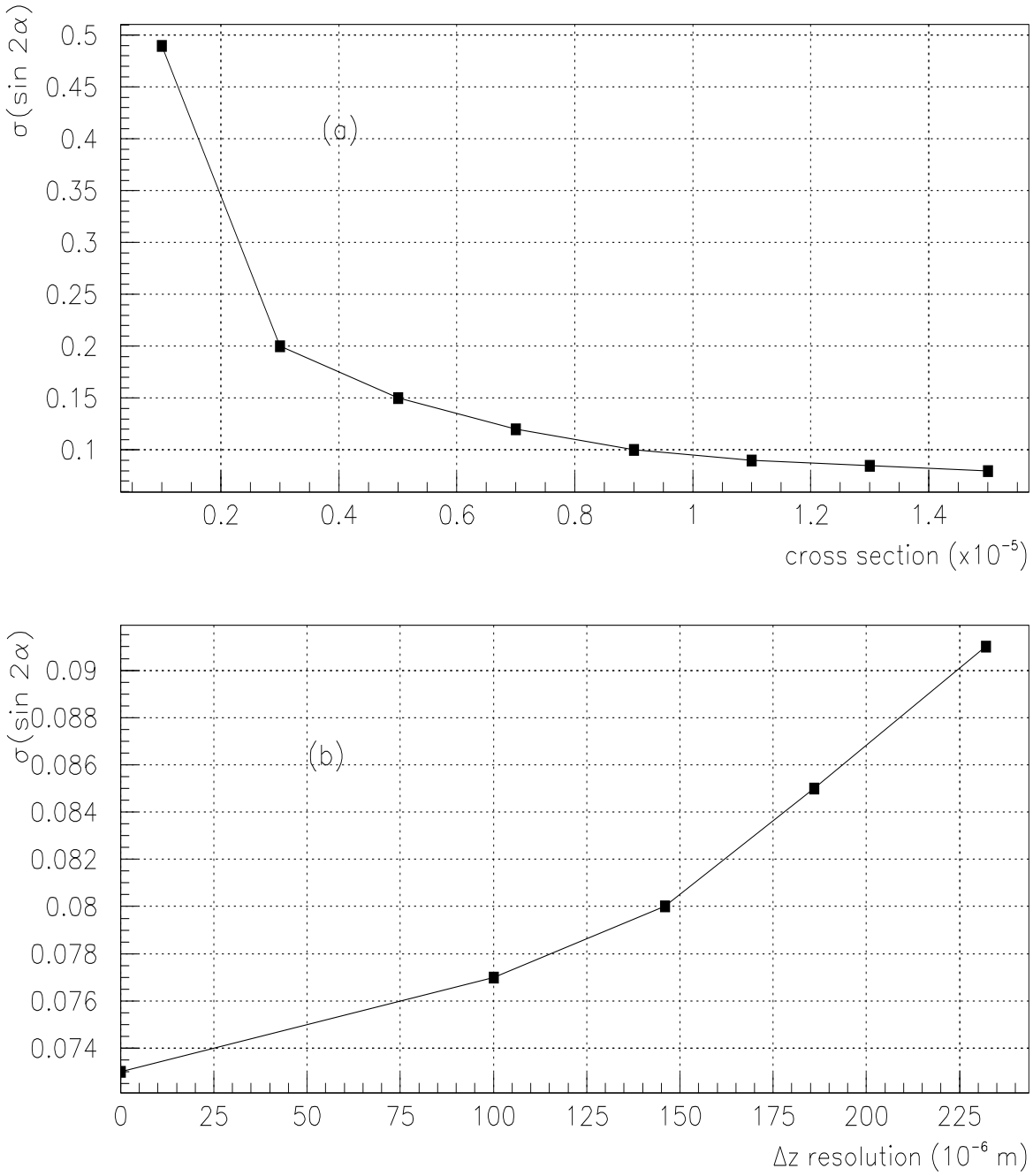

Figure 4.28: Plots of measured errors on $\sin 2\alpha$ vs (a) the cross section for $B \longrightarrow \pi^+\pi^-$ and $\overline{B} \longrightarrow \pi^+\pi^-$ assuming they are identical and (b) the Δz resolution.

the sensitivity of the measured cross section to the mis-tag probability from a fit in which there were no $\overline{b}$ events and the rate for $B \longrightarrow \pi^+\pi^-$ is 1.5×10^{-5}. The dependence

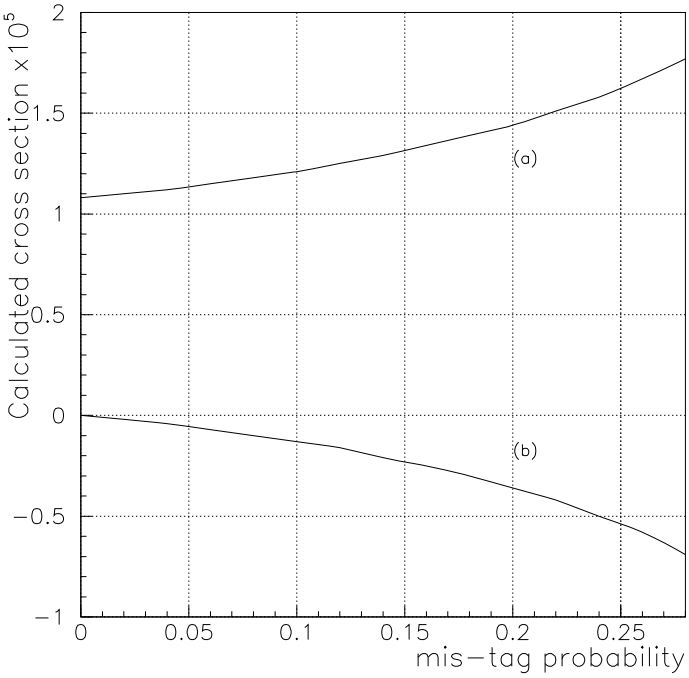

Figure 4.29: Sensitivity of the fit results to the measured mis-tag probability. The results shown are for a fit where the rate of $B \longrightarrow \pi^+\pi^-$ is 1.5×10^{-5} and the rate of $\overline{B} \longrightarrow \pi^+\pi^-$ is zero. The curves are for the calculated rates of (a) $B \longrightarrow \pi^+\pi^-$ and (b) $\overline{B} \longrightarrow \pi^+\pi^-$.

varies as a function of the mis-tag probability with no strong sensitivity in the region of 0.16. In determining the systematics due to signal line shapes, the M_B resolution used in the fit has been varied with respect to the optimal value. Assuming that the Monte Carlo can be trusted to within $\pm 5\%$, then the error on the observed number of events due to this effect is $\pm 1\%$ (see figure 4.30a). If it is assumed that the mean of the M_B can be determined to within $\pm 10 MeV/c^2$, then an error of $\pm 2\%$ is observed (see figure 4.30b). The systematic error due to the background line shape is negligible for same reasons as discussed in section 4.7.2. For this study it was arbitrarily decided that the reconstruction efficiency could be determined to within $\pm 5\%$ (ϵ_{reco}). The final error is given by

$$\epsilon_{total} = \epsilon_{fit} \oplus \epsilon_{reco} \oplus \epsilon_{lineshape}. \tag{4.20}$$

Adding the errors in quadrature results in the plot given in figure 4.31.

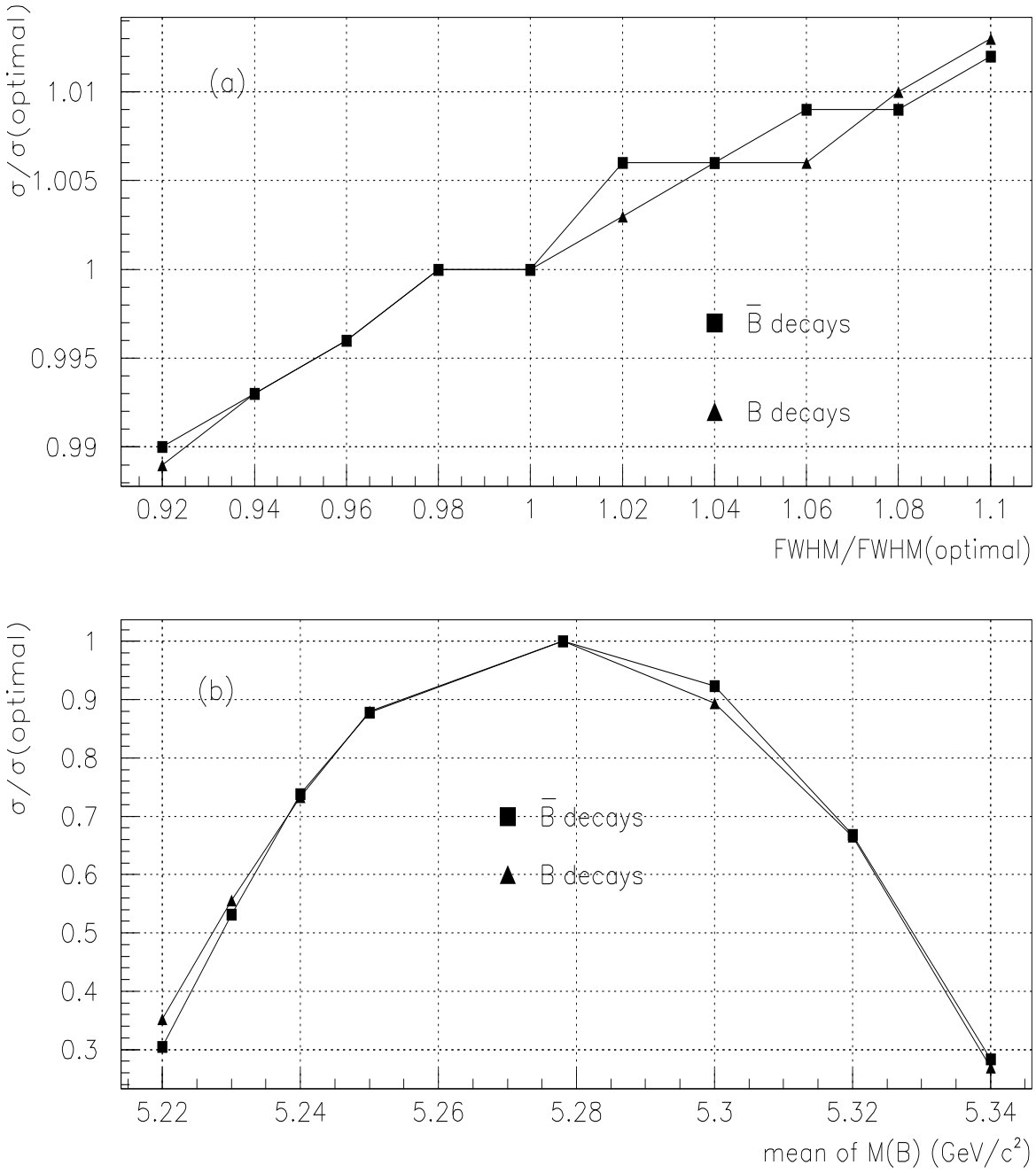

Figure 4.30: Variation of the measured cross section with respect to (a) the FWHM of the signal M_B distribution and (b) the mean of the signal M_B distribution. Curves are shown for the $\overline{B} \longrightarrow \pi^+\pi^-$ and $B \longrightarrow \pi^+\pi^-$ components. The rates for B and $\overline{B}$ decays has been taken to be 1.5×10^{-5} for these fits.

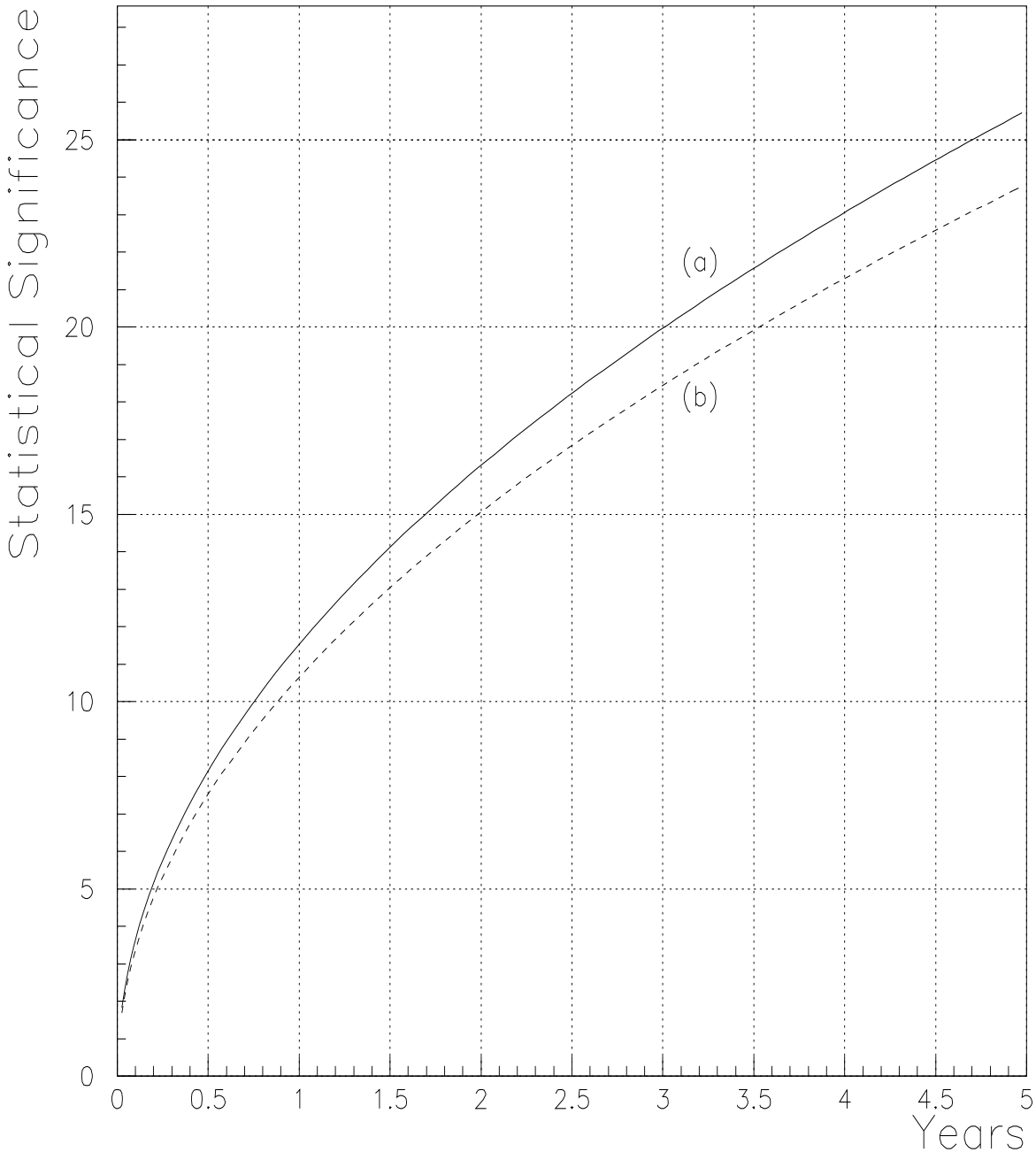

Figure 4.31: Time evolution of errors when the rate of $B \longrightarrow \pi^+\pi^-$ is 1.5×10^{-5}. Curves are shown for (a) the statistical error arising from the fit and (b) the statistical and the systematic errors added in quadrature.

4.10 Sensitivity to penguins

As discussed in section 4.9.1, if the CP asymmetry parameter $R^{+-} = 0$ and assuming there are no penguin diagrams, then eqn. 4.19 is quite simple, i.e. $K^{+-} = \sin 2\alpha$. On the other hand if $R^{+-} \neq 0$, i.e if there are penguin diagrams, then one needs to measure the amplitudes A_{i2}, $\overline{A}_{i2}$, A_{i0}, $\overline{A}_{i0}$, A^{+-}, $\overline{A}^{+-}$ and the angles θ and $\overline{\theta}$ to extract $\sin 2\alpha$ (see chapter 1). However it is worth noting that whilst measurement of $R^{+-} \neq 0$ will signify an observation of CP violation and hence penguin diagrams, $R^{+-} = 0$ will not necessarily mean penguin diagrams are negligible. The reason is that for small values of $|A_P|/|A_T|$ (≤ 0.1) [43],

$$R^{+-} \simeq -2\frac{|A_P|}{|A_T|}\sin(\phi_T - \phi_P)\sin(\delta_T - \delta_P) \tag{4.21}$$

and

$$K^{+-} \simeq \sin 2\alpha + 2\frac{|A_P|}{|A_T|}\sin(2\alpha + \phi_T - \phi_P)\cos(\delta_T - \delta_P), \tag{4.22}$$

where A_T, A_P, ϕ_T, ϕ_P, δ_T and δ_P are as defined in eqn. 1.10. Since we have no knowledge of $\sin(\phi_T - \phi_P)\sin(\delta_T - \delta_P)$ we cannot conclude that the penguin diagrams are negligible. The useful thing to be done in this situation is to proceed to carry on the full isospin analysis to extract $\sin 2\alpha$.

To evaluate the sensitivity on $\sin 2\alpha$ for a given $R^{+-} \neq 0$ and $K^{+-} = 1$ with branching fractions of B and $\overline{B}$ decays to $\pi^0\pi^0$, $\pi^+\pi^0$ and $\pi^+\pi^-$ as given in the first column of Table 4.8, measured errors on the branching fractions and K^{+-} from the fit with the triangular relations given in figure 1.6 have been used to obtain the missing variables in eqn. 4.19 and hence solve for $\sin 2\alpha$. However there is a four-fold discrete ambiguity since only $\cos\theta$ is measured (see chapter 1, eqns. 1.47 and 1.48). Table 4.9 shows the measured values of $\sin 2\alpha$ for the four pairs of θ and $\overline{\theta}$ given the input values of the first column of Table 4.8.

In order to investigate the effect on the results in Table 4.9 as the two triangles in figure 4.32(a) is increased, the $\overline{B} \longrightarrow \pi^0\pi^0$ branching fraction is varied, it has been changed to 5×10^{-6} keeping all others the same, the effect on the isospin triangles is shown in figure 4.32(b). The purpose is to increase the effect of the penguin contamination. The effect on the results are shown in Tables 4.10. It can be seen from figure 4.32 that the

	Assumed rate	Measured rates
$B^0 \longrightarrow \pi^0\pi^0$	0.2×10^{-5}	$(0.24 \pm 0.10) \times 10^{-5}$
$\overline{B}^0 \longrightarrow \pi^0\pi^0$	0.3×10^{-5}	$(0.25 \pm 0.11) \times 10^{-5}$
$B^0 \longrightarrow \pi^+\pi^-$	1.1×10^{-5}	$(0.85 \pm 0.10) \times 10^{-5}$
$\overline{B}^0 \longrightarrow \pi^+\pi^-$	1.0×10^{-5}	$(0.80 \pm 0.10) \times 10^{-5}$
$B^+ \longrightarrow \pi^+\pi^0$	1.0×10^{-5}	$(1.21 \pm 0.13) \times 10^{-5}$
K^{+-}	1.0	0.99 ± 0.11

Table 4.8: Table of measured branching fractions from the fits. It is assumed that $R^{+-} \neq 0$ i.e. the rates of B and $\overline{B}$ are different for decays to $\pi^+\pi^-$ and $\pi^0\pi^0$.

θ (radians)	$\overline{\theta}$ (radians)	$\sin 2\alpha$
2.35	2.11	0.98 ± 0.10
2.35	-2.11	0.85 ± 0.13
-2.35	2.11	0.80 ± 0.14
-2.35	-2.11	0.99 ± 0.10

Table 4.9: A table showing the four measured values of $\sin 2\alpha$ from the data in Table 4.8.

θ (radians)	$\overline{\theta}$ (radians)	$\sin 2\alpha$
2.35	1.84	0.95 ± 0.16
2.35	-1.84	0.78 ± 0.19
-2.35	1.84	0.72 ± 0.20
-2.35	-1.84	0.97 ± 0.14

Table 4.10: Results of the four values of $\sin 2\alpha$. The size of the penguin diagrams has been increased by increasing the $\overline{B} \longrightarrow \pi^0\pi^0$ branching fraction to 5×10^{-6}. All other rates in table 4.8 have been kept the same.

Figure 4.32: Isospin triangles showing the sides of the triangles from (a) the assumed rates in Table 4.8 and (b) the assumed rates in Table 4.8 but with $\overline{B} \longrightarrow \pi^0\pi^0$ rate of 5×10^{-6}. The labels in the diagrams correspond to the definitions in figure 1.6 with $a \equiv A^{+-}/\sqrt{2}$, $b \equiv A^{00}$ and $c \equiv A^{+0}$.

angle $\theta - \overline{\theta}$ in figure 4.32(b) is slightly larger than that in figure 4.32(a). Now, in the situation where $R^{+-} = 0$ and the B and $\overline{B}$ rates are the same so that the two triangles sit on top of each other, then the results of measurements are given in Table 4.11. Figure 4.33

θ (radians)	$\overline{\theta}$ (radians)	$\sin 2\alpha$
2.35	2.35	0.99 ± 0.10
2.35	-2.35	0.92 ± 0.10
-2.35	2.35	0.88 ± 0.11
-2.35	-2.35	0.99 ± 0.10

Table 4.11: Results showing the measured values of $\sin 2\alpha$ given $R^{+-} = 0$ and equal rates of B and $\overline{B}$.

shows the 95% confidence level region in the (ρ η) plane of the unitarity triangle from the results of $\sin 2\alpha$ in Table 4.11 (the value of $\sin 2\alpha$ used is the truth set that satisfy all the four solutions in the table), choosing $\sin 2\beta$ to be 0.700 ± 0.059 (the quoted error is from the TDR studies [25]) and current measurements of Δm_d, ϵ_k and V_{ub}/V_{cb}. Each shaded region corresponds to the (ρ, η) values satisfying the equations relating to a measurement at the 95% confidence level (see equations of Appendix A) and obtained by scanning the (ρ, η) plane. The lines marking the boundaries of each region are the solutions in the (ρ, η) plane for the upper and lower limits of the related measurement. From Table 4.11 the combined solution will imply our measurement of $\sin 2\alpha$ lies between 0.77 and 1.09. At the 95% confidence level (1.96σ) this implies $0.66 < \sin 2\alpha < 1.18$. For $\sin 2\beta$, at the 95% confidence level we have $0.58 < \sin 2\beta < 0.81$. The procedure followed was to scan the (ρ, η) plane, finding (ρ, η) pairs such that equation A.6 (see appendix A.4) satisfies $0.66 < \sin 2\alpha < 1.18$ and equation A.7 (see Appendix A.4) satifies $0.58 < \sin 2\beta < 0.81$. These truth pairs of ($\rho$, η) are what is seen lying in the horizontally shaded region in figure 4.33. The other shaded regions in figure 4.33 have been obtained in a similar manner. For example, the region shaded with the diagonal lines (Δm_d constraint) was obtained using equation A.3 in Appendix A.2. At the 95% confidence level the measured value of Δm_d lies between 0.42 and 0.50 (i.e. $0.465 \pm 1.96\sigma$, where σ is 0.024). Equating these values to equation A.3 give a region bounded by two circles with centres at (1, 0), where solutions for the lower limit (i.e. 0.42) and the upper limit (i.e. 0.5) mark the

boundaries represented by the solid curves. The allowed region for the apex of the triangle is the intersection of the shaded regions. It can be seen from the plots that the measurements of $\sin 2\alpha$ and $\sin 2\beta$ have imposed a much tighter constraint on the currently known allowed region for the apex of the triangle shown in figure 2.2.

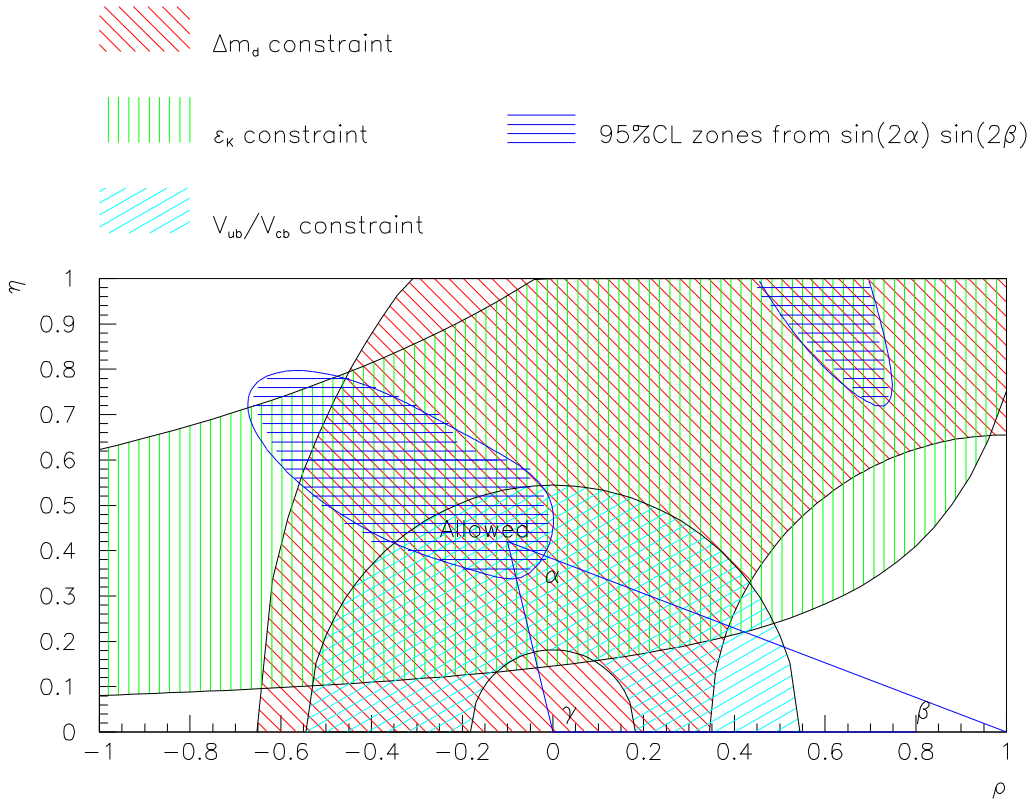

Figure 4.33: Plots showing the 95% confidence level region in the ρ, η plane of the unitarity triangle using results of $\sin 2\alpha$ in Table 4.11, $\sin 2\beta$ equals 0.700 ± 0.059 (from the TDR) and current measurements of Δm_d, ϵ_k and V_{ub}/V_{cb}. The intersection of the shaded regions gives an indication of the allowed region for the apex of the triangle.

Chapter 5

Conclusions

5.1 Introduction

In this chapter a brief summary is presented of the results showing the capabilities of the BABAR detector to make measurements of CP violation in the B system.

5.2 Test beam results

In chapter 3 a description has been made of the response of a prototype CsI electromagnetic calorimeter to a beam of electrons and pions in the energy range 0.1 to 0.4 GeV. The calorimeter was a 5×5 array of CsI crystals, which is a small scale version of the final detector of 6580 crystals. The size of each crystal was 5×5 cm at the front face, 6×6 cm for the back and 36 cm long. The electron energy resolution showed good agreement with the goal stated in the BABAR Technical Design Report; in particular the $1/\sqrt[4]{E}$ dependence expected was achieved. The measured resolution was $1.5\%/\sqrt[4]{E}$ compared with $1\%/\sqrt[4]{E}$ used in the TDR. However electronic noise in the prototype test which will be removed in the final system contributed at least part of this worse resolution. For pions, the distribution of deposited energy was not perfectly reproduced by the FLUKA and GHEISHA Monte Carlo code, possibly as a result of a poor approximation of the cross sections for nuclear interactions for low energy hadrons in both programs. However in this energy region studied it is clear that FLUKA provides a more adequate description of the data than GHEISHA.

5.3 B decays to $\pi\pi$

B decays to $\pi^+\pi^-$ allow the measurement of the CP asymmetry parameter $\sin 2\alpha$. In chapter 4 a new technique using a maximum likelihood method has been developed to extract this parameter in the absence of penguin diagrams. For a year's data the error on $\sin 2\alpha$ was calculated to be 0.082.

However the possible presence of penguin diagrams implies that the angle extracted from the fitted asymmetry parameter contains additional effects. Making a clean measurement of $\sin 2\alpha$ requires an analysis in which isospin symmetry is used to relate the three amplitudes of B and $\overline{B}$ decays to $\pi^+\pi^-$, $\pi^\pm\pi^0$ and $\pi^0\pi^0$. In this analysis the penguin contamination is calculated using isospin triangles and equations relating the measured amplitudes to $\sin 2\alpha$. The fraction of the measured asymmetry due to penguin contamination can be determined; as this fraction increases the error on $\sin 2\alpha$ gets slightly worse. The allowed region of the (ρ, η) plane corresponding to this measurement has been determined. The intersection of this region with the region currently allowed by other measurements gives an indication of the size of the additional constraint imposed by one full year of BABAR data.

Appendix A

Relating measurements to the CKM parameters: A, ρ, η

Points in the ρ, η plane for the apex of unitarity triangle are obtained by evaluating the equations relating the given measurements and the CKM parameters: A, ρ, η as given below.

A.1 $|V_{bc}|$ and $|V_{bu}/V_{bc}|$ measurements

$|V_{bc}|$ and $|V_{bu}/V_{bc}|$ are related by the equations:

$$|V_{bc}|(A) = A\lambda^2, \tag{A.1}$$

$$\frac{|V_{bu}|}{|V_{bc}|}(\rho,\eta) = \lambda\sqrt{\rho^2+\eta^2}. \tag{A.2}$$

A.2 Δm_{B_d} measurement

Δm_{B_d} is related by

$$\begin{aligned}\Delta m_{B_d}(A,\rho,\eta) &= \frac{G^2}{6\pi^2}A^2\lambda^6[(1-\rho)^2+\eta^2] \\ &\quad \times m_W^2 m_B (f_B\sqrt{B_B})^2\eta_B S(m_t/m_W^2),\end{aligned} \tag{A.3}$$

where G, f_B, B_B and $S(m_t/m_W^2)$ are as defined in section 2.2.2. In the usual unitarity triangle representation, this can be seen as the constraint of a circle with centre $(\rho,\,\eta) = (1,\,0)$ [40].

A.3 $|\epsilon_K|$ measurement

$|\epsilon_K|$ is related by

$$\begin{aligned} |\epsilon_K|(A,\rho,\eta) &= \frac{G^2}{6\sqrt{2}\pi^2}\frac{m_W^2}{\Delta m_K} m_K f_K^2 B_K A^2\lambda^6\eta[-\eta_1 S(m_c/m_W) \\ &\quad +A^2\lambda^4(1-\rho)\eta_2 S(m_t/m_W) \\ &\quad +\eta_3 S_{ij}(m_c/m_W, m_t/m_W)], \end{aligned} \tag{A.4}$$

where f_K is the decay constant for the K meson, η_1, η_2 and η_3 are the QCD correction factors [41], B_K is the K meson mixing parameter, m_c, m_t, and m_W are the masses of the charm quark, top quark and W boson respectively, Δm_K is the K_L and K_S mass difference, the function S is as defined in section 2.2.2 and $S_{ij}(x_c, x_t)$ is defined as [42].

$$S_{ij}(x_c,x_t) = x_c\left[\ln\frac{x_t}{x_c} - \frac{3x_t}{4(1-x_t)} - \frac{3x_t^2\ln x_t}{4(1-x_t)^2}\right]. \tag{A.5}$$

Equation A.4 specifies a hyperbola in the (ρ, η) plane.

A.4 $\sin 2\alpha$ and $\sin 2\beta$ measurements

Applying simple trigonometrical relations on the unitarity triangle, measurements of $\sin 2\alpha$ and $\sin 2\beta$ are related to the CKM parameters: A, ρ and η as follows:

$$\sin 2\alpha(\rho,\eta) = \frac{2\eta(\eta^2+\rho^2-\rho)}{(\rho^2+\eta^2)((1-\rho)^2+\eta^2)} \tag{A.6}$$

$$\sin 2\beta(\rho,\eta) = \frac{2\eta(1-\rho)}{((1-\rho)^2+\eta^2)}. \tag{A.7}$$

Appendix B

Formulae used in the analysis of $B \longrightarrow \pi\pi$

B.1 The M_B component

The Gaussian function used to fit the B mass distribution of the signal component of the data is defined as

$$g_{sig}(M_B) = \exp\left[\frac{-1}{2}\left(\frac{M_B - M_B^{mean}}{\sigma}\right)^2\right]. \tag{B.1}$$

A fit function to a log normal distribution is given by

$$g_{sig}(M_B) = \frac{1}{X_0 - M_B}\exp\left[-\left(\frac{\ln(X_0 - M_B) - M_B^{mean}}{\sigma}\right)^2\right], \tag{B.2}$$

where M_B^{mean} is the mean value of M_B, σ is the error on the mean and X_0 is a free parameter for the tail.

The background component is fitted with the function given by

$$g_{back}(M_B) = M_B.\exp(p_1^2).\left(-1 - \left(\frac{M_B}{5.65}\right)^2\right).\sqrt{1 - \left(\frac{M_B}{5.65}\right)^2}, \tag{B.3}$$

where p_1 is a free parameter.

B.2 The $\cos\theta^*$ component

The $\cos\theta^*$ distribution for the continuum component of the data is fitted by

$$h_{back}(\cos\theta^*) = \exp\left[\frac{-1}{2}\left(\frac{|\cos\theta^*| - 1}{\sigma_1}\right)^2\right] + c \tag{B.4}$$

where σ_1 is the error on the Gaussian and c is the constant term.

B.3 The time difference (t) component

The convolution of the time dependent rate for B decays to $\pi^+\pi^-$ with the Gaussian errors on time difference t is given by (see references [44, 45, 46])

$$P(t') = \frac{A_n}{2}\int_{-\infty}^{\infty} e^{\frac{-(t-t')^2}{2\sigma_t^2}} e^{-\Gamma|t|}\left\{1 + R^{+-}\cos\Delta Mt - K^{+-}\sin\Delta Mt\right\} dt \quad (B.5)$$

$$= \frac{A_n\sqrt{\pi}}{8}\left[g(t')e^{\Gamma^2\sigma_t^2/2} + e^{-t'^2/2\sigma_t^2}(R^{+-}h(t') + K^{+-}j(t'))\right] \quad (B.6)$$

where:

$$g(t') = e^{\Gamma t'}erfc(t'_+) + e^{-\Gamma t'}erfc(t'_-) \quad (B.7)$$

$$h(t') = Re\{W(\frac{-\Delta M\sigma_t}{\sqrt{2}} + it'_+) - W(\frac{-\Delta M\sigma}{\sqrt{2}} + it'_-)\} \quad (B.8)$$

$$j(t') = Im\{W(\frac{-\Delta M\sigma_t}{\sqrt{2}} + it'_+) - W(\frac{-\Delta M\sigma_t}{\sqrt{2}} + it'_-)\} \quad (B.9)$$

and $t'_\pm$ is defined as

$$t'_\pm = \frac{\Gamma\sigma_t^2 \pm t'}{\sqrt{2}\sigma_t}. \quad (B.10)$$

The complex error function W(x) is defined as

$$W(x) \equiv e^{-x^2}erfc(-ix). \quad (B.11)$$

Erfc is a standard fortran function, $\Gamma = 1/\tau$ and $A_n\sqrt{\pi}/8$ is the normalisation.

In evaluating eqn. B.5, use has been made of the following integrals [46]:

$$\int_0^\infty e^{-(az^2+bz+c)}\sin Kz\ dz = -\frac{1}{2}\sqrt{\frac{\pi}{a}}e^{-c}Im[e^{\frac{(b+iK)^2}{4a}}erfc(\frac{(b+iK)}{2\sqrt{a}})] \quad (B.12)$$

$$\int_0^\infty e^{-(az^2+bz+c)}\cos Kz\ dz = \frac{1}{2}\sqrt{\frac{\pi}{a}}e^{-c}Re[e^{\frac{(b+iK)^2}{4a}}erfc(\frac{(b+iK)}{2\sqrt{a}})] \quad (B.13)$$

where a, b, c and K are real constants. Then applying eqn. B.11, B.12 and B.13 the convolution with a single Gaussian $G(t,t') = e^{\frac{(t-t')^2}{2\sigma_t^2}}$ gives:

$$\int_0^\infty G(t,t')e^{-\Gamma t}\sin\Delta Mt\ dt = -\frac{\sqrt{\pi}}{2}e^{-t'^2/2\sigma^2}Im[W(\frac{-\Delta M\sigma_t}{\sqrt{2}} + i\frac{\Gamma\sigma_t^2 - t'}{\sqrt{2}\sigma_t}] \quad (B.14)$$

$$\int_0^\infty G(t,t')e^{-\Gamma t}\cos\Delta Mt\ dt = \frac{\sqrt{\pi}}{2}e^{-t'^2/2\sigma_t^2}Re[W(\frac{-\Delta M\sigma_t}{\sqrt{2}} + i\frac{\Gamma\sigma_t^2 - t'}{\sqrt{2}\sigma_t}]. \quad (B.15)$$

The convolution for the $\overline{B}$ component can be evaluated in the same way to obtain

$$\overline{P}(t') = \frac{A_n\sqrt{\pi}}{8}\left[g(t')e^{\Gamma^2\sigma_t^2/2} - e^{-t'^2/2\sigma_t^2}(R^{+-}h(t') + K^{+-}j(t'))\right]. \quad \text{(B.16)}$$

The time difference (t) component for the background is parameterised by a double Gaussian given by

$$P_{back}(t) = N_1 e^{-\frac{1}{2}(t/\sigma_1)^2} e^{-\frac{1}{2}(t/\sigma_2)^2}, \quad \text{(B.17)}$$

where N_1 is the normalisation and σ_1, σ_2 are the Gaussian errors.

Bibliography

[1] Proceedings of the School for Young High Energy Physicists, Technical Report RAL-TR-96-018, ps. 109, 116.

[2] The OPAL Collaboration, "Search for the Standard Model Higgs Boson in e^+e^- Collisons at $\sqrt{s}$ = 161 - 172 GeV", CERN-PPE/97-115 (1997).

[3] The OPAL Collaboration, "A Study of B meson Oscillations Using Hadronic Z^0 Decays Containing Leptons", CERN-PPE/97-036, April 1997.

[4] LHC-B Letter of intent, CERN/LHCC 95-5 LHCC/I 8 25, August 1995.

[5] L. Wolfenstein, Phys. Rev. Lett. **51**, (1983) 1945.

[6] M. Gronau, "Testing the Standard Model of CP Violation in the B System", TECHNION-PH-94-64, November 1994.

[7] M. Gronau, Phys. Rev. Lett. **65**, (1989) 1451.

[8] D. London, "CP Violation in the B System", UdeM-LPN-TH-94-199, June 1994.

[9] N.G. Deshpande and Xiao-Gang He, Phys. Rev. Lett. **74**, (1995) 26.

[10] J. Alexender, "$B \longrightarrow K\pi$, $\pi\pi$, KK", presented at "Hawaii Conf. on B Physics and CP Violation", Honolulu, Hawaii, March 24-27, 1997.

[11] The BABAR Collaboration, "BABAR Technical Design Report", SLAC-R-95-457, March 1995, p. 531.

[12] LHC-B Letter of intent, CERN/LHCC 95-5 LHCC/I 8 25, August 1995, p. 112.

[13] G. Wormser, "Measuring CP violating asymmetries in B decays with the BABAR and BELLE detectors", Laboratoire de l'Accelerateur Lineaire d'Orsay IN2P3-CNRS et Universite Paris-XI, 91405 Orsay, France.

[14] BTEV Collaboration, "An expression of interest for a Heavy quark program at CO", May 18, 1997, pp. 114-119.

[15] J. H. Christenson, J. W. Cronin, V. L. Fitch, and R. Turlay, Phys. Rev. Lett. **13**, (1964) 138.

[16] L.K. Gibbons et al., "CP and CPT Symmetry Tests from the Two-pion Decays of the Neutral Kaon with the Fermilab-E731 Detector", FERMILAB-Pub-95/392-E Revised EFI-95-76 E731, March 1997, p. 84.

[17] CPLEAR Collaboration, Phys. Lett. **B363**, (1995) 237.

[18] G. Bauchalla and A. J. Buras, Phys. Rev. **D54**, (1996) 6782.

[19] G. Bauchalla, "CP Violation in Neutral Kaon Decays", SLAC-PUB-7520 HEP-PH/9705369, May 1997.

[20] Particle Data Group, Phys. Rev. **D50**, (1994) 1315.

[21] K. Berkelman, "The CESR-CLEO Program", CLNS 96/1398.

[22] V. Barger, C.S. Kim and R.J.N. Phillips, Phys. Lett. **B251**, (1990) 629.

[23] CLEO Collab., R. Fulton et al., Phys. Rev. Lett. **64**, (1990) 16.

[24] T. Inami and C. S. Lim, Prog. Theor. Phys., **65** (1981) **297**; *ibid.*, **65** (1981) 1772(E).

[25] The BABAR Collaboration, "BABAR Technical Design Report", SLAC-R-95-457, March 1995, pp. 81, 248.

[26] The BABAR Collaboration, "BABAR Technical Design Report", SLAC-R-95-457, March 1995, pp. 265, 325.

[27] The BABAR Collaboration, "Results from the BABAR Electromagnetic Calorimeter Beam Test", BABAR Note # 367 (1997).

[28] A. J. Noble, "A Study of Hadronic Interactions in CBGEANT", CB Note No. 258, July 1, 1994.

[29] M. Blann, Phys. Rev. Lett. **21**, (1968) 1357.

[30] J. J. Griffin, Phys. Rev. Lett. **17**, (1966) 478.

[31] GEANT 3.21: Detector Description and Simulation Tool, CERN program library, March 1994.

[32] CLEO Collaboration, Phys. Rev. **D53**, (1996) 1039.

[33] T. Sjostrand, JETSET 7.3, CERN-TH 6488/92, May 1992.

[34] T. Glanzman, W. Innes, S. Saxena and A. Snyder, "Using ASLUND at SLAC", BABAR Note # 117 (1993).

[35] P. F. Harrison et al., "Electromagnetic Calorimeter Resolutions: Parameterisation in ASLUND", BABAR Note # 249 (1995).

[36] S. Versaille and C. Yeche, "User Guide of CORNELIUS V00-01-00", BABAR Tagging Note # 5, September 1996.

[37] D.E Jaffe, F. Le Diberder, M. H. Schune and G. Wormser, "Treatment of weighted events in a likelihood analysis of B_S oscillations or CP-violation", BABAR Note # 132.

[38] A. G. Frodesen, "Probability & Statistics in Particle Physics", Global Books Resources Ltd., U.K. (1979)

[39] F. James, "MINUIT - Function Minimization and Error Analysis", CERN Program Library D506.

[40] S. Plaszczynski and M. H. Schune, "An overall fit of the CKM parameters: present and future for BABAR", BABAR Note # 340, December 12, 1996.

[41] A. J. Buras, "Flavour Changing Neutral Current Processes", Proceedings of the 28^{th} International Conference on High Energy Physics, (1996) 243.

[42] G. Buchalla, A. J. Buras and M. E. Lautebbacher, Rev. Mod. Phys. **Vol.68**, (1996) 1181.

[43] R. Aleksan, A. Gaidot and G. Vasseur, "Probing the Penguin Contribution in $B \longrightarrow \pi\pi$ at an Asymetric B meson Factory", DAPNIA/SPP 92-19, September 1992.

[44] F. LeDiberder, "Precision on CP violation Measurements and Requirements on the Vertex Resolution", BABAR Note # 34.

[45] W. Toki, "Parametrization of Decay Length Distributions with errors", BABAR Note # 35.

[46] P. S. Marroccesi, "An unbinned likelihood analysis of CP violation", BABAR Note # 257.